UC Berkeley
UC Berkeley Electronic Theses and Dissertations

Title
Quantitative characterization of meiotic chromosome organization

Permalink
https://escholarship.org/uc/item/5mr0c0kp

Author
Cheveralls, Keith Charles

Publication Date
2016

Peer reviewed|Thesis/dissertation

eScholarship.org Powered by the California Digital Library
University of California

Quantitative characterization of meiotic chromosome organization

By

Keith Charles Cheveralls

A Dissertation submitted in partial satisfaction of the

requirements for the degree of

Doctor of Philosophy

in

Biophysics

in the

Graduate Division

of the

University of California, Berkeley

Committee in charge:

Professor Abby F. Dernburg, Chair
Professor David Drubin
Professor Barbara Meyer
Professor Eva Nogales

Spring 2016

Abstract

Quantitative characterization of meiotic chromosome organization

by

Keith Charles Cheveralls

Doctor of Philosophy in Biophysics

University of California, Berkeley

Professor Abby F. Dernburg, Chair

Sexual reproduction relies on a specialized program of cell division called meiosis to generate haploid gametes from diploid germ cells. In order for chromosome segregation to occur accurately, homologous chromosomes must pair, synapse, and undergo crossover recombination. These physical and biochemical interactions occur in coordination with large-scale reorganization of meiotic chromosomes. To understand the relationship between chromosome organization and the regulation of recombination, we developed an automated image analysis pipeline that combines the throughput of population-based biochemical assays with the temporal and contextual information provided by cytological methods. This new technique enables us to monitor temporal changes in the distribution of meiotic double strand breaks (DSBs) on a chromosome-wide basis and to correlate that distribution with features of meiotic chromosome organization. We applied this technique to meiotic chromosomes in the nematode *Caenorhabditis elegans* and observed that the distribution of DSBs is dynamic during prophase and shifts from a distribution that mirrors the distribution of crossovers to one that is more uniform. This shift correlates with isotropic, recombination-independent elongation of chromosomes along the axis and is insensitive to defects in recombination, variation in the number of DSBs, and variation in chromosome axis length. This work reveals a novel dynamic aspect of meiotic DSB formation and quantifies, for the first time, statistical features of meiotic chromosome organization in *C. elegans*.

Table of Contents

Chapter 1 Introduction 1
Chapter 2 Automated image analysis of meiotic chromosomes 10
Chapter 3 Characterization of meiotic chromosome organization and the distribution of DSBs and crossovers 25
Chapter 4 Observing homolog interactions using FISH 46
References 58

List of Figures

Figure 2.1 Overview of analysis pipeline for automated segmentation and tracing of pachytene chromosomes 12
Figure 2.2 Overview of nucleus segmentation 14
Figure 2.3 Chromosome segmentation using iterative region merging 16
Figure 2.4 Chromosome tracing using skeletonization and active contours 19
Figure 2.5 Methodology for measuring the position of nuclei within the gonad 21
Figure 2.6 SIM imaging of meiotic chromosome axes 23

Figure 3.1 Chromosome axes elongate during pachytene 28
Figure 3.2 Chromosome III axis length and compaction during pachytene 30
Figure 3.3 Chromosome V axis length variation 32
Figure 3.4 Axis lengths are correlated within single nuclei 32
Figure 3.5 RAD-51 foci are arm enriched in early pachytene but uniformly distributed in late pachytene. 35
Figure 3.6 Axis length does not predict RAD-51 distribution, and RAD-51 foci do not interfere 37
Figure 3.7 Axis curvature near DSBs and crossovers 39

Figure 4.1 Distribution of SNPs and homolog probe design 48
Figure 4.2 Localization of a 250kb region in the Chromosome III pairing center in the transition zone 50
Figure 4.3 Localization of a 250kb region in the Chromosome III pairing center during pachytene and at diakinesis 52
Figure 4.4 Homolog probe hybridization is specific and robust 54
Figure 4.5 Chromosome III homolog FISH suggests pairing center regions colocalize specifically in the transition zone 55
Figure 4.6 Quantification of homolog FISH focus overlap 57

Acknowledgements

There is only one way to begin these acknowledgements, and that is by thanking my parents: while many people have made this thesis possible, my parents have made it all possible. I owe whatever achievement an advanced degree represents to the unconditional love and support that they have shown me for the past three decades, even as my own path in life has diverged in just about every way—geographically, personally, and professionally—from any with which they are familiar.

On the smaller scale of my graduate career, I am similarly grateful to my advisor, Abby Dernburg, for trusting me to pursue a project whose methods were both new to her and outside of the lab's expertise. The loneliness of this pursuit was considerably lightened by the truly supportive and caring environment that she has fostered in the lab—this is a rare advantage in science, and in life, and one to which I hope my tenure in the lab has done justice. Scientifically, Abby's uncanny ability to discern principles where others see only discordant results has been inspirational to observe and has deepened my appreciation for the beauty of biology.

It has been a pleasure to work alongside the many people with whom I have overlapped in the Dernburg lab and who have, without exception, made it a friendly and fun place to do science, including Baris Avsaroglu, Josh Bayes, Gilbert Garcia, Nina Glazier, Nicola Harper, Yumi Kim, Simone Kohler, Chitra Kotwaliwale, Regina Rillo, Ericca Stamper, Dave Wynne, Zhouliang Yu, and Liangyu Zhang. I owe a special thanks to Hoang Pham, our lab manager, who has helped the lab navigate countless administrative snafus, anticipated problems before they became problems, and also, incidentally, built the computer that much of this work was performed on. I am also indebted to Michelle Scott, the manager of LBL's Advanced Microscopy Facility, for providing technical assistance on the many occasions when difficulties with structured illumination microscopy materialized.

I would like to thank my thesis committee—Barbara Meyer, Eva Nogales, and David Drubin—for their advice and comments on the intermediate stages of my research, with special thanks to Barbara for very detailed comments on a draft of this thesis. The image analysis portion of the work summarized here owes much to Paul Wiggins, from whom I learned both how to run a gel and how to (attempt to) transform images into results. At the other end of my graduate career, Hernan Garcia offered thoughtful feedback on my work as well as unbiased career advice. Kate Chase, our Biophysics Program coordinator, plays a much more central role in the program than that word implies, and the quiet competence with which she guards the interests of the program and its students has been a constant source of assurance and support throughout my time here.

In the very earliest days of my PhD, the kindness of two friends from back east—Matt Marcello and April Lambert—made coming to California, and staying here, much easier than it otherwise would have been. Since then, my time at Berkeley has been enlivened and enriched by the constellation of friends I have found here. In particular, I am grateful to Aaron Smyth for piloting his share of our combined roommateship-friendship with an energy I can only imagine having, and to Joey Greenspun for tirelessly reminding me that a glass half empty is no reason not to keep running (but

that sometimes tender tendons are). I have not met anyone in science as effortlessly funny as Nora Kostow, and she has brought no small measure of light to many an otherwise dull moment. I hope it is safe to say that we have, finally, graduated from colleagues to friends.

Although chromosomes lie well beyond the length scale of his own interests, my boyfriend, Eric Bolin, has met my frustrations and complaints—both scientific and extra-scientific—with patience and good humor. He has done more than anyone else to smooth the many bumps in graduate school's long road.

Finally, but very much not least, thanks to Ofer Rog, who has toed the blurry line between mentorship and friendship with generosity, thoughtful equanimity, and an inimitable blend of kindness and irony. It is impossible for me to imagine the last six years here—in California, at Berkeley, and in Bay 4 of the Dernburg lab—without him.

Chapter 1 Introduction

Sexual reproduction

All living things must reproduce. Some organisms, including all bacteria, many fungi, and some plants, reproduce by generating a copy of themselves—often by literally splitting themselves in half. This is asexual reproduction, and it is the simplest and most ancient reproductive scheme. For reasons that remain poorly understood, most multicellular organisms do not reproduce asexually. Instead, they reproduce by generating specialized cells that fuse together to form a single daughter organism. Usually, these cells are contributed by two different parents, so that their offspring inherits genes from each and is an exact copy of neither. This is sexual reproduction.

The obvious complexity and inefficiency of sexual reproduction poses challenges to the organism seeking to execute it and to the biologist seeking to understand it. These challenges are both mechanistic and evolutionary. Mechanistically, the parental organisms must generate sex cells—sperm and eggs—having half of their own chromosomal copy number, so that upon fertilization, the parental ploidy is restored in the daughter organism. This requires a special program of cell division called meiosis in which the copies, or homologs, of each chromosome are segregated away from one another, followed by sister chromatids. Remarkably, prior to segregation, recombinational interactions shuffle genes between the homologs of each chromosome to generate novel allelic combinations. The fusion of sperm and egg during fertilization thus begets an organism carrying a complex admixture of parental alleles and endowed with a genetic—and usually phenotypic—identity unique from both its parents and siblings.

Evolutionarily, sexually reproducing species must overcome the challenge of competing with asexually reproducing species that can proliferate twice as fast and therefore possess a staggering numerical advantage. That this competition has instead favored sexual reproducing organisms is evident in the persistent dominance of higher eukaryotes for the past several hundred million years. Our understanding of the advantages of sexual reproduction that underlie this dominance remains incomplete. It is likely that the advantages are multiple; two of the most plausible are that the genetic diversity generated by sexual reproduction yields more adaptable populations, while genetic exchange between homologs allows for the elimination of deleterious alleles.

The focus of the work presented here is on the first of these two challenges—that is, on understanding the mechanics of how homologous chromosomes interact, recombine, and, ultimately, segregate away from each other during meiosis.

Meiosis: an overview

Two events distinguish meiosis from the canonical mitotic program of cell division. The first is the occurrence of homologous recombination between homologs that culminates in the formation of sites, called crossovers, at which homologs have reciprocally exchanged alleles. The second is the use of two sequential rounds of cell division to segregate first homologs and then sister chromatids away from each other, yielding gametes whose ploidy is half that of the parental organism. These two events—crossover formation and homolog segregation—do not occur independently but instead

are intimately mechanistically linked, for the crossovers formed between homologs provide the physical linkages required for homologs to segregate away from each other at the first meiotic division. To complete meiosis successfully, the cell must therefore ensure that crossovers form between each pair of homologs.

This imperative to form crossovers conflicts with the cell's basic interest in maintaining the integrity of its genome. For in order to initiate homologous recombination, the cell must deliberately generate double strand breaks—a dangerous kind of DNA damage against which, at other times, it deploys elaborate repair machinery to combat. It should come as no surprise, then, that meiotic recombination is highly regulated and tightly coupled to the intricate physical interactions that occur between homologous chromosomes during meiotic prophase.

These interactions begin with a process called homolog pairing during which each homolog identifies and stably associates with its homologous partner. Next, a proteinaceous structure called the synaptonemal complex assembles between each pair of homologs and holds them together along their lengths. This process is called synapsis. At the same time, crossover formation begins as programmed double strand breaks (DSBs) are generated throughout the genome and subsequently repaired using homologous recombination; a subset of these repair events yield crossovers. Following crossover formation, the SC is removed, and cohesion between recombinant homologs partially lost, allowing homologs to segregate away from each other at the first meiotic division. Sister chromatids are then segregated in a second, mitosis-like division that immediately follows the first, finally yielding four haploid gametes.

Defects in any of the interactions between homologs usually result, if not in unrepaired DSBs and fragmented chromosomes, then in the failure of one or more pairs of homologs to form crossovers. When this happens, homologs fail to segregate away from each other at the first meiotic division, yielding gametes having either no copies, or more than one copy, of particular chromosomes. This imbalance is called aneuploidy, and, when it is not fatal to the developing embryo, usually results in genetic disorders. In humans, almost all aneuploidies yield miscarriages. Those that do not include trisomy of chromosome 21, which causes Down syndrome, and either disomy of the X chromosome in males or monosomy in females, which cause Klinefelter and Turner syndromes, respectively (Nagaoka et al., 2012).

Meiotic recombination

Meiotic recombination is the hallmark event of meiotic prophase. The crossovers that are its final outcome both ensure that homolog segregation occurs accurately and generate the genetic diversity that underlies the evolutionary success of sexually reproducing organisms. Crossover formation involves both the somatic DNA damage repair machinery, meiosis-specific recombination factors, and the unique axis-based organization of meiotic chromosomes.

The first step in crossover formation is the programmed formation of DSBs throughout the genome in early meiotic prophase. In all studied organisms, these breaks are catalyzed by the enzyme SPO-11, a highly conserved and meiosis-specific endonuclease homologous to the catalytic subunit of a type II topoisomerase (Keeney, 2001). Following break formation, SPO-11 is removed from the DSB and the 5' strand is resected. The resulting 3' single-stranded overhang then searches for and 'invades' the

intact duplex of the homologous chromosome, eventually forming a Holliday junction (Hunter and Kleckner, 2001). The invasion process is catalyzed by the recA homologs RAD-51 and, in some organisms, DMC-1 (reviewed in Keeney et al., 2014). These molecules form a nucleoprotein filament along the break-adjacent single-stranded DNA and mediate the search for homology and the subsequent formation of a Holliday junction intermediate. Once both ends of the DSB have invaded the same homologous strand, the resulting double Holliday junction can be resolved to form a crossover (reviewed in Kohl and Sekelsky, 2013).

Although all crossovers are thought to form in this way, not all DSBs follow this pathway and mature into crossovers. Although the number of DSBs formed is challenging to determine for technical reasons, it is clear that in all organisms, more DSBs form than crossovers, and often many more. Approximately three times as many DSBs as crossovers are likely formed in budding yeast (Buhler et al., 2007; Mancera et al., 2008) and in Drosophila (Mehrotra and McKim, 2006). In *C. elegans*, estimates of DSB number have varied, but it appears that DSBs are at least twice as numerous as crossovers (Mets and Meyer, 2009; Rosu et al., 2011; Saito et al., 2012). Mouse and humans, meanwhile, appear to generate an even greater excess of DSBs: several hundred RAD-51 foci are observed per meiotic nucleus (Baudat and de Massy, 2007), while only about a tenth as many crossovers are formed (Martinez-Perez and Colaiácovo, 2009).

DSB repair without crossover formation can occur in several ways. The most obvious but most elusive alternative is that the repair process can take place between sister chromatids—in which case, the DSB will leave no genetic signature at all. Meiosis-specific mechanisms exist to bias repair template selection towards the homolog, and away from the sister (reviewed in Hunter, 2015), but it is likely that some intersister recombination still occurs (Goldfarb and Lichten, 2010).

A second alternative outcome of DSB repair occurs when Holliday junctions that have appropriately formed between homologs are resolved to yield a tract of nonreciprocal exchange called a noncrossover. This is thought to occur when only one strand forms a Holliday junction (Kohl and Sekelsky, 2013). The choice between crossover and noncrossover formation is complex and only partially understood (reviewed in Youds and Boulton, 2011). In budding yeast, it appears to occur early in meiosis, prior to synapsis (Bishop and Zickler, 2004), while in mouse and *C. elegans* it likely occurs in pachytene (Cole et al., 2012; Yokoo et al., 2012).

Finally, crossover formation is further complicated by the existence of two different repair pathways: one requiring MSH-4/5 and one requiring MUS-81. Both pathways are active, to varying extents, in most organisms (Kohl and Sekelsky, 2013). Notably, however, it appears that only crossovers formed by the MSH-4/5-dependent pathway (‘Class I’ crossovers) exhibit interference (discussed below). The extent to which each of these pathways is predisposed to form crossovers instead of noncrossovers, or vice versa, is not clear.

Homolog pairing

Homologous chromosomes do not generally associate with one another in somatic cells or prior to meiotic entry. The earliest events of meiotic prophase involve, therefore, the stable recognition of each chromosome by its homologous partner. This

process is called pairing. Despite significant progress, a complete understanding of how it occurs has remained elusive. This is due, in part, to the fact that multiple mechanisms contribute, to varying extents in different organisms, to the pairing process. These mechanisms fall into two major categories according to whether or not they depend upon the initiation of meiotic recombination. In some organisms, both kinds of mechanisms contribute to pairing, while other organisms rely exclusively upon one or the other (reviewed in Bhalla and Dernburg, 2008; Zickler and Kleckner, 2015).

Most well-studied organisms, including budding yeast, mouse, Arabidopsis, and most other plants and mammals, rely upon recombination-dependent mechanisms to pair their homologs. In these organisms, the search for a homologous repair template that follows meiotic DSB formation is coupled to each chromosome's search for its homologous partner, so that homolog recognition occurs when the repair process has at least reached the point of strand invasion (reviewed in Zickler and Kleckner, 2015). The molecular nature of the recombination intermediate(s) that license stable pairing, however, has remained unclear. Nevertheless, work in budding yeast has revealed that meiotic recombinases possess both pro- and anti-pairing activities—presumably in order to reverse or prevent pairing at intermediates that have inappropriately formed between nonhomologous chromosomes (reviewed in Bhalla and Dernburg, 2008)—suggesting that break repair and the assessment of homolog pairing are tightly coupled.

Two prominent exceptions to recombination-dependent homolog pairing are known. In both Drosophila and *C. elegans*, pairing and synapsis occur without apparent defects in the absence of meiotic DSBs (Dernburg et al., 1998; McKim et al., 1998). Drosophila is further notable for widespread somatic pairing, though this apparently only contributes to pairing during male meiosis. In female meiosis, recent evidence indicates that germline homolog pairing initiates during the mitotic divisions that precede meiotic entry (Christophorou et al., 2013; Joyce et al., 2013); the mechanisms that underlie this phenomenon are unknown.

Homolog pairing is better understood in *C. elegans*. In this organism, short regions called Pairing Centers (PCs), located near one end of each chromosome, are responsible for stably pairing homologs (MacQueen et al., 2005). These regions are defined by the enrichment of short motifs bound by a family of zinc-finger proteins (Phillips and Dernburg, 2006; Phillips et al., 2005). These proteins mediate attachment of the PCs to the nuclear envelope (discussed below) and are specifically required for pairing of the homologous PCs they recognize (Phillips and Dernburg, 2006; Phillips et al., 2005; Sato et al., 2009). Interestingly, however, the PCs of two pairs of autosomes share the same motif and are bound by the same zinc-finger protein, indicating that homolog recognition must be determined, in part, by other mechanisms.

Some features of the pairing process are shared between all organisms, regardless of whether pairing is recombination dependent or not. In most organisms, initial contacts between particular loci—often, centromeres and/or telomeres—appear to occur almost immediately upon meiotic entry and do not, in any organism, depend on the initiation of meiotic recombination (reviewed in Klutstein and Cooper, 2014). These contacts are facilitated by tethering of the telomeres (or, in *C. elegans*, the PCs) to the nuclear periphery by a complex that spans the nuclear envelope and interacts with cytoskeletal motor proteins. This connection drives what is perhaps the most striking conserved feature of early meiosis: rapid, end-directed chromosome movements and

the concomitant clustering of chromosomes into a ‘bouquet’-like formation (reviewed in Hiraoka and Dernburg, 2009; Rog and Dernburg, 2013; Zickler and Kleckner, 2015). These rapid movements likely have several functions. In *C. elegans* and fission yeast, directed movements of the PCs and telomeres, respectively, accelerate (but are not required for) homolog pairing and, in *C. elegans*, play an important role in licensing the initiation of synapsis (Davis and Smith, 2006; Sato et al., 2009; Wynne et al., 2012). In budding yeast, they are thought to help avoid and resolve entanglements during synapsis and perhaps also eliminate ectopic recombination intermediates (Koszul et al., 2008; Storlazzi et al., 2010).

Meiotic chromosome organization

Chromosomes adopt a unique and conserved organization upon meiotic entry. This organization is catalyzed by the assembly of an array of proteins, called axial elements, into an elongated ‘core’ or axis along the length of each chromosome. These proteins include condensins, cohesins, and meiosis-specific HORMA-domain proteins (reviewed in Zickler and Kleckner, 2015). Although the molecular organization of this structure is still poorly understood, its assembly involves hierarchical interactions between the HORMA-domain proteins (reviewed in Muniyappa et al., 2014) and, its architecture, at larger scales, is speculated to resemble a dense ‘meshwork’ of axis components and chromatin (Kleckner, 2006).

A model for chromosome organization along the axis has emerged from a combination of electron microscopy, biochemical methods, and cytological observations. The core feature of this model is the existence of chromatin loops stably ‘tethered’ at intervals to the axis. Chromosomes are thought to be organized into an array of such loops emanating radially from the chromosome axis (Blat et al., 2002; Panizza et al., 2011; Zickler and Kleckner, 2015). This organization has only been directly observed in scanning electron microscopy images of chromosome spreads (Zickler and Kleckner, 1999), but it has been inferred to exist in most organisms from both the highly conserved cytological appearance of meiotic chromosomes and from chromatin immunoprecipitation experiments (Zickler and Kleckner, 2015). Results from these experiments indicate that axial elements preferentially associate with particular loci that have been interpreted to be the sites at which loops are tethered to the axis (Blat et al., 2002).

The chromosome axis plays central roles in regulating meiotic recombination and coupling it to meiotic progression (reviewed in Zickler and Kleckner, 2015). The appearance of ‘recombination nodules’ in electron micrographs of meiotic chromosomes has long made it clear that the recombination complexes responsible for forming crossovers localize to the axis in most organisms (Zickler and Kleckner, 1999). In budding yeast, this co-localization appears to occur by the recruitment of nascent DSBs to the axis (Storlazzi et al., 2010), and it is likely that axis proteins play direct roles in biasing recombination to occur between homologs rather than sisters (Goldfarb and Lichten, 2010; Hong et al., 2013). The axis also recruits components that contribute to chromosome-wide surveillance of DSB and crossover formation (Kleckner, 2006; Nabeshima et al., 2004; Panizza et al., 2011) and, in *C. elegans*, implements a checkpoint-like response to recombination defects (Kim et al., 2015).

Synapsis

Once stable homolog pairing has been achieved, the two axes of each pair of homologs serve as the template for the assembly of the synaptonemal complex (SC) during a process called synapsis. The SC is a proteinaceous structure that assembles between the axes of each pair of homologs and holds them in lengthwise alignment for the duration of pachytene (reviewed in Page and Hawley, 2004). Its appearance coincides with a striking chromosome morphology in which chromosomes resemble thick, stiff, and well-differentiated 'threads.' Indeed, the classical stage of prophase in which chromosomes are synapsed is called pachytene—Greek for 'thick threads' (Zickler and Kleckner, 1999).

The appearance of the SC in electron microscopy images is remarkable and highly conserved. It is characterized by regularly spaced transverse striations spanning the gap between homolog axes, and has given rise to the canonical view of the SC as a ladder- or zipper-like structure whose 'rungs,' called 'transverse filaments,' (TFs) span the gap between homolog axes and together holding homolog axes together (Zickler and Kleckner, 1999). The TFs consist of the protein components that have been determined, genetically and cytologically, to constitute the SC. Interestingly, although the ladder-like appearance of the SC in EM images is highly conserved, the sequence—and even number—of its protein components are not (reviewed in de Boer and Heyting, 2006). Yeast appears to possess a single TF protein (Sym et al., 1993), as does mouse (de Vries et al., 2005), though whether these are the only structural components of the SC is not clear (Fraune et al., 2012), and they are not the only proteins that associate with the SC (Zickler and Kleckner, 2015). Meanwhile, *C. elegans* has four proteins that are all required for SC assembly, localize to the SC, and presumably together form a complex that constitutes the TFs observed cytologically (reviewed in Colaiácovo, 2006; Rog and Dernburg, 2013). Notably, however, despite divergent primary sequences, the TF components from these various species appear to possess similar structural features (de Boer and Heyting, 2006).

Observations from several organisms suggest that SC assembly usually initiates at the loci or regions involved in homolog pairing. In budding yeast, for example, the proteins involved in SC initiation colocalize with recombination intermediates (Fung et al., 2004), although initiation also occurs at centromeres (Tsubouchi et al., 2008). Similar observations have been made in mouse, plants, and other organisms (reviewed in Henderson and Keeney, 2005). In *C. elegans*, synapsis has been directly visualized and shown to initiate specifically at PCs and to occur processively, irreversibly, and relatively rapidly (Rog and Dernburg, 2015). SC assembly has not been directly observed in other organisms, but given the structural conservation of the SC, these observations are likely generalizable.

The canonical description of the SC as a 'zipper' that conjoins the axes of each pair of homologs implies that the SC, once installed, is a static structure, but there is evidence that it has dynamic properties. It appears that the SC can undergo post-assembly extension into regions of unsynapsed axis (Henzel et al., 2011; MacQueen et al., 2005) and that it can incorporate new subunits after its assembly is (cytologically) complete (Voelkel-Meiman et al., 2012). Finally, in *C. elegans*, the SC appears to elongate locally in response to crossover formation (Libuda et al., 2013).

The distribution of DSBs and crossovers

Crossovers are not distributed randomly throughout the genome. Instead, in most organisms, crossovers preferentially occur at particular loci, called 'hotspots.' In turn, hotspots themselves occur more frequently within broader genomic regions and less frequently in others. These basic features of crossover distribution have been evident for decades from genetic mapping, but the mechanisms responsible for generating them have been challenging to elucidate. Recently, high-resolution measurements of the distribution of meiotic DSBs have been made by performing ChIP against recombination proteins and by sequencing SPO-11-bound oligos. These measurements have shown—with the exception of fission yeast (Hyppa and Smith, 2010)—that the distribution of crossovers generally mirrors the distribution of DSBs, and have begun to shed light on the genetic and epigenetic determinants of hotspot positioning (reviewed in de Massy, 2013).

Across the organisms in which high-resolution hotspot maps have been measured or inferred, the most consistent correlate of hotspot positioning is enrichment of histone modifications associated with transcriptionally active chromatin, including, most prominently, H3K4me3. In buddying yeast, this correlation likely reflects recognition of this modification by Spp1, a Spo11-accessory factor involved in recruiting DSB sites to the chromosome axis (Sommermeyer et al., 2013). Local chromatin structure is also important in both budding and fission yeasts, as hotspots almost exclusively occur in nucleosome-depleted regions, likely because the DSB machinery in these organisms requires accessible chromatin (de Massy, 2013).

Meanwhile, in mouse, humans, and most other mammals, hotspots are correlated with H3K4me3 but do not necessarily occur in open chromatin. Instead, a protein called PRDM9 appears to determine the distribution of hotspots (reviewed in Baudat et al., 2013). PRDM9 possesses a zinc-finger domain that recognizes a motif whose distribution almost exactly matches the hotspot distribution; different PRDM9 alleles recognize different motifs and give rise to correspondingly different hotspot distributions. PRDM9 also possesses a methyltransferase domain that can catalyze H3K4me3, explaining the hotspot-proximal enrichment of this modification (de Massy, 2013). However, the roles played by this modification, as well as how PRDM9 interacts with the DSB machinery, remain unclear. And, while most vertebrates carry PRDM9, some lineages have lost it, indicating that compensatory mechanisms exist (or can evolve) to distribute DSBs in mammals.

The distribution of DSBs has not been directly determined in other organisms, but hotspots appear to be a primary feature of the crossover distributions in most organisms, including Drosophila (Comeron et al., 2012) and Arabidopsis (Lu et al., 2012). The most notable exceptions to this generality are fission yeast and *C. elegans*, in which prominent hotspots do not exist (Hyppa and Smith, 2010; Kaur and Rockman, 2014). In *C. elegans*, crossovers are instead substantially enriched in the terminal regions of each chromosome, which receive approximately 90% of the crossovers but correspond to only about half of the genome (Barnes et al., 1995; Brenner, 1974; Rockman and Kruglyak, 2009). These regions are called the chromosome 'arms.' They differ in several ways from the chromosome centers. They are less gene-dense, they have more repetitive sequence, and their introns are larger (*C. elegans* Sequencing Consortium, 1998). Most surprisingly, given the enrichment of crossovers within them,

the arms are strongly enriched for histone modifications associated with heterochomatin and transcriptional silencing (Liu et al., 2011). Measurement of the DSB distribution by ChIP-seq against RAD-51, however, has revealed that local enrichment of H3K4me3 at DSB sites coexists with these large-scale heterochromatin-like properties of the arms (Ho et al., 2014).

Crossover homeostasis and interference

The number and distribution of crossovers are both highly regulated. The number of crossovers is subject to two constraints. First, because crossovers are required for chromosome segregation, at least one crossover must form between each pair of homologs—this is called the obligate crossover. In principle, formation of this crossover could be passively guaranteed by forming such a high number of crossovers that the probability of any one chromosome receiving zero crossovers would be negligible. Because most organisms form only a few crossovers per chromosome, this is evidently not a prominent strategy, and active mechanisms must instead exist (Martinez-Perez and Colaiácovo, 2009; Wang et al., 2015).

While one crossover is essential, too many crossovers are likely deleterious—if not to the mechanics of meiosis, then to its evolutionary benefits (Hunter, 2015). In consequence, a phenomenon called crossover homeostasis exists to buffer the number of crossovers from fluctuations in the number of DSBs by appropriately adjusting the ratio of crossovers to noncrossovers. Such fluctuations likely occur endogenously, but can also be introduced exogenously either by genetic perturbation of the DSB machinery or by irradiation. First discovered by studying hypomorphic alleles of Spo11 in budding yeast (Martini et al., 2006), homeostasis has since been observed in Drosophila (Mehrotra and McKim, 2006), mouse (Cole et al., 2012), and *C. elegans* (Hillers and Villeneuve, 2003; Rosu et al., 2011; Yokoo et al., 2012), and is likely to be a conserved feature of meiotic recombination.

Perhaps the most mysterious feature of crossover regulation is a phenomenon called crossover interference, which describes the observation that crossovers tend not to occur close together but are instead evenly spaced throughout the genome. This interference effect, first discovered in Drosophila a century ago (Muller, 1916) and subsequently observed in almost all eukaryotes, operates over significant portions of each chromosome, implying that biochemical information (i.e., the presence of a crossover) is somehow communicated or ‘propagated’ along chromosomes over millions of base pairs and microns of chromosome axis contour length (reviewed in Hillers, 2004; Hunter, 2015). The mechanism(s) responsible for imposing crossover interference, as well as the medium that propagates the interference signal along chromosomes, have remained one of the enduring mysteries of meiosis, both because it is technically demanding to measure and because few genetic mutants exist that specifically perturb it (Hillers, 2004)

Several models for interference have been proposed: a ‘counting’ model in which each crossover is separated by some fixed number of noncrossovers (Lande and Stahl, 1993); a model in which the signal is the ‘spreading’ or polymerization of some biochemical modification along the chromosome (Kleckner, 2006), and, most recently, a model in which the signal is instead coupled to mechanical stress within the chromosome (Kleckner et al., 2004). A recent report that topoisomerase II is specifically

responsible for implementing interference in budding yeast argues for the latter stress-based model (Zhang et al., 2014). Notably, an interference effect between DSBs—a possibility first raised by the observation of interference between noncrossovers and crossovers (Mancera et al., 2008)—has recently been detected directly in budding yeast (Garcia et al., 2015), adding to the evidence that interference is likely imposed at an early stage of meiosis in that organism (Bishop and Zickler, 2004; Börner et al., 2004; Fung et al., 2004) and arguing against models in which the SC, if not the axis itself, propagates the interference signal. However, in *C. elegans*, perturbation of the SC by depleting one of its components diminishes the strength of interference (Hayashi et al., 2010; Libuda et al., 2013), arguing that the SC is not dispensable for interference in all organisms. Evidence from mouse and *C. elegans* suggests that interference may be implemented in stages, allowing for the possibility that interference is implemented sequentially by multiple mechanisms (de Boer et al., 2006; Reynolds et al., 2013; Rosu et al., 2011).

Overview of presented work

Crossover formation is regulated on length scales ranging from the local enrichment of crossovers at hotspots to the chromosome-wide effect of interference. Our molecular understanding of this regulation and its relationship to meiotic chromosome organization has emerged principally from population-based biochemical methods. Meanwhile, our understanding of large-scale chromosome organization, the SC, and dynamic chromosome-wide behaviors has relied on low-throughput immunofluorescence or live imaging of meiotic chromosomes. Although much has been learned from this approach, it is limited by the laboriousness and difficulty of extracting quantitative information from complex images.

To understand the relationship between large-scale chromosome organization and the chromosome-wide regulation of recombination during meiosis, we developed an image analysis pipeline to computationally segment and trace meiotic chromosomes in a semi-automated fashion. This method, discussed in Chapter 2, bridges the gap between high-throughput population-based biochemical assays and low-throughput but context-rich cytological methods. This allows us to monitor the dynamics of chromosome organization and the distribution of DSBs during meiotic prophase.

In Chapter 3, the descriptive results from using this technique to quantify both chromosome organization and the distribution of DSBs and crossovers in *C. elegans* are discussed. We find that the distribution of DSBs is dynamic during prophase and shifts in mid-pachytene from a distribution that mirrors the distribution of crossovers to one that is more uniform. This shift correlates with isotropic, recombination-independent elongation of chromosomes and is insensitive to defects in recombination and variation in the number of DSBs.

Finally, in Chapter 4, preliminary results from a separate project to observe interactions between homologous chromosomes are discussed. This project relies upon a novel method for the design of FISH probes (Beliveau et al., 2015) that enables the synthesis of homolog-specific probe pairs. Using this technique, we show that homologous regions are usually well-separated from one another during meiotic prophase, with the prominent exception of regions within pairing centers in the transition zone.

Chapter 2 Automated image analysis of meiotic chromosomes

Introduction

Dramatic reductions in the cost of computing power and storage capacity in the last several decades have enabled both the acquisition of vast quantities of biological data and the use of sophisticated algorithms to analyze them. In cell biology, these developments have dramatically expanded the capabilities of fluorescence microscopy. Traditionally a technique used to make qualitative cytological observations, fluorescence microscopy is now used to make quantitative measurements of cellular structures and dynamics, often at resolutions that significantly surpass the diffraction limit.

This new era in biological imaging holds great promise for chromosome biology, and for the study of meiosis in particular. Meiotic chromosomes are large structures whose organization and interactions both lend themselves to cytological visualization and play central roles in the meiotic program. Indeed, the history of the cytological study of meiosis spans nearly a century, and much of what we know about meiotic chromosomes has been gleaned from careful inspection of both electron- and light-microscopic images of meiotic nuclei. However, efforts to quantify chromosome organization have so far been limited by the difficult and time-consuming task of identifying and tracing meiotic chromosomes in three-dimensional images. In this chapter, I discuss the development of a computational approach—developed for images of meiotic nuclei in the nematode *C. elegans*—that can perform these tasks semi-automatedly and relatively rapidly.

Several features of *C. elegans* make it a particularly powerful system for the cytological analysis of chromosome organization throughout meiotic prophase. Meiotic nuclei migrate through the gonad as they progress through meiosis, resulting in a gradient of meiotic stages within a single gonad. Together with the organization of nuclei as a monolayer on the surface of the syncytial gonad, this spatio-temporal gradient permits the imaging of a large number of staged nuclei within a single field of view in whole-mount gonads. The gonads can be dissected from the body of the animal, so that well-preserved meiotic nuclei can be imaged in three dimensions. Finally, a critical advantage is the ability of light microscopy to resolve all six pairs of synapsed chromosomes in meiotic nuclei—a consequence of both the simple karyotype of *C. elegans* and the dispersed organization of synapsed chromosomes within each nucleus.

Published efforts to quantify images of meiotic chromosomes in *C. elegans* fall into two categories. In the first, some parameter of interest—for example, whether chromosomes have paired or synapsed or have formed DSBs—is determined by eye for each nucleus in multiple gonads. By dividing the gonad into several subregions, the change in this parameter as nuclei progress through prophase can be determined. These assays are powerful because they can detect relatively subtle defects in pairing, synapsis, and recombination, and a large body of work relies upon them.

A second existing approach to extracting quantitative information from images of meiotic chromosomes has relied upon visualization software that enables the investigator to manually select points in a three-dimensional image and thereby generate a trace along the chromosome of interest. Although it allows for the

measurement of chromosome-specific quantities like contour length and DSB and crossover distributions, this method has not been widely adopted in the literature, presumably because it is labor intensive and requires high-resolution three-dimensional images. Nevertheless, it has proven sufficient to detect significant differences in chromosome length or in the distribution of cytological markers of crossovers (Libuda et al., 2013; Mets and Meyer, 2009; Nabeshima et al., 2011; Saito et al., 2012). These datasets are not, however, large enough to quantify variation in axis length or detect subtle differences between DSB or crossover distributions. Moreover, they are labor-intensive, imprecise, and subject to user bias in the selection of traced chromosomes.

These two approaches to quantitative cytology have not yet been combined to measure how properties of single chromosomes changing during prophase, because doing so requires tracing, in three dimensions, most of the chromosomes in most nuclei in multiple gonads—a formidable task to accomplish by hand. This chapter describes a computational image analysis pipeline that overcomes this challenge by automating the laborious process of identifying and tracing single chromosomes. Along the way, several other limitations of manual quantification are overcome, including the unbiased identification of bright fluorescent foci and the generation of unbiased centroid-based chromosome traces that allow for measurements of chromosome axis curvature.

RESULTS

Overview

The task of computationally identifying and tracing synapsed meiotic chromosomes consists of three major components: first, the segmentation of individual nuclei from a field of view; second, the segmentation of individual chromosomes from cropped images of single nuclei; and third, the generation of a curve that traces along the ‘backbone’ or ‘core’ of each segmented chromosome. Here, we discuss solutions to each of these three problems; a graphical overview of their solutions is shown in Figure 2.1. Of course, prior to these computational challenges, the methodological challenge of acquiring bright, high-resolution, three-dimensional images of well-preserved nuclei must be surmounted. There are several approaches to doing so; these are discussed in the *Methods* section below. In practice, we found that using linear structured illumination microscopy (SIM) yielded the highest quality images and was necessary to resolve chromosome axes in early pachytene (Figure 2.6). In all cases, our analysis is restricted to the co-aligned axes of synapsed chromosomes. Staining of the chromosomes themselves yields much wider structures that would be challenging to differentiate, while prior to synapsis, chromosome axes are too tightly intermixed to resolve. For the sake of brevity, we will refer to the computational segmentation and tracing of the axes of synapsed homologs as ‘chromosome segmentation’ and ‘chromosome tracing,’ even though our analysis relies upon images of synapsed axes, rather than staining of the chromosomes themselves.

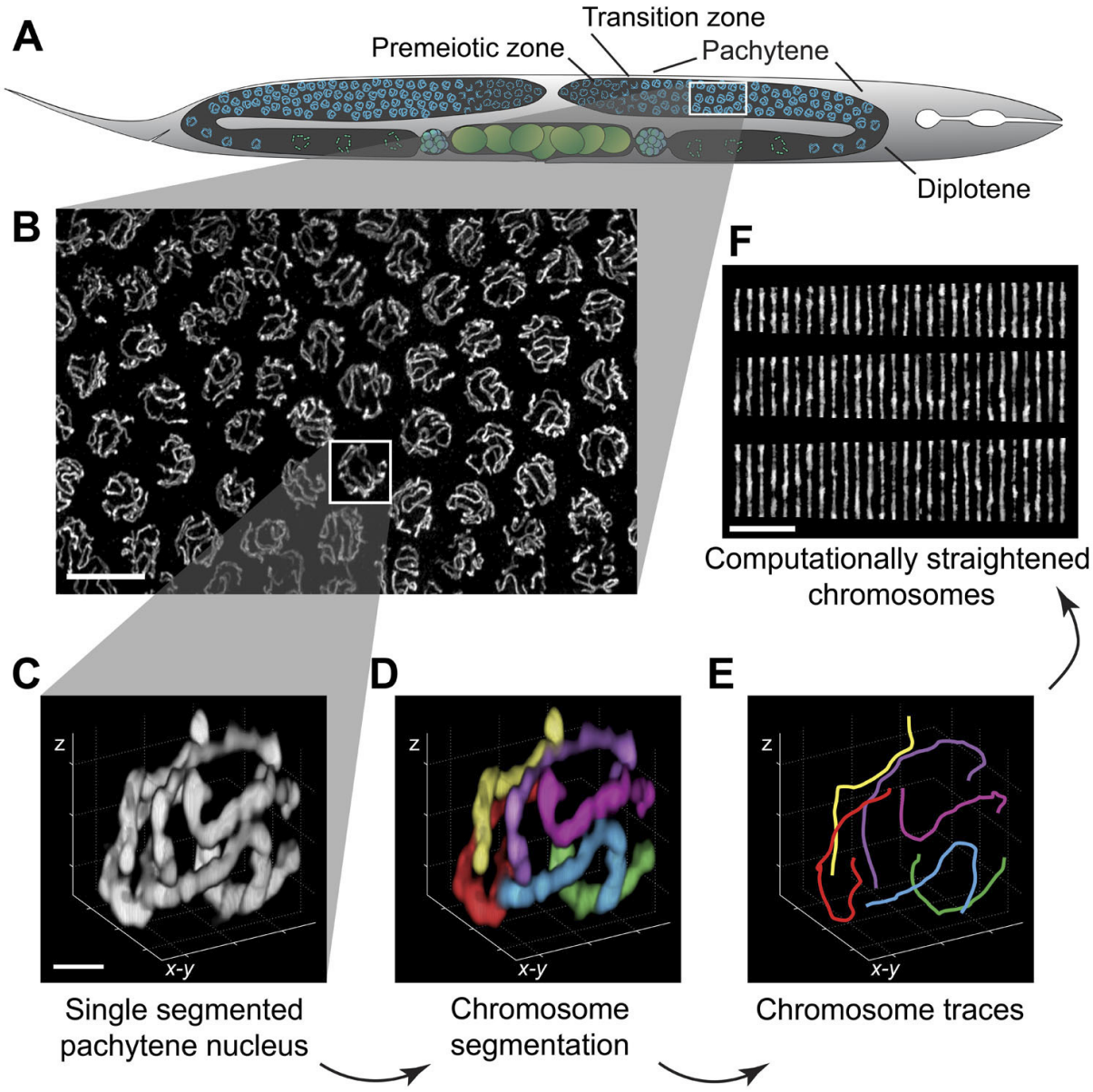


Figure 2.1 Overview of analysis pipeline for automated segmentation and tracing of pachytene chromosomes
(A) Overview of the *C. elegans* germline in hermaphrodites. Pachytene nuclei occupy the proximal half of each gonad arm. (B) Projection of a three-dimensional SIM image of mid-pachytene nuclei stained for axis component HTP-3. Scale bar, 5μm. (C) Volume visualization of a single pachytene nucleus isolated from the projection in (B). The vertical axis is the Z, or axial, direction. Scale bar, 1μm. (D) Output of the chromosome segmentation algorithm, visualized by coloring each different chromosome axis in a different color. (E) Output of the chromosome tracing algorithm, visualized as a 3D plot of each trace, colored according to the color of its corresponding axis. (F) A sample of the output of the segmentation and analysis pipeline. Individual chromosomes have been segmented, traced, and computationally straightened. Scale bar, 5μm.

Segmentation of single nuclei

In well preserved tissue, individual pachytene nuclei are usually well-separated from one another. In principle, chromosome staining itself could be used to segment nuclei, but it is computationally simpler to use axis staining itself to segment nuclei. An accurate segmentation can be obtained by thresholding a bandpass-filtered raw image of axis staining. The bandpass filtering removes both high-frequency noise (usually due to 'splotchy' background immunofluorescence staining) and low-frequency noise (usually due to variation in the intensity of the excitation light) (Figure 2.1B). The threshold is 'guessed' using Otsu's method and then adjusted manually as necessary for each image.

The raw segmentation that this algorithm yields is not perfect. Because synapsed chromosomes are often well-separated from each other, even this rudimentary algorithm often successfully segments some chromosomes from others in a single nucleus. This is undesirable behavior, because it means that single nuclei are often not represented as contiguous regions in the segmentation, but instead consist of several smaller regions (Figure 2.1C). This over-segmentation problem is corrected using K-means clustering of the centroids of all regions that are too small to correspond to an entire nucleus. This clustering procedure exploits the fact that, because synapsed chromosomes tend to be confined to the nuclear periphery, each over-segmented region usually lies within a concave surface facing the center of its corresponding nucleus. This, in turn, means that the centroids of over-segmented regions are biased to lie near the center of their corresponding nuclei and therefore that identifying centroid clusters is usually equivalent to identifying single nuclei. Once this region merging operation has been completed, a relatively accurate nucleus segmentation is obtained (Figure 2.1D).

Segmentation of chromosome axes

Following nucleus segmentation, each nucleus is cropped from the raw three-dimensional image stack and chromosome segmentation performed on each nucleus separately, allowing us to exploit the constraint that each nucleus contains six chromosomes. Although the axes of single synapsed homolog pairs are resolvable by eye and sometimes segmented even by our simple nucleus segmentation algorithm, adjacent synapsed chromosomes are usually too closely spaced for simple segmentation techniques to separate them (Figure 2.3A). This is usually because of variation in intensity and contrast—so that, for example, the local minimum intensity between two adjacent chromosomes is greater than the maximum local intensity along a single chromosome elsewhere in the same nucleus. This kind of variation is likely due both to intrinsic noise in immunofluorescence staining and to biological variation in the density of axis components between and along chromosomes.

To robustly segment chromosomes using axis staining, then, the local minima in axis staining intensity must be identified, and only those minima that correspond to the border between adjacent chromosomes must be retained in the final segmentation. To identify local minima, we applied the watershed transform (Meyer, 1994) to a lowpass-filtered axis fluorescence image. The watershed transform identifies the boundaries between 'watersheds' in a grayscale image—that is, the ridges of local maxima that

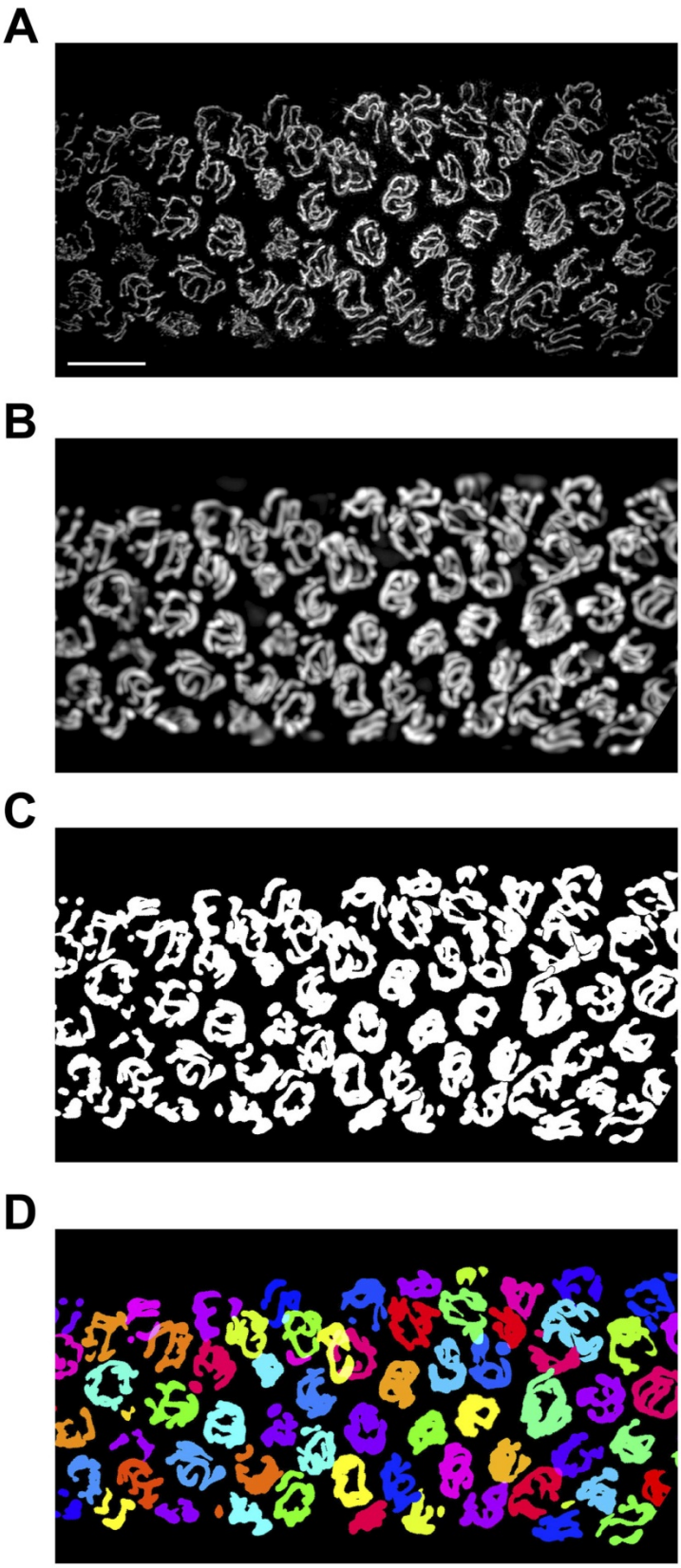


Figure 2.2 Overview of nucleus segmentation
(A) Example projection of a single SIM image of HTP-3 staining in early pachytene. (B) The first step in nucleus segmentation: a bandpass-filtered image in which low-frequency and high-frequency noise has been eliminated. (C) The mask that results from simple binary thresholding applied to the image in (B). (D) Final output of the nucleus segmentation algorithm, following clustering of the regions in the binary mask in (C) into nuclei, each of which here colored differently. Scale bar, 5μm.

encircle each local minimum. By applying the watershed transform to individual nuclei, masked by the nucleus mask generated during nucleus segmentation, we obtain a set of boundaries that lie both along single chromosomes and between different, but adjacent, chromosomes. These boundaries are shown in red in Figure 2.3B. Invariably, most of these watershed boundaries are spurious—that is, they lie between local maxima within a single chromosome, thereby 'chopping' a single chromosome into several smaller regions. To remove these spurious boundaries, the fact that each chromosome is, topologically, a line segment without intersections or loops, and the fact that each nucleus contains six chromosomes of approximately equal axial length, are exploited using an algorithm described below and inspired, conceptually, by a segmentation algorithm developed to segment adjacent bacterial cells (Wiggins et al., 2010).

First, all of the watershed boundaries are retained, yielding an over-segmented image (Figure 2.3B). Next, the watershed boundary that is most likely to be spurious is removed from the image. The likelihood that a boundary is spurious is calculated using several of its properties, including the absolute intensity of the ridge along which it lies, the relative contrast of that ridge, its orientation (since resolution is always worse in the *z*-direction, surfaces that are parallel to the *x*-*y* plane are less likely to be spurious), and its surface area. After removing the first boundary, two of the regions will have been merged together. Properties of this new region—its volume, surface area, and topology—are calculated to determine whether it now corresponds to a single pachytene chromosome. Topology is assessed using a skeletonization algorithm that erodes the binary segmentation volume until it is as small as possible without altering its topology—so that, for example, a spherical volume erodes to a single pixel, a filament- or sausage-like volume erodes to a line of pixels, and a donut erodes to a circular loop of pixels (Figure 2.4C). If the new region resembles a full chromosome, then it, and all watershed boundaries that border it, are excluded from further optimization and marked as correctly segmented. If the new region cannot be a single chromosome—if, for example, it is a loop or a branched structure—then the boundary that was removed is instead added back and removed from the set of possibly non-spurious boundaries. This procedure is then iterated: watershed boundaries are removed one by one from the image in order of estimated spuriousness while at each step the merged regions are tested for correspondence with the expected size and topology of a single chromosome. The procedure is stopped automatically once six such 'real' regions have been obtained (Figure 2.3C).

This chromosome segmentation algorithm can fail in several ways, even when the underlying image is 'perfect' in the sense that the axis staining is sufficiently bright and detectable local minima exist between all adjacent chromosomes. The most common mode of failure is due to error in the order in which watershed boundaries are removed from the image—if a spurious boundary is removed before a real boundary, then the result is often a segmentation that conjoins adjacent chromosomes. This error occurs because of the intrinsically probabilistic nature of the boundary sorting algorithm, and also because of variation in the estimate of each boundary's probability of being spurious. Another kind of failure occurs when a merged region is either wrongly determined to correspond to a single chromosome. This failure is due to intrinsic variation in chromosome axis length and volume.

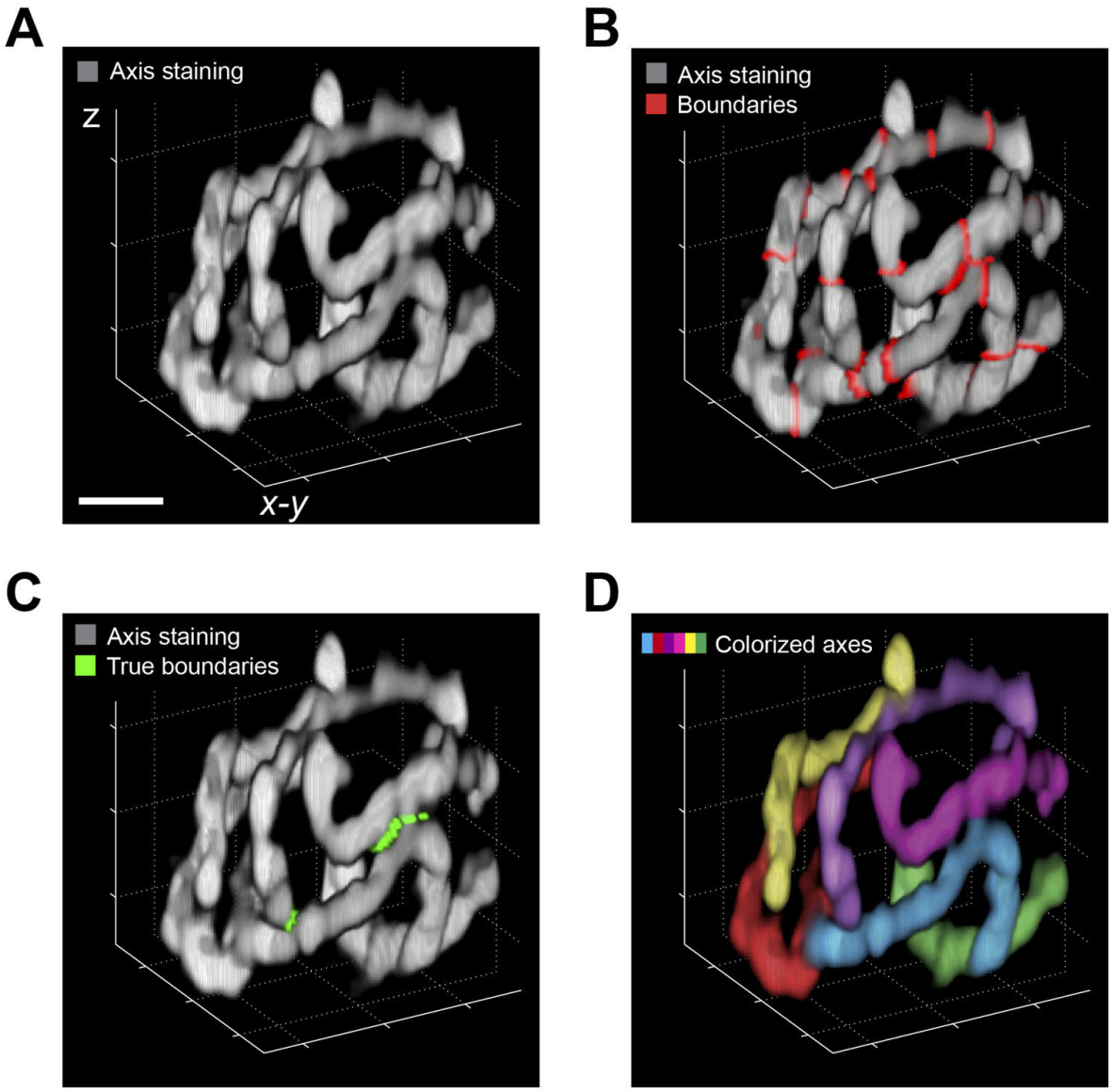


Figure 2.3 Chromosome segmentation using iterative region merging
(A) Volume visualization of a single pachytene nucleus, stained for axis component HTP-3. The vertical direction is the *z*-dimension. Note the adjacent chromosomes at center left. (B) Output of the watershed algorithm applied to the axis staining in (A), visualized by highlighting the surfaces between adjacent watersheds in red. Note that the 'real' boundary between adjacent chromosomes has been detected, but many spurious intra-chromosomal boundaries have also been generated. (C) Result of iteratively removing the boundaries in (B) until six appropriate chromosome-like volumes have been obtained. The 'real' boundaries between adjacent chromosomes have been retained and are now highlighted in green. (D) Following identification of 'real' watershed boundaries, each chromosome can be manipulated individually—here illustrated by artificially coloring the axis staining of each chromosome differently. Scale bar, 1μm.

The segmentation algorithm can also fail when the axis staining is imperfect. This can occur if two adjacent chromosomes are positioned so closely together that, at the resolution of light microscopy, a local minimum in axis staining intensity does not exist. In this case, the segmentation algorithm will usually over-segment both of the two unresolvably adjacent chromosomes. The segmentation can also fail when dramatic differences in axis staining intensity exist within the nucleus—which can occur when antibody penetration into the tissue is poor. This results, in the best case, in very poor estimates of the probability that each boundary is spurious. In more severe cases, it results in error in the background mask, which is a prerequisite for the segmentation algorithm itself.

Supervised segmentation correction

Some of the segmentation errors described above can be corrected by human intervention. A GUI was created to allow a human operator to inspect the chromosome segmentation in each nucleus in each field of view. The visualization problem posed by this task was solved by displaying a three-dimensional surface, corresponding to the region created by merging all watershed regions, with boundaries between watersheds highlighted and labeled graphically. The color of the watershed boundaries indicated whether the segmentation algorithm had chosen to remove them from the image. By selectively adding or removing boundaries according to their numerical label, the user is able to correct the segmentation to the extent that the quality of the underlying axis staining permits.

Chromosome tracing

The final output of the segmentation algorithm described above is a set of filament-like volumes that occupy the regions in the nucleus corresponding to the axis staining of each pair of synapsed chromosomes. The cross-sectional extent of this staining at each point along the chromosomes is due both to diffraction—each axis alone is a diffraction-limited ‘thread’—and to the fact that synapsed axes are separated by the 100nm-wide transverse filaments of the SC. Measuring properties of synapsed chromosomes, like contour length and curvature, requires eliminating this substantial cross-sectional area to yield a three-dimensional curve that follows along the ‘backbone’ or longitudinal center of each filamentous segmentation volume. This curve is what we refer to here as a chromosome trace.

A crude approximation to this curve can be generated by using the binary skeletonization algorithm described previously. This algorithm reduces each filamentous volume to a pixelated curve that, topologically, resembles the original volume (Figure 2.4C). Because the algorithm works by iteratively eroding the initial volume, the final skeleton tends to lie along the center of the chromosome. However, because the algorithm operates on pixels, the skeleton is necessarily discretized by pixel size. The end points of the skeleton also do not correspond to the true chromosome ends (as delimited by the axis staining). To overcome these limitations and to generate a curve that extends to the ends of the chromosome, an active contour model was used to refine the crude curve generated by skeletonization.

Active contour models refer to algorithms that deform a curve (i.e., a contour) that has been overlaid on an image (either by a human user or another algorithm)

according to features of the underlying image (Caselles et al., 1997). Traditionally, such models have been used to precisely identify edges in an image from an approximation provided by a human user, but they can just as easily be used to trace local 'ridges' of intensity. In all cases, the deformation of the curve is accomplished by subjecting the initial, approximate curve to an 'energy' or cost function derived from the underlying image, such that the energy of the curve is minimized when the curve exactly coincides with the feature of interest—for example, an edge—in the original image. Mathematically, this procedure requires two steps: first, creating an appropriate energy or cost functional for the curve, and, second, using a numerical minimization algorithm to find the curve that minimizes that functional.

To apply this approach to refining the pixelated chromosome traces generated by skeletonization, the pixelated traces themselves are used as the initial, approximate curve. The problem is then reduced to designing an energy or cost functional whose minimum corresponds to the curve that both lies along the 'core' or cross-sectional center of the axis staining and has endpoints that correspond to the ends of each chromosome. The first constraint is straightforward to implement: an energy term proportional to the sum of the staining intensity at each point along the curve ensures that the curve follows the path of greatest intensity through the chromosome. The second constraint is enforced using an energy term that depends on the derivative of the intensity along the tangent to the curve at each endpoint. This biases the endpoints of the curve to coincide with the (very narrow) 'edge' corresponding to the end of the axis staining. These two image-dependent energy terms are empirically weighted relative to an internal energy term that resists changes in the overall contour length of the curve to prevent the trace from overshooting the ends of the axis staining or shrinking to a point. Finally, an additional internal energy term enforces local continuity in the curve, so that 'kinks' in the curve sharper than those resolvable by light microscopy cannot occur.

The final step, once the energy functional is constructed, is to identify the curve that minimizes it (Figure 2.4D). There are many optimization algorithms, of varying sophistication, that can be used to iteratively approach the minimum by deforming an initial estimate of this curve. Because the initial estimate for the chromosome trace—the skeletonized segmentation volume—is usually very close to the final trace, it is sufficient to use classic gradient descent to find the local minimum in the energy functional. Animating the iterative solutions generated by this algorithm yields a curve that appears to 'find' and 'snap' into the correct place. Typically, twenty iterations are sufficient to yield a stable solution, and the solution is rarely spurious (i.e., a trace that extends beyond the ends of the chromosome or has spurious loops or kinks).

Chromosome straightening

Once the chromosome trace has been determined, it is possible to computationally straighten or 'unbend' the chromosome axis staining. This was accomplished by interpolating a two-dimensional image slice from the three-dimensional axis intensity along the plane normal to the trace at evenly spaced contour-length intervals along the axis. These slices are then 'stacked' to generate a new three-dimensional image whose third dimension now corresponds to axis contour length; this image can be projected in any cross-sectional direction to yield a two-dimensional

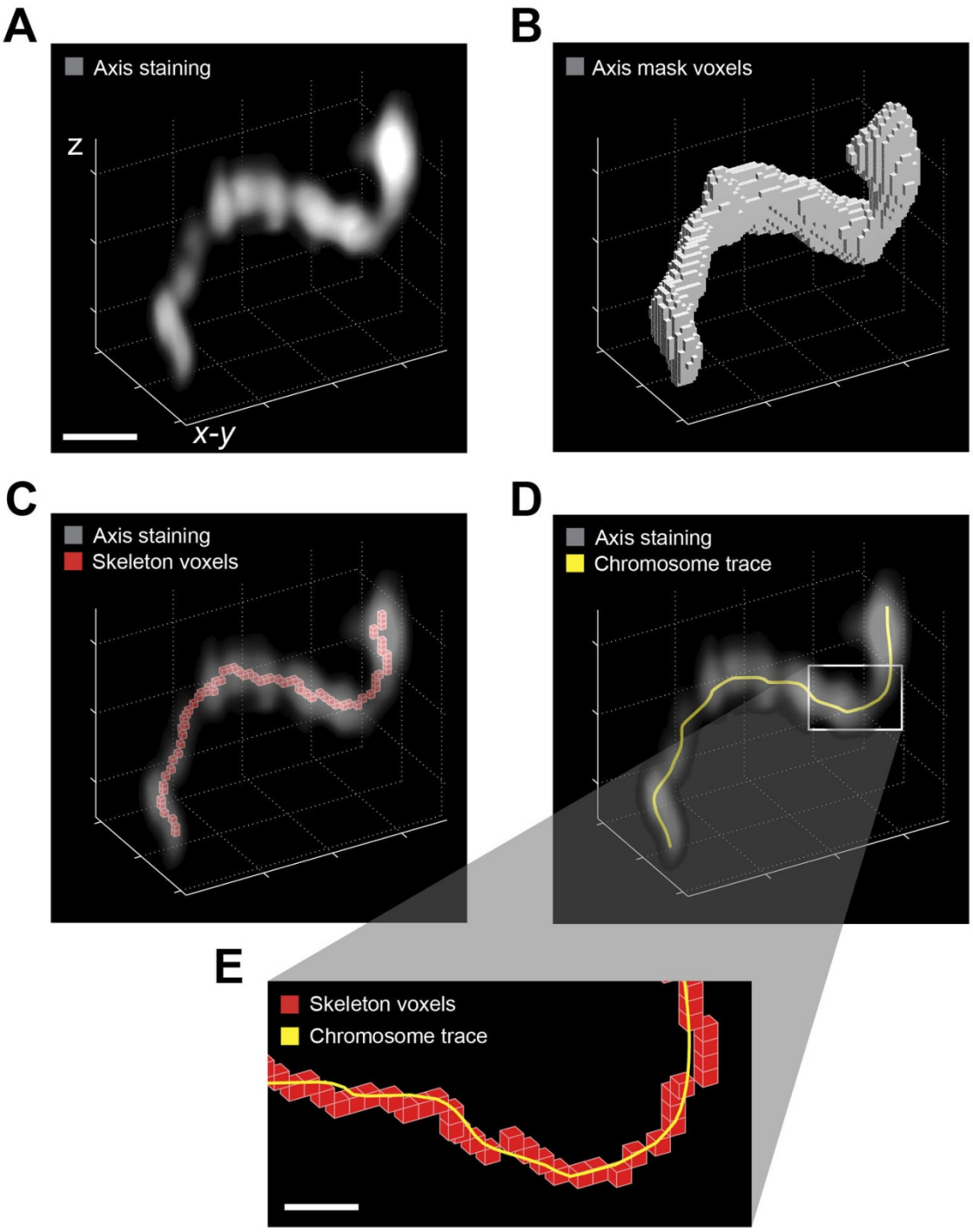


Figure 2.4 Chromosome tracing using skeletonization and active contours
(A) Volume visualization of a single segmented chromosome, computationally isolated from its nuclear context. (B) Three-dimensional representation of the binary mask generated by the segmentation algorithm. (C) The result of skeletonizing the binary region in (B), overlaid on the original axis staining. (D) The result of using an active contour to refine the coarse trace provided by the skeletonized mask. Scale bar, 500nm. (E) Magnified view of the final trace with the skeleton superimposed to illustrate the refinement and subpixel resolution provided by the active contour. Scale bar, 100nm.

image of the straightened axis (Figure 2.1F). Although this procedure is not necessary to calculate chromosome length, curvature, or contour length position of markers of interest, it is a useful visualization technique.

Three-dimensional fluorescent focus localization

Markers for recombination intermediates, including the repair factor RAD-51 (Alpi et al., 2003; Ogawa et al., 1993) and crossover-associated protein COSA-1 (Yokoo et al., 2012) appear cytologically as diffraction-limited foci. We developed a simple algorithm to automatedly detect these foci and determine their positions. First, the raw image is smoothed to eliminate high frequency noise. Next, all local maxima brighter than an empirically determined threshold are considered candidate foci, and their positions, widths, and intensities determined by fitting each to a three-dimensional Gaussian function. Finally, candidate foci that are sufficiently symmetric (i.e., are truly diffraction-limited) and sufficiently close to a chromosome trace are defined to be true foci, and their positions retained for subsequent analysis.

Measuring nucleus position

The final step in the analysis pipeline described here is the determination of the location in the gonad of each analyzed nucleus. This is accomplished in two steps. In the first, a low-resolution whole-gonad mosaic is generated, its ‘spine’ or center is marked by hand, and the positions of the high-resolution fields of view in this mosaic determined (Figure 2.5). This process is accomplished by hand. Next, the position of each analyzed nucleus within its field of view is determined computationally using a cross-correlation algorithm. Finally, the position of each nucleus along the ‘spine’ of the whole gonad, relative to the start of the transition zone (also marked by hand) is calculated. Meiotic progression is quantified by the number of rows of nuclei that lie between the start of the transition zone and each nucleus. These rows are marked by hand (Figure 2.5).

DISCUSSION

Automation and its limits

The image analysis pipeline we have described here is, in principle, fully automated. However, in practice, the substantial variation in staining intensity along synapsed chromosome axes—likely to some extent biological and to some extent an artifact of immunofluorescence staining—diminished the frequency with which the chromosome segmentation algorithm could successfully differentiate between real and spurious watershed boundaries. This limitation is intrinsic to the design of the segmentation algorithm, which evaluates watershed boundaries based only on local properties like boundary size and image intensity along the boundary. Incorporating information about the image context in which each boundary occurs—for example, the topology of the background mask—would improve the performance of the algorithm but is computationally intensive and mathematically complex.

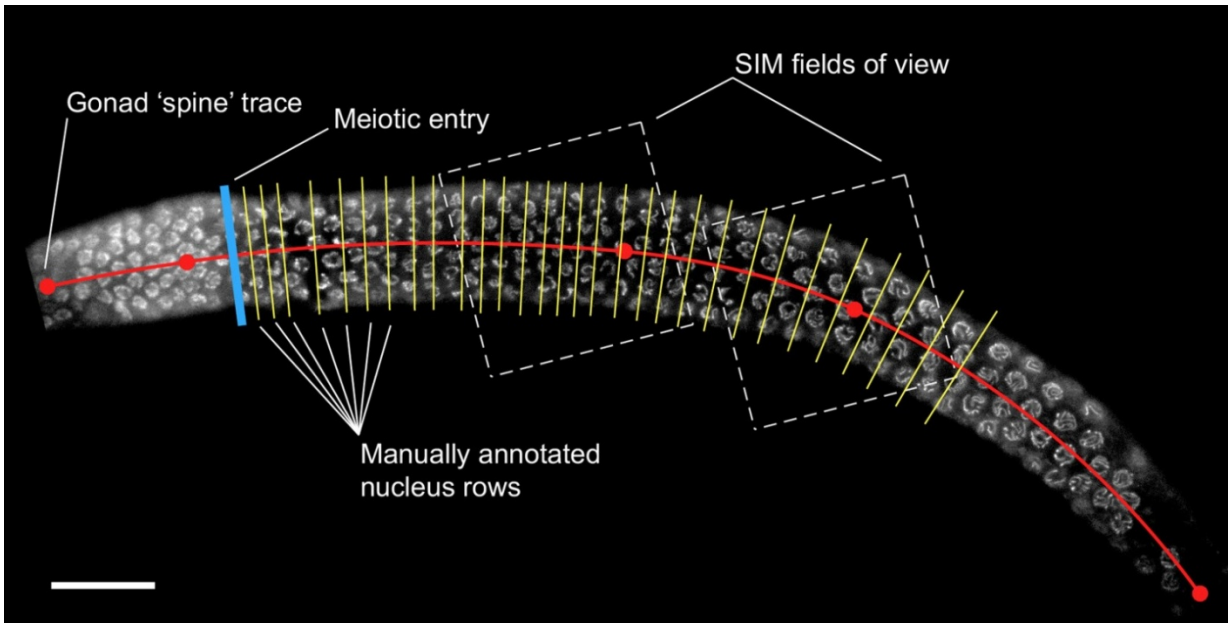


Figure 2.5 Methodology for measuring the position of nuclei within the gonad
A gonad spine (red), the point of meiotic entry (blue bar), and each row of nuclei (yellow lines) are all annotated manually. An automated algorithm locates each analyzed nucleus in each SIM field of view and determines its overall position in the gonad in terms of the number of rows between it and meiotic entry. Scale bar, 20μm.

In practice, given the need for human supervision, the throughput of the pipeline was sufficient to generate datasets consisting of thousands of traced and staged chromosomes with associated markers from tens of hours of human labor. The unsupervised computation time required, using a single desktop computer, was on the order of hours per thousand chromosomes. The human and computation time required varies significantly with the quality of the raw images and the stage of pachytene (early pachytene nuclei, for example, almost always require supervision). On average, this throughput likely represents an improvement of approximately an order of magnitude over previous unautomated approaches to meiotic chromosome segmentation and tracing in *C. elegans*. Without the need for supervision during chromosome segmentation, throughput would likely increase by an additional order of magnitude and become limited by the human labor required for sample preparation and image acquisition. However, this further improvement would require a novel and more powerful segmentation algorithm. In the absence of an obvious need for datasets consisting of tens of thousands, rather than thousands, of chromosomes, such an algorithm will likely remain undeveloped.

Imaging technologies

The robustness of the approach described here does not depend upon imaging modality, image resolution, or axis staining method—so long as the staining intensity does not vary too dramatically over the field of view and the resolution is sufficiently high that local minima exist between adjacent chromosomes. In practice, we have found that the resolution of both confocal microscopy and standard widefield deconvolution microscopy is sufficient to segment the majority of chromosomes in mid- and late pachytene nuclei. In early pachytene, however, when chromosomes have not completely lost the polarized morphology of the transition zone and tend to be clustered very close to one another, the *z*-resolution of these standard imaging technologies is not sufficient to robustly differentiate between adjacent chromosomes.

To overcome this limitation, we paired our automated analysis with linear structured illumination microscopy (Gustafsson, 2000). This super-resolution imaging modality, in theory, doubles the resolution of widefield microscopy and, when applied in three dimensions, yields true optical sectioning, dramatically improving contrast in the *z*-direction (Gustafsson et al., 2008). In practice, the resolution we obtained fell slightly short of the theoretical expectation, likely due to aberrations in the patterned illumination introduced by the intervening tissue, but remained sufficient to permit segmentation of chromosomes in early pachytene (Figure 2.6).

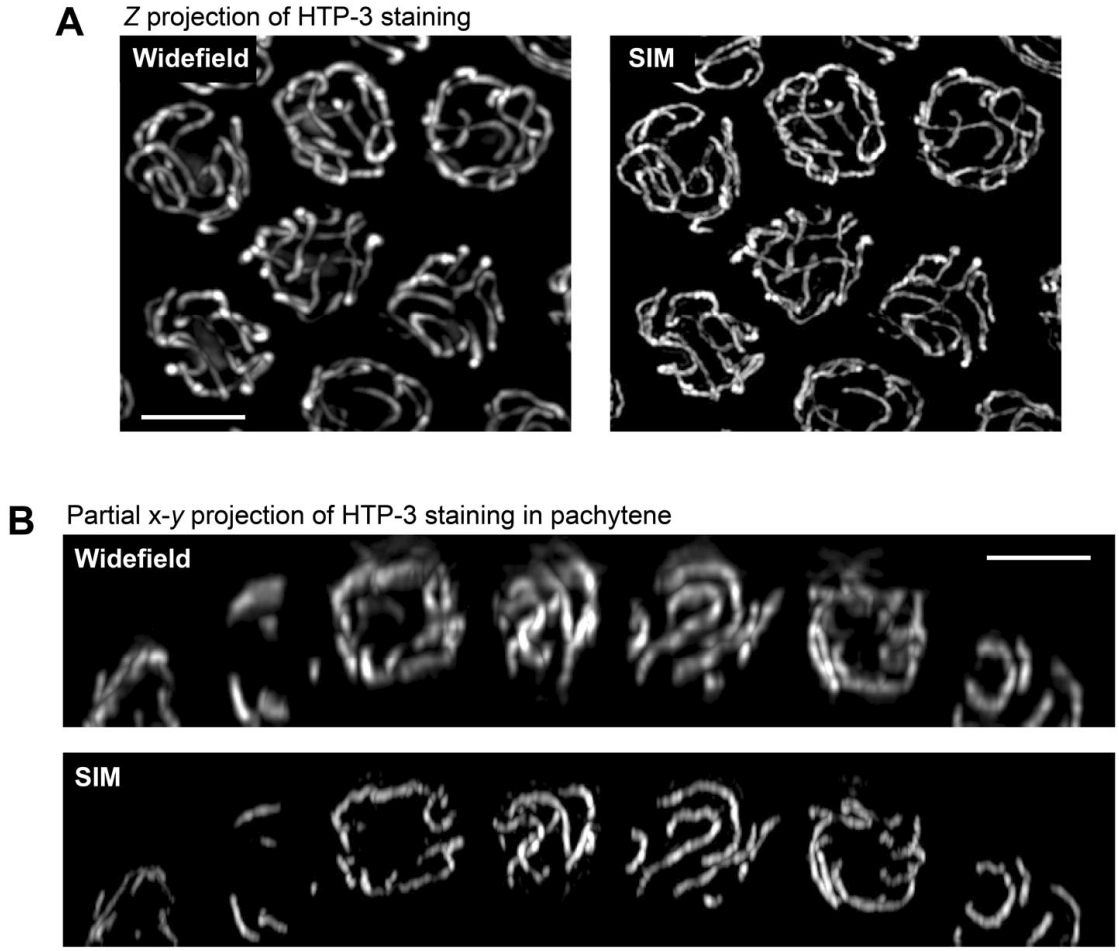


Figure 2.6 SIM imaging of meiotic chromosome axes
(A) A *z*-projection of the same field of view of HTP-3-stained pachytene nuclei imaged using widefield deconvolution microscopy (left) and SIM (right). Scale bar, 3μm. (B) A partial *x-y* projection of the same field of view; the enhanced axial resolution and contrast is apparent in the significantly narrower and sharper axis staining in the SIM image. Scale bar, 3μm.

METHODS

Sample preparation and microscopy

The analysis described here was applied predominately to three-dimensional structured illumination images of axis components stained by immunofluorescence in dissected and fixed whole-mount gonads. Procedures for sample preparation, immunofluorescence, and structured illumination imaging are described in Chapter 3.

Implementation of image analysis algorithms

All of the algorithms described here were implemented in MATLAB (Mathworks). Because built-in support for manipulation of three-dimensional images is limited in MATLAB, custom functions for reading, writing, filtering, resizing, and displaying three-dimensional images were written. In most cases, these were implemented as extensions of the built-in two-dimensional versions. Three dimensional images were stored and retrieved as uncompressed multi-page TIFF files.

The watershed algorithm used for chromosome segmentation was the built-in dimensionality-independent implementation provided by MATLAB. Custom functions for labeling surfaces and volumes in three-dimensional binary images were written in C and compiled for MATLAB. The skeletonization algorithm used in the chromosome tracing analysis was an implementation of a published algorithm (Lee et al., 1994) written in C and compiled for use in MATLAB. Custom algorithms for manipulating and simplifying skeletonized volumes were written to eliminate spurs and topological complexity like loops. The open-ended active contour model was adapted from an open-source implementation (Kroon, 2011). Chromosome straightening and focus localization algorithms used the built-in geometric transformation and nonlinear least-squares fitting algorithms, respectively, provided by MATLAB.

Chapter 3 Characterization of meiotic chromosome organization and the distribution of DSBs and crossovers

Introduction

Crossover formation is the hallmark event of meiosis and is both required for its successful execution and underlie its evolutionary benefit. Crossovers are also, however, subject to a remarkable tension during meiosis, for the double strand breaks required to initiate crossover formation also threaten the integrity of the genome. In consequence, crossover formation is subject to regulation on scales ranging from the nucleotide level to the entire genome. Locally, for example, both DSBs and crossovers preferentially occur at hotspots whose positions are determined by a combination of local chromatin features, histone modifications, and, in most mammals, primary sequence motifs (reviewed in de Massy, 2013). On larger scales, meanwhile, crossover interference inhibits the clustering of crossovers over lengths that can span millions of base pairs, implying that local biochemical information is propagated in *cis* across entire chromosomes (reviewed in Hillers, 2004).

These many scales of crossover regulation are mirrored by both local and global regulation of chromosome organization during meiosis. Upon meiotic entry, each homolog becomes organized into a linear array of loops tethered at intervals to a protein backbone called the chromosome axis (Blat et al., 2002; Kleckner, 2006). In budding yeast, loci at or near DSBs are among those that become tethered to the axis, where axis components play local roles in directing and regulating recombination (Panizza et al., 2011; Storlazzi et al., 2010). On a larger scale, the chromosome axis mediates genome-wide surveillance of recombination defects and is required for the assembly of a structure called the synaptonemal complex (SC) between the axes of paired homologs (reviewed in Page and Hawley, 2004). The SC is required for the formation of crossovers, likely helps prevent entanglements between homolog pairs, and may play a role in implementing crossover interference in some organisms (Hayashi et al., 2010; Libuda et al., 2013).

Our molecular understanding of recombination and its relationship to chromosome organization has emerged principally from population-based biochemical methods. Recently, sequencing-based assays have extended these methods to yield high-resolution, genome-wide maps of meiotic DSBs, crossovers, and sites of chromosome-axis associations (reviewed in de Massy, 2013). Meanwhile, our understanding of large-scale chromosome organization, the SC, and dynamic chromosome-wide behaviors has relied on low-throughput immunofluorescence or live imaging of meiotic chromosomes. Although much has been learned from this approach, it is limited by the laboriousness and difficulty of extracting quantitative information from complex images. To understand the relationship between large-scale chromosome organization and the chromosome-wide regulation of recombination during meiosis, quantitative methods are required that combine the high throughput of population-based biochemical assays with the temporal and contextual information provided by cytological methods.

Several lines of evidence hint at the importance of developing such methods. In *C. elegans*, both chromosome axis length and the distribution of crossovers are altered in condensin mutants (Mets and Meyer, 2009) and when the SC is perturbed by partially

depleting one of its components (Hayashi et al., 2010; Libuda et al., 2013). In budding yeast, shorter chromosomes receive more DSBs (Pan et al., 2011) and crossovers (Kaback et al., 1992), while in humans and mice, a direct correlation between chromosome length and crossover number has been observed (Gruhn et al., 2013; Kauppi et al., 2011; Kleckner et al., 2003). These observations all point to a relationship between a large-scale emergent property of chromosome organization—axis contour length—with the distribution of recombination events along the chromosome. Cytological measurements of axis length have also implied that contour-length distance along the chromosome axis, rather than physical distance (measured in in base pairs), is the metric of crossover interference (Kleckner et al., 2003; Zhang et al., 2014). This suggests that the medium of the interference 'signal' is not the chromosome itself but instead some feature of its physical organization—which is observable only by cytological methods.

Motivated by these observations, we applied our high-throughput image analysis pipeline, described in the previous chapter, to quantify both chromosome organization and the distribution of DSBs and crossovers cytologically in *C. elegans*. This new approach bridges the gap between low-throughput cytological observations and high-resolution, population-averaged measurements of DSB distributions and enables us to monitor temporal changes in the distribution of DSBs on a chromosome-wide basis and to correlate that distribution with features of meiotic chromosome organization. We find that the distribution of DSBs is dynamic during prophase and shifts in mid-pachytene from a distribution that mirrors the distribution of crossovers to one that is more uniform. This shift correlates with isotropic, recombination-independent elongation of chromosomes along the axis and is insensitive to defects in recombination and variation in chromosome axis length and in the number of DSBs.

RESULTS

Chromosome axes elongate during pachytene

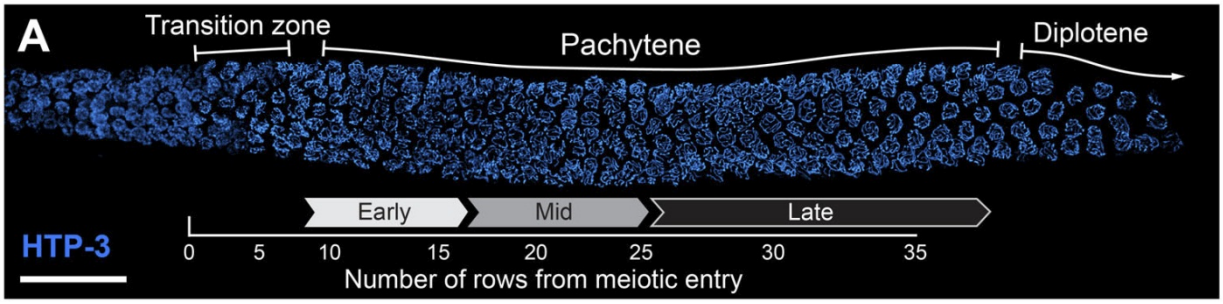
In *C. elegans*, the earliest stages of meiosis define a region of the gonad called the transition zone. This region corresponds to the leptotene and zygotene stages or meiotic prophase, during which the axis assembles and homologs pair and then synapse. Completion of synapsis defines the beginning of the pachytene stage, which in *C. elegans* occupies much of the distal region of the gonad. Nuclei normally remain in pachytene until they reach the "bend" or "loop" of the gonad, where spatially regulated signals trigger exit from pachytene, chromosome condensation, and eventually segregation. Pachytene exit is also marked by disassembly of the SC as the chromosomes reorganize in preparation for the first meiotic division (Figure 3.1A).

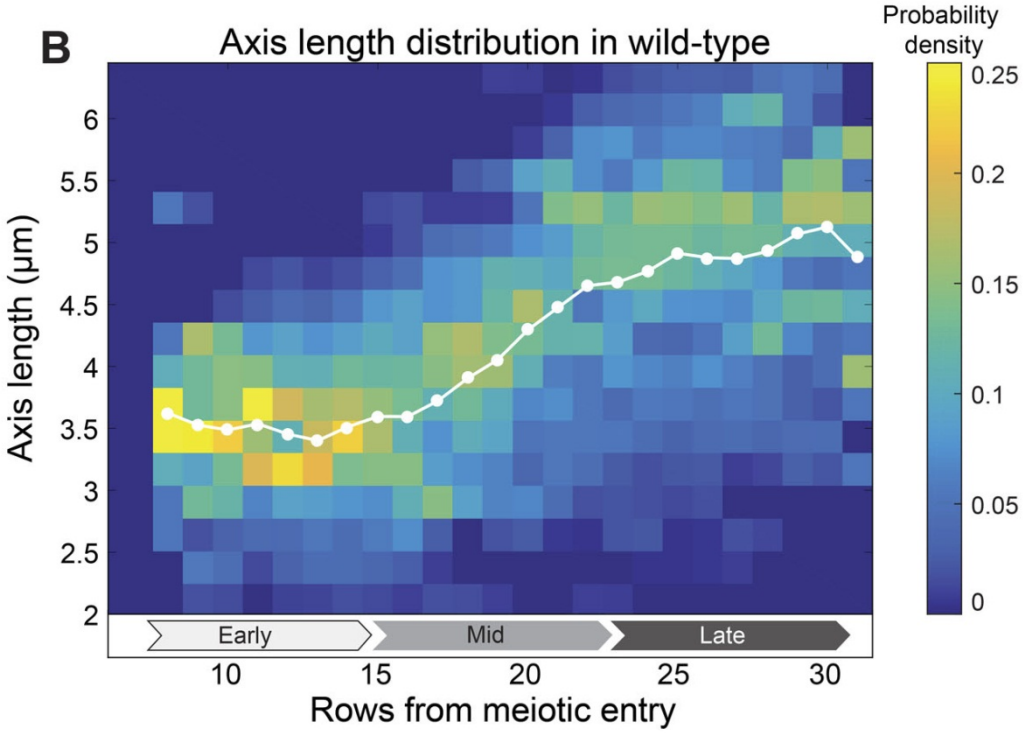
We applied our analysis pipeline to investigate the progression of wild-type nuclei through the pachytene stage. We used immunofluorescence and structured illumination microscopy to image the axis component HTP-3, which localizes to the chromosome axis upon meiotic entry (Goodyer et al., 2008; Martinez-Perez et al., 2008). To detect changes in chromosome organization during pachytene, we also measured the position of each analyzed nucleus within the gonad by counting the number of rows between it and the start of the transition zone (Figures 2.5 and 3.1A). Using the computational chromosome traces to measure total chromosome axis length, we plotted the

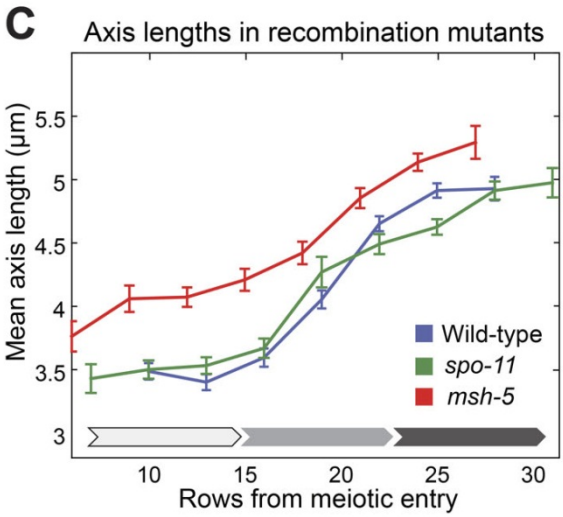
distribution of axis lengths at each row in pachytene to generate a two-dimensional histogram (Figure 3.1B). We observed a significant increase in axis length during pachytene. In early pachytene (rows 10-16), mean axis length was 3.41μm, while in late pachytene (rows 25-30), mean axis length was 4.77μm—an increase of approximately 40%.

We wondered whether the elongation of chromosome axes was a consequence of double strand break or crossover formation, both of which occur during early and mid-pachytene. We first measured axis lengths in *spo-11* mutants, which lack the enzyme responsible for generating meiotic DSBs (Dernburg et al., 1998; Keeney et al., 1997). We detected elongation of the axis that closely corresponded to the elongation we observed in wild-type hermaphrodites (Figure 3.1E), indicating that either DSBs or meiotic recombination is not required for axis elongation. We also measured axis length in a *msh-5* mutant, in which DSBs form but cannot be repaired to form crossovers (Kelly et al., 2000). We observed axis elongation in this mutant, indicating that unrepaired recombination intermediates do not prevent axis elongation. The mean length of early pachytene axes, however, was greater in this mutant than in wild-type (Figure 3.1E).

The axis elongation we observe could occur in several ways. It could occur gradually as nuclei progress through mid-pachytene, or it could occur abruptly and rapidly within each nucleus at some particular point in mid-pachytene. To distinguish between these possibilities, we simulated a spectrum of scenarios in which a portion of the observed increase in axis length occurs abruptly but stochastically while the remaining increase occurs gradually. A quantitative signature of abrupt elongation is a transient spike in the variance in axis length when elongation occurs (Figure 3.1D). We did not detect any such spike in axis length variance in wild-type, *spo-11*, or *msh-5*, suggesting that axis elongation is not, predominately, abrupt. However, simulations of intermediate scenarios revealed that the magnitude of the predicted spike decreases rapidly below the detectability threshold set by the error in the measured variances as the abrupt portion of elongation is reduced. We cannot, therefore, eliminate scenarios in which a portion of the elongation occurs abruptly while the remainder occurs gradually.


A
Transition zone
Pachytene
Diplotene
Early
Mid
Late
HTP-3
0
5
10
15
20
25
30
35
Number of rows from meiotic entry


B
Axis length distribution in wild-type
Probability density
0.25
0.2
0.15
0.1
0.05
0
Axis length (μm)
6
5.5
5
4.5
4
3.5
3
2.5
2
Early
Mid
Late
10
15
20
25
30
Rows from meiotic entry


C
Axis lengths in recombination mutants
Mean axis length (μm)
5.5
5
4.5
4
3.5
3
Wild-type
spo-11
msh-5
10
15
20
25
30
Rows from meiotic entry

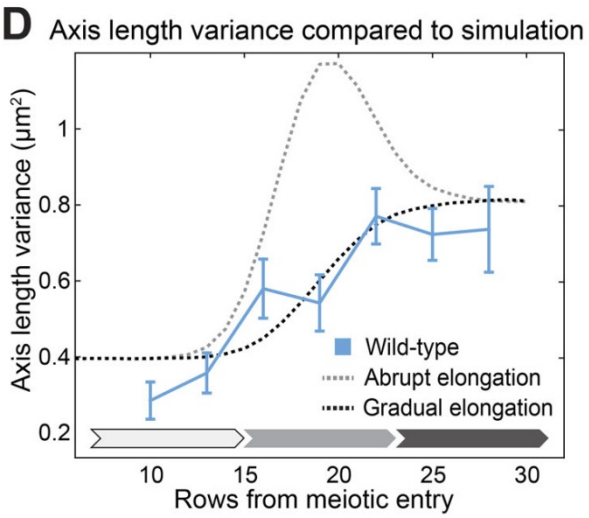
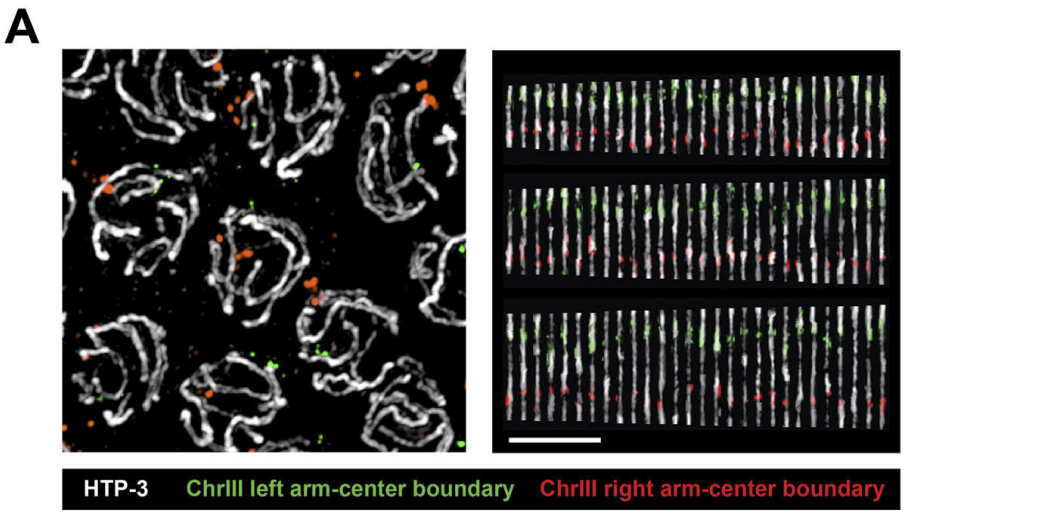
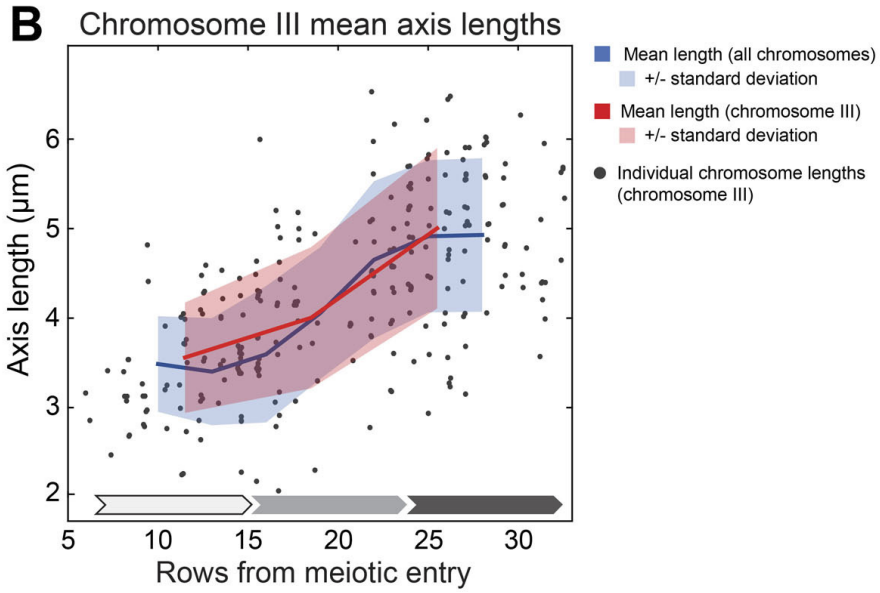

D
Axis length variance compared to simulation
Axis length variance (μm²)
1
0.8
0.6
0.4
0.2
Wild-type
Abrupt elongation
Gradual elongation
10
15
20
25
30
Rows from meiotic entry

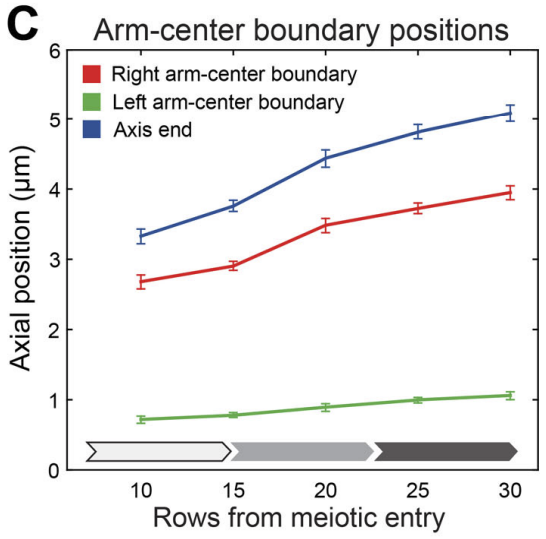
Figure 3.1 Chromosome axes elongate during pachytene
(A) Overview of meiotic prophase, showing definitions of early, mid, and late pachytene. The row numbers on the horizontal axis are specific to the image shown; variation in the absolute spacing between rows exists within and between gonads. Scale bar, 20μm. (B) Axis lengths of all chromosomes plotted as a two-dimensional histogram. Mean axis length is overlaid in white. (C) Mean axis lengths over pachytene in wild-type, *spo-11*, and *msh-5*. Axis length increases by late pachytene in both mutants. Errors bars, standard error of the mean. (D) Axis lengths were simulated for two simple models of axis elongation: one in which elongation occurs gradually, and the other in which elongation occurs instantaneously but at a stochastic time in mid-pachytene. The model parameters were adjusted so that the mean axis length matched the experimental results in (B). The measured standard deviation of axis lengths argues against abrupt axis elongation, which should generate a spike in standard deviation during the window when axes abruptly elongate. Error bars, standard error of the variance.

Axis length is not dictated by physical chromosome length

A prominent feature of the axis length distribution we observed is wide variation in axis lengths. The magnitude of this variation was not constant but instead increased during pachytene in approximate proportion to the increase in mean axis length; the standard deviation of axis lengths corresponded to between 18% and 22% of the mean axis length throughout pachytene. This variation could reflect the underlying variation in the physical length of different chromosomes, or it could reflect chromosome-to-chromosome variability. To determine the variation in the length of the same chromosome in different nuclei, we combined FISH with immunofluorescence to label individual chromosomes (Figure 3.2A). We initially chose to label chromosome III, because of its especially symmetric domain organization (see below), but also confirmed our results using lacI::GFP to label an array of *lac* operator repeats integrated into chromosome V (Gonzalez-Serricchio and Sternberg, 2006) (Figure 3.3). Strikingly, the length of the chromosome III axis varied as widely as the lengths of all six chromosomes collectively (Figure 3.2B). In both early and late pachytene, minimum and maximum observed axis lengths differed by nearly a factor of two (Figure 3.2B). This observation implies that variation in chromosome axis length is not a consequence of the differences in physical length between different chromosomes and must occur stochastically, either between nuclei or chromosomes themselves. In individual nuclei, the length of the shortest and longest axes are well-correlated in both early and late-pachytene nuclei, suggesting that much of the variation occurs between, rather than within, nuclei (Figure 3.4B).


A
HTP-3
ChrIII left arm-center boundary
ChrIII right arm-center boundary


B
Chromosome III mean axis lengths
Mean length (all chromosomes)
+/- standard deviation
Mean length (chromosome III)
+/- standard deviation
Individual chromosome lengths (chromosome III)
Axis length (µm)
Rows from meiotic entry


C
Arm-center boundary positions
Right arm-center boundary
Left arm-center boundary
Axis end
Axial position (µm)
Rows from meiotic entry

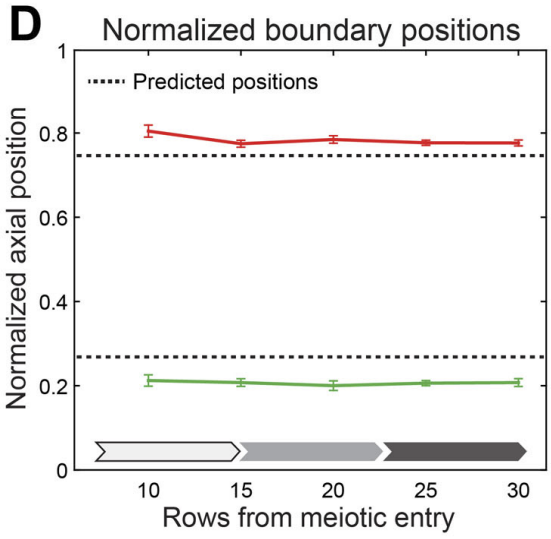

D
Normalized boundary positions
Predicted positions
Normalized axial position
Rows from meiotic entry

Figure 3.2 Chromosome III axis length and compaction during pachytene
(A) FISH against loci at the border between the arm and center regions of chromosome III combined with immunofluorescence against the axial element HTP-3. Chromosomes are segmented and traced as shown in Figure 1, and the position of the centroid of the FISH signals along the straightened axes determined to measure the axial length of each region. Scale bars, 3μm. (B) The mean and standard deviation of chromosome III axis lengths (red) overlaid on the chromosome-averaged data shown in Figure 2 (blue) and on a scatter plot of individual chromosome III axis lengths (black circles). The variation in chromosome III axis lengths is comparable to the variation in the chromosome-averaged data. (C) Axial position of the FISH signals, relative to the left end of the chromosome axis, during meiosis. Error bars, standard error of the mean. (D) Axial positions of the two FISH signals normalized by total axis length. Despite variation in axis length and elongation of the axis during pachytene, the relative positions of the arm-center boundaries remain constant. Error bars, standard error of the mean.

Chromosome compaction is not dynamic during pachytene

The distal regions, or 'arms,' of each chromosome in *C. elegans* differ in several ways from the central regions. The arms are have more repetitive sequences, are enriched for heterochromatic histone modifications (*C. elegans* Sequencing Consortium, 1998; Liu et al., 2011) and, most prominently, receive significantly more crossovers than the center regions (Barnes et al., 1995; Brenner, 1974; Rockman and Kruglyak, 2009). We hypothesized that the arm and center regions might be differentially compacted along the chromosome axis and, if so, that the loss of this differential compaction during pachytene would drive the axis elongation we observed. To measure the compaction of chromatin in the arm and center regions, we developed FISH probes using the OligoPaints method (Beliveau et al., 2012) to label the boundaries between these regions on chromosome III. Using a three-dimensional focus-finding algorithm, we determined the positions of the two FISH foci along the segmented and traced chromosomes (Figure 3.2A).

The mean length of the chromosomes increased during pachytene by approximately 40%, from about 3.5μm to 5μm, consistent with our chromosome-averaged results (Figure 3.2B). The two arm regions also increased in length, and in nearly exact proportion to the overall increase in axis length. Each arm region is approximately 0.7μm in length in early pachytene and 1μm in length by late pachytene—an increase of 40% (Figure 3.2C). This result indicates that the chromosome axis elongation we observe during pachytene occurs by homogeneous expansion of the chromosome, rather than by differential expansion of the arm or center regions. Notably, however, the arm regions are more compact than the center region, together occupying 43% of the chromosome axis despite spanning 52% of the physical length of the chromosome (Figure 3.2D). This disparity implies that the axial density of chromatin is about 40% greater along the arms than in the center. In early pachytene, the mean arm lengths that we observe imply that the density of chromatin is 4.7 mbp/μm in the arms and 3.3 mbp/μm in the center region.

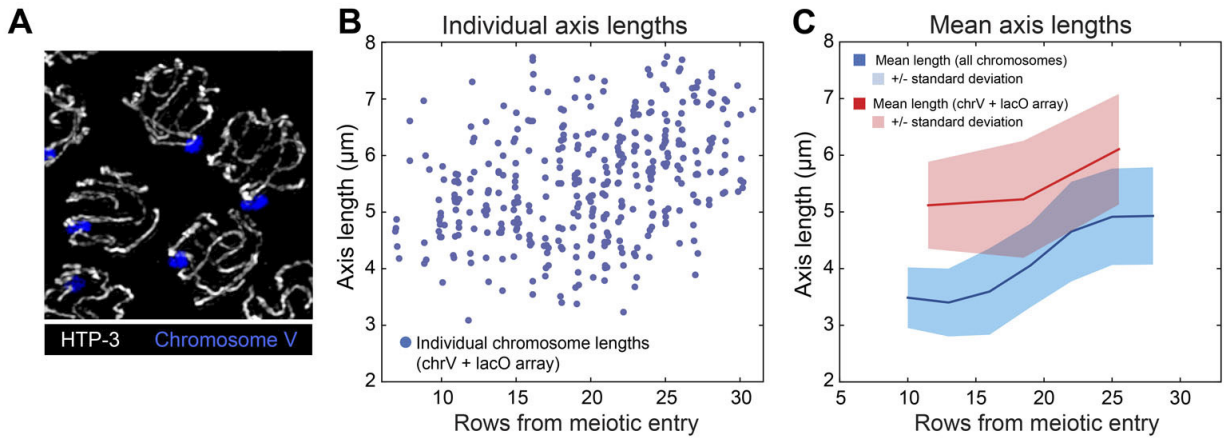


Figure 3.3 Chromosome V axis length variation
(A) Chromosome labeling using lacI::GFP 'stain' an array of *lac* operator (*lacO*) repeats integrated into the left end of chromosome V. (B) Scatter plot of chromosome V axis lengths during pachytene. (C) Mean and standard deviation of chromosome V axis lengths plotted over the chromosome-averaged mean length from Figure 2. The variation in axis length is comparable to that observed in the all-chromosome wild-type data.

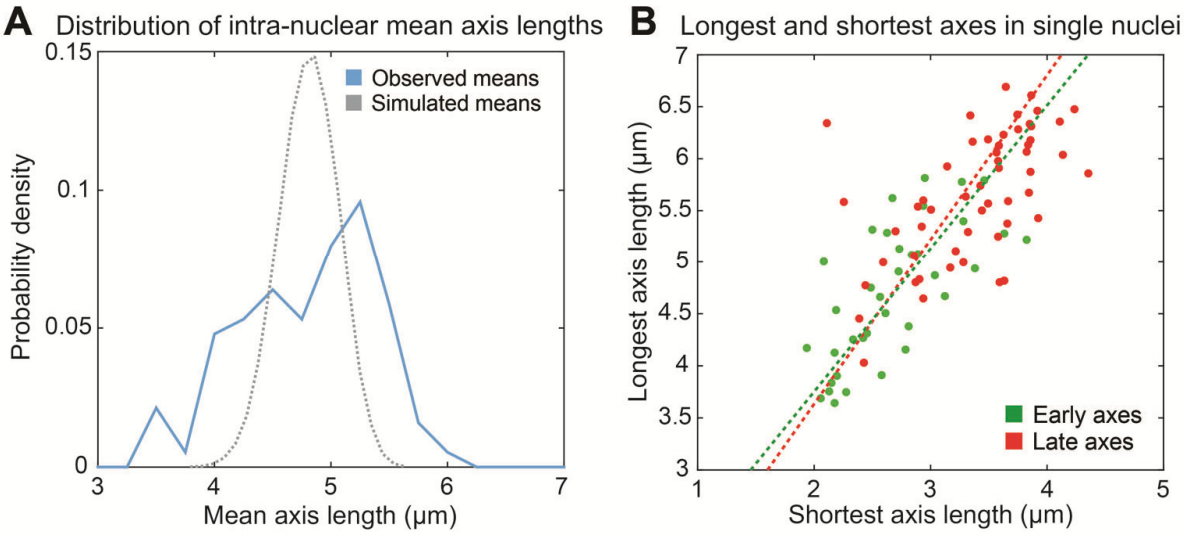


Figure 3.4 Axis lengths are correlated within single nuclei
(A) The distribution of the mean length of axes in single nuclei is wider than the distribution of the means of randomly selected sets of six axes (i.e., 'simulated' nuclei), indicating that some of the variation in axis length occurs between nuclei and not between chromosomes within single nuclei. (B) The lengths of the shortest and longest axes in single nuclei are well-correlated, again suggesting that axis length variation occurs at the nuclear, rather than chromosomal, level.

The distribution of DSBs changes during pachytene in coordination with axis elongation

Population-based measurements of DSB distributions in several organisms have led to the general conclusion that DSB distributions mirror crossover distributions (reviewed in de Massy, 2013). The results of ChIP-seq experiments (Ho et al., 2014) and measurements on the X chromosome (Mets and Meyer, 2009) suggest that this conclusion also holds true in *C. elegans*. To confirm these results, and to resolve the dynamics of the DSB distribution during pachytene, we analyzed images of meiotic nuclei co-stained for RAD-51 and the axis protein HTP-3. RAD-51 is the sole recA homolog in *C. elegans* and is required to mediate strand invasion during meiotic DSB repair (Alpi et al., 2003; Colaiácovo et al., 2003). It localizes to chromatin-associated foci in early and mid pachytene nuclei that likely correspond to single DSBs (Figure 3.5A-B). We coupled our chromosome segmentation and tracing pipeline with a focus-finding algorithm to locate RAD-51 foci and associate each focus with its nearest chromosome in order to generate a distribution of foci along the synapsed axes of each homolog pair. Separately, we also measured the distribution of crossovers using a strain expressing GFP::COSA-1, a robust marker for mature crossovers that appears in late pachytene (Figure 3.5B) (Yokoo et al., 2012).

When we measured the distribution of GFP::COSA-1 foci, we observed that most foci appeared on the chromosome arms (Figure 3.5C). The enrichment of foci on the arms closely corresponded to that predicted from the genetic map, as expected given the modest variation in chromatin compaction that we observed using FISH. When we measured the distribution of RAD-51 foci, we observed modest arm enrichment (Figure 3.5C). The enrichment became more dramatic when we examined only foci from early pachytene, and was mostly lost when we examined only foci from late pachytene (Figure 3.5D). To quantify this enrichment, we calculated the ratio between the density of foci on the arms and in the center. In early pachytene, RAD-51 foci are approximately twice as likely to appear on the arms as in the center, but by mid-pachytene, they are only about 20% more likely to do so (Figure 3.5E).

This loss of arm-enriched RAD-51 foci occurred concomitantly with axis elongation (Figure 3.5E). Because axes elongate even in recombination mutants, the RAD-51 distribution could shift in response to axis elongation, or these two phenomena could be independent consequences of meiotic progression. To determine whether axis length per se correlated with the distribution of RAD-51 foci, we took advantage of the wide variation in axis lengths and plotted the distribution of RAD-51 foci along the longest and shortest axis length quartiles in early pachytene, prior to the increase in mean axis length and loss of arm-enriched RAD-51 foci. We found no statistically significant difference between the distributions of RAD-51 foci on short and long axes in either early or late pachytene (Figure 3.6A), indicating that axis length alone does bias RAD-51 foci to appear on the chromosome arms.

A correlation between axis length and the number of crossovers has been observed in several organisms, even when chromosome physical length is unchanged (Kleckner et al., 2003; Libuda et al., 2013; Lynn, 2002). Although we cannot directly measure the number of DSBs per chromosome, we used the frequency with which we observed two RAD-51 foci on one chromosome as a proxy for DSB number. We found that the frequency of axes with two RAD-51 foci remained constant during pachytene,

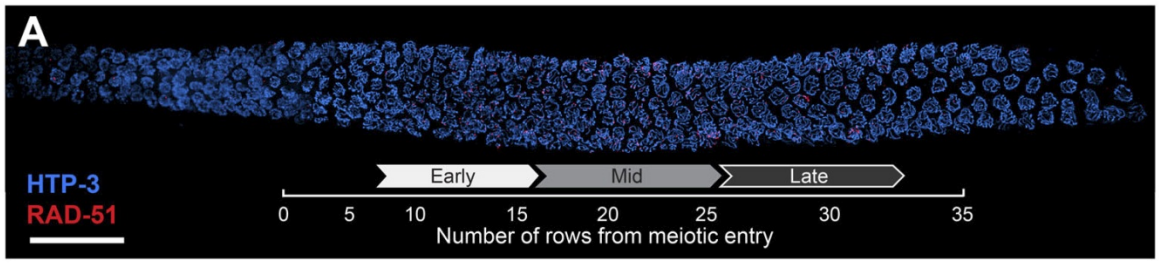
despite axis length elongation that occurs between early and late pachytene (Figure 3.6B). We also did not observe any change in the frequency of two RAD-51 foci when we binned chromosomes by length in early and late pachytene, implying that axis length alone does not either promote or inhibit DSB formation.

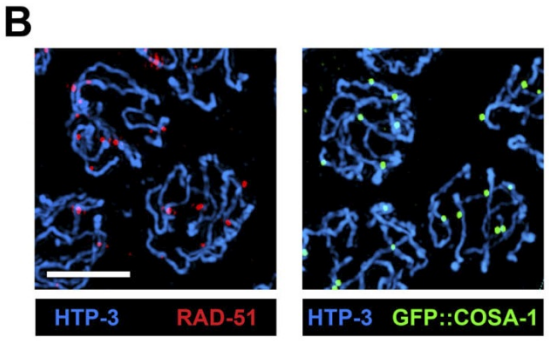
The distributions of RAD-51 foci and axis lengths are unperturbed in *him-8* but coordinately perturbed in *him-5*

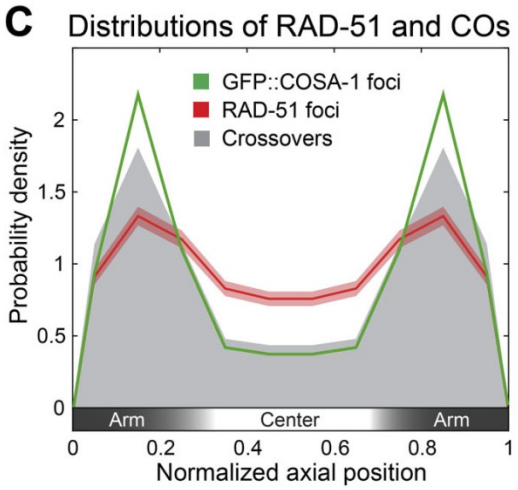
DSB formation in *C. elegans* is governed, in part, by a checkpoint-like response that prolongs the period of time during which breaks are made when defects in crossover formation occur (Kim et al., 2015; Stamper et al., 2013). This response appears to be genome-wide; even when only one chromosome cannot form a crossover, markers of recombination intermediates and a DSB-permissive state persist on all chromosomes (Carlton et al., 2006; Rosu et al., 2013; Stamper et al., 2013). Interestingly, in these situations, the distribution of crossovers is also perturbed on all chromosomes (Carlton et al., 2006, Kotwaliewale and Dernburg, unpublished), and an analogous phenomenon appears to affect the DSB distribution in yeast (Thacker et al., 2014). We wondered whether the loss of arm-enriched RAD-51 foci that we observed in wild-type occurs in response to the satisfaction of this checkpoint and whether, in consequence, defects in crossover formation would extend the zone of arm-enriched RAD-51 foci.

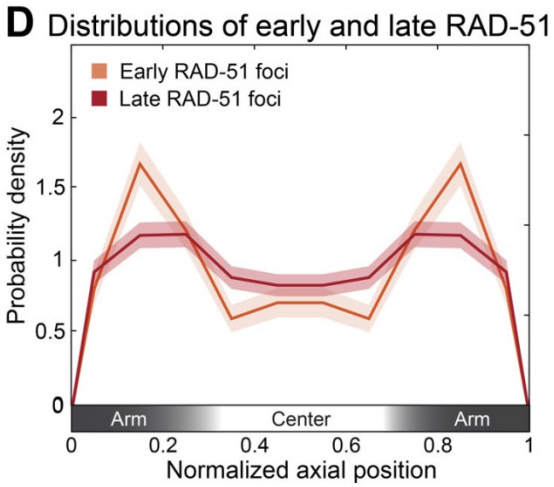
We measured the distribution of RAD-51 foci in *him-8(me44)*, which specifically disrupts pairing and, consequently, crossover formation on the X chromosome (Phillips et al., 2005). We found that early RAD-51 foci were approximately as arm-enriched as in wild-type, and that the distribution of foci shifted at approximately the same position in pachytene as in wild-type (Figure 3.5F). This result indicates that crossover defects, despite prolonging the DSB-permissive zone, do not delay the loss of arm-enriched RAD-51 foci. The wild-type-like arm enrichment of early RAD-51 foci we observed in *him-8* is consistent with the genetic map in this mutant, which, though altered on each chromosome, resembles the wild-type genetic map after averaging over all five autosomes (Kotwaliwale and Dernburg, unpublished).

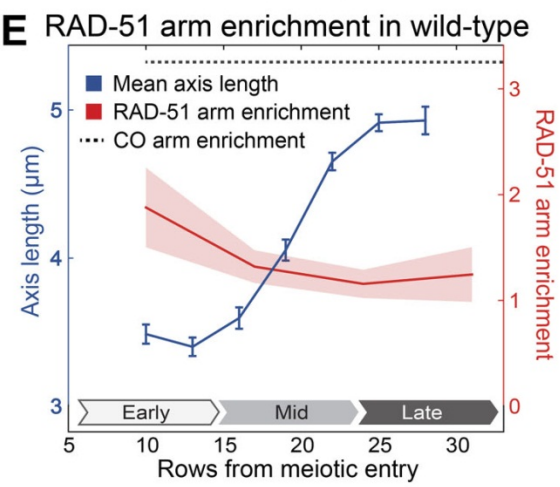
To determine whether arm-enriched RAD-51 foci are lost when the arm enrichment of crossovers is lost genome-wide, we measured axis length and DSB distributions in a *him-5* mutant. In this mutant, pairing and synapsis are unimpaired, but DSBs fail to form specifically on the X chromosome (Meneely et al., 2012). The consequent failure to form a crossover on the X chromosome triggers the same checkpoint-like response as in *him-8* (Stamper et al., 2013). The crossover map is also perturbed genome-wide; the enrichment of crossovers on the arms is largely lost on every autosome, and this is reflected in the autosome-averaged distribution (Kotwaliwale and Dernburg, unpublished). When we measured the distribution of RAD-51 foci, we observed that early foci were not arm-enriched, mimicking the loss of arm-enriched crossovers in this mutant (Figure 3.5F). At the same time, chromosome axes failed to elongate. This result implies that the arm enrichment of DSBs in wild-type plays a role in imposing the arm enrichment of crossovers, and also suggests a connection between DSB regulation and axis elongation.


A
HTP-3
RAD-51
Early
Mid
Late
0 5 10 15 20 25 30 35
Number of rows from meiotic entry


B
HTP-3 RAD-51
HTP-3 GFP::COSA-1


C
Distributions of RAD-51 and COs
GFP::COSA-1 foci
RAD-51 foci
Crossovers
Probability density
Arm
Center
Arm
Normalized axial position


D
Distributions of early and late RAD-51
Early RAD-51 foci
Late RAD-51 foci
Probability density
Arm
Center
Arm
Normalized axial position


E
RAD-51 arm enrichment in wild-type
Mean axis length
RAD-51 arm enrichment
CO arm enrichment
Axis length (µm)
RAD-51 arm enrichment
Early
Mid
Late
Rows from meiotic entry

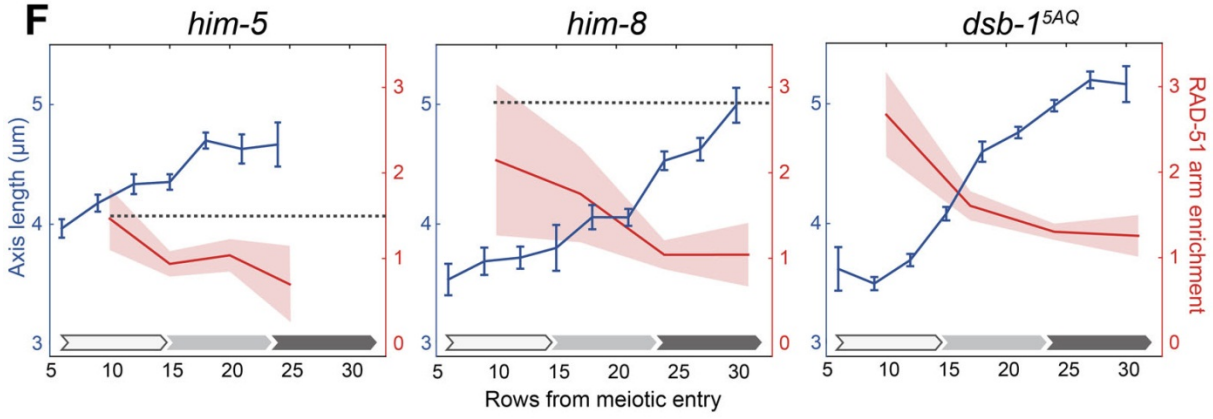

F
him-5
him-8
dsb-1 5AQ
Axis length (µm)
RAD-51 arm enrichment
Rows from meiotic entry

Figure 3.5 RAD-51 foci are arm enriched in early pachytene but uniformly distributed in late pachytene.
(A) Immunofluorescence against RAD-51 (in red) reveals foci in nuclei from a broad region corresponding to early and mid-pachytene. Scale bar, 20μm. (B) RAD-51 localizes to multiple chromosome-associated foci in each nucleus. GFP::COSA-1, a marker of mature crossovers, also localizes to foci, but only appears in late pachytene. Scale bar, 3μm. (C) The distribution of GFP::COSA-1 foci along the chromosome axis, visualized as a one-dimensional histogram of focus positions normalized by total axis length (green line). This distribution mimics the distribution of crossovers predicted from the genetic map (solid gray shading). The distribution of all observed RAD-51 foci (in red) also exhibits arm enrichment, but not as dramatically as GFP::COSA-1 foci. The shading around the RAD-51 distribution corresponds to the estimated standard deviation of histogram bin counts. (D) The distribution of RAD-51 foci appearing in early pachytene (light red) exhibits more dramatic arm enrichment than the distribution of foci appearing in mid-pachytene (dark red). The shading around each distribution again corresponds to the estimated standard deviation of histogram bin counts. (E) Mean axis length (blue curve) overlaid on a measure of RAD-51 arm enrichment—the ratio of the density of RAD-51 foci on the arms and in the center during pachytene (red curve). The error bars indicate the standard error of the mean, while the shaded area surrounding the enrichment values corresponds to the bootstrap-estimated standard deviation. (F) Mean axis length and RAD-51 arm enrichment in *him-5*, *him-8*, and *dsb-1*^{5AQ}. Only in *him-5* is the arm enrichment of early-pachytene RAD-51 foci lost.

The dynamic distribution of DSBs is insensitive to DSB number and is not the product of DSB interference

Multiple regulatory circuits control the timing of DSB formation during meiosis. In mouse, yeast, and worms, one such circuit is a negative feedback loop that, once triggered by the earliest meiotic DSBs, inhibits the formation of additional DSBs (Carballo et al., 2013; Joyce et al., 2011; Lange et al., 2011). In yeast, this feedback has also been implicated in negative interference between DSBs (Garcia et al., 2015). We wondered whether the shift in the distribution of RAD-51 foci we observed was a consequence of this inhibitory feedback following the appearance of the first DSBs in early pachytene. In *C. elegans*, this feedback requires, at least in part, phosphorylation of the nematode- and meiosis-specific gene *dsb-1*. A non-phosphorylatable allele of this gene, *dsb-1*^{5AQ}, has no meiotic defects except for an elevated number of DSBs (Stamper and Dernburg, unpublished). We measured the distribution of RAD-51 foci in this mutant and found that it closely resembles the wild-type distribution, except that, surprisingly, the early RAD-51 foci are even more dramatically arm-enriched than in wild-type (Figure 3.5F). This result indicates that the shift in distribution of RAD-51 foci occurs independently of DSB-1-mediated negative feedback, and also that the dynamics of the DSB distribution are not perturbed by an increase in DSB number.

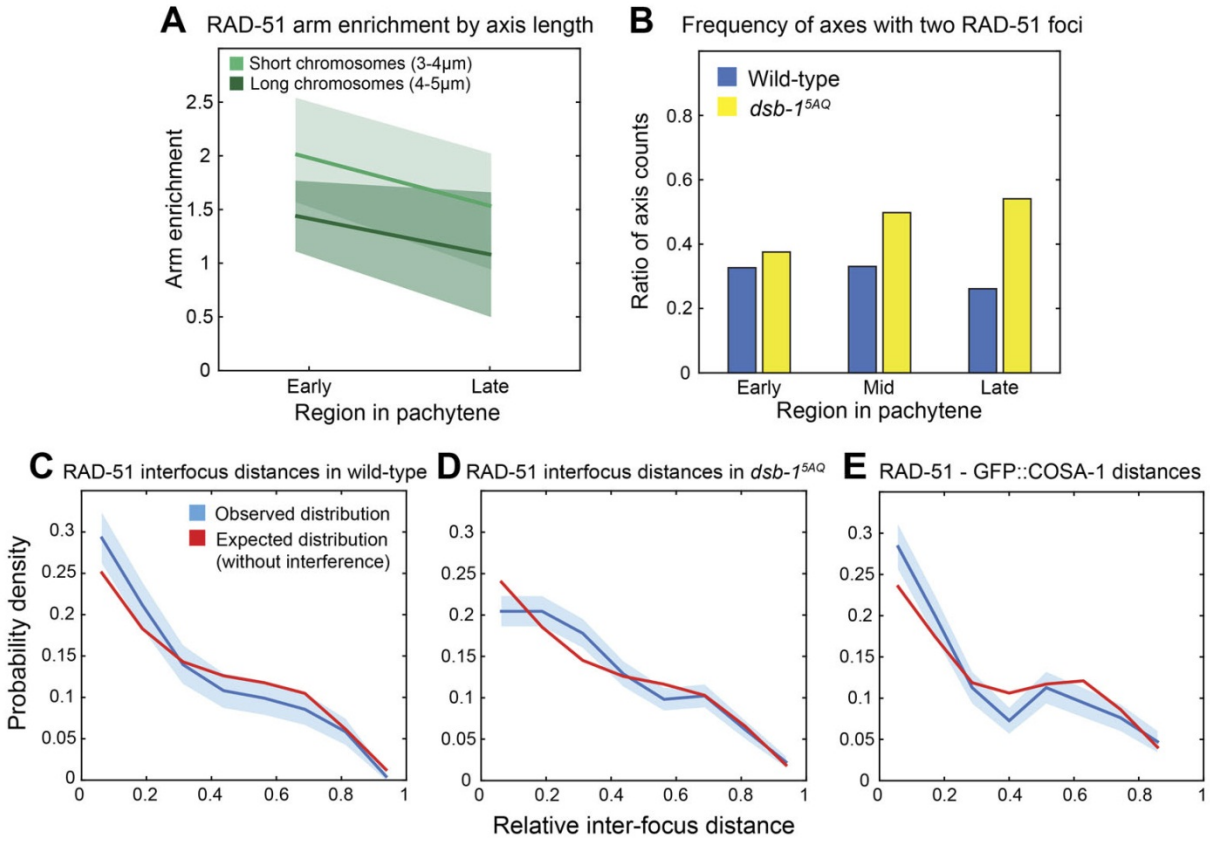


Figure 3.6 Axis length does not predict RAD-51 distribution, and RAD-51 foci do not interfere
(A) The arm enrichment of RAD-51 is lost on both long and short chromosomes in late pachytene, indicating that length per se does not dictate RAD-51 arm enrichment. (B) The frequency with which two RAD-51 foci are observed on one chromosome, relative to the number of chromosomes observed with at least one focus, does not change during pachytene. (C) and (D) The distribution of distances between RAD-51 foci on chromosomes with two foci in wild-type and *dsb-1*^{5AQ}. These distributions closely match the distributions predicted by assuming no interference between foci. (E) The distribution of distances between RAD-51 foci and GFP::COSA-1 foci does not differ significantly from the distribution predicted by assuming that the two species of foci do not interact.

We also measured interference between RAD-51 foci by examining only chromosomes associated with two foci and plotting the distribution of distances between them. We compared this distribution to the distribution of distances between randomly selected pairs of foci; this distribution approximates the expected distribution of inter-focus distances in the absence of interference. We did not observe a significant difference between the two distributions in either wild-type or *dsb-1*^{5AQ} (Figure 3.6C and 3.6D). This result indicates that RAD-51 foci do not interfere with one another and are instead positioned independently of one another.

Chromosome axes are not preferentially curved near DSBs or crossovers

How chromosome organization responds to crossover formation is not well understood. In *C. elegans*, chromosome axes likely elongate locally at crossover sites (Libuda et al., 2013), and crossover formation also triggers asymmetric remodeling of the 'long' and 'short' crossover-demarcated arms of the chromosome axis (Martinez-Perez et al., 2008). A prominent model for crossover interference, the 'mechanical stress' model, also suggests that chromosome organization changes locally near either crossovers or an upstream recombination intermediate (Kleckner et al., 2004). Prompted by these observations, we wondered whether the conformation of the chromosome axis depended upon crossover position. We used our chromosome traces to calculate local curvature (Figure 3.7A), divided each trace into regions near and far from either RAD-51 foci or COSA-1::GFP foci, and observed the distribution of local curvature in the two regions. We did not observe any shift in the curvature distribution near early or late RAD-51 foci (Figure 3.7D-E) or near COSA-1::GFP foci (Figure 3.7C), indicating that the conformation of synapsed axes, at least at the resolution of our chromosome traces, is uncorrelated with DSB or crossover position.

DISCUSSION

Implications of axis length variation

Variation in the axis length of synapsed chromosomes has not previously been measured with the robust statistics that we report here. Measurements of total SC length in humans and mice have hinted at variation in chromosome length (Kleckner et al., 2003; Zickler and Kleckner, 1999). However, these studies did not label individual chromosomes; other studies have measured individual axis lengths, but only either in unstaged nuclei or in nuclei at particular substages of pachytene, and only for the purpose of determining average lengths (Libuda et al., 2013; Mets and Meyer, 2009; Novak et al., 2008). Our observation that the axis length of a single chromosome can vary by a factor of two between nuclei at the same substage of pachytene suggests that meiotic chromosome organization is subject to an unappreciated level of stochasticity.

It is widely accepted that meiotic chromosomes are organized into arrays of chromatin loops that are 'tethered' at particular loci to the axis. Chromosome axis length is a product of both the genomic locations of these tethering sites and the spacing of the tethers along the chromosome axis; variation in axis length must, therefore, require that one of these parameters vary coordinately. Measurements from many different species suggest that, despite vast differences in genome size, the density of loops along the axis is constant within species and varies only modestly—from 10 to 30 loops per micron of axis length—between species (Kleckner, 2006). Consistent with this observation, chromosome axes in mouse cohesion mutants are longer, and loop sizes proportionately shorter, than in wild-type (Novak et al., 2008), and in human spermatocytes total axis length is greater, and loop size smaller, than in oocytes (Tease and Hultén, 2004). These observations imply that the two-fold variation in axis length that we observe most likely occurs by the stochastic selection of loop tethering sites, resulting in a variable number of loops and coordinately variable axis length.

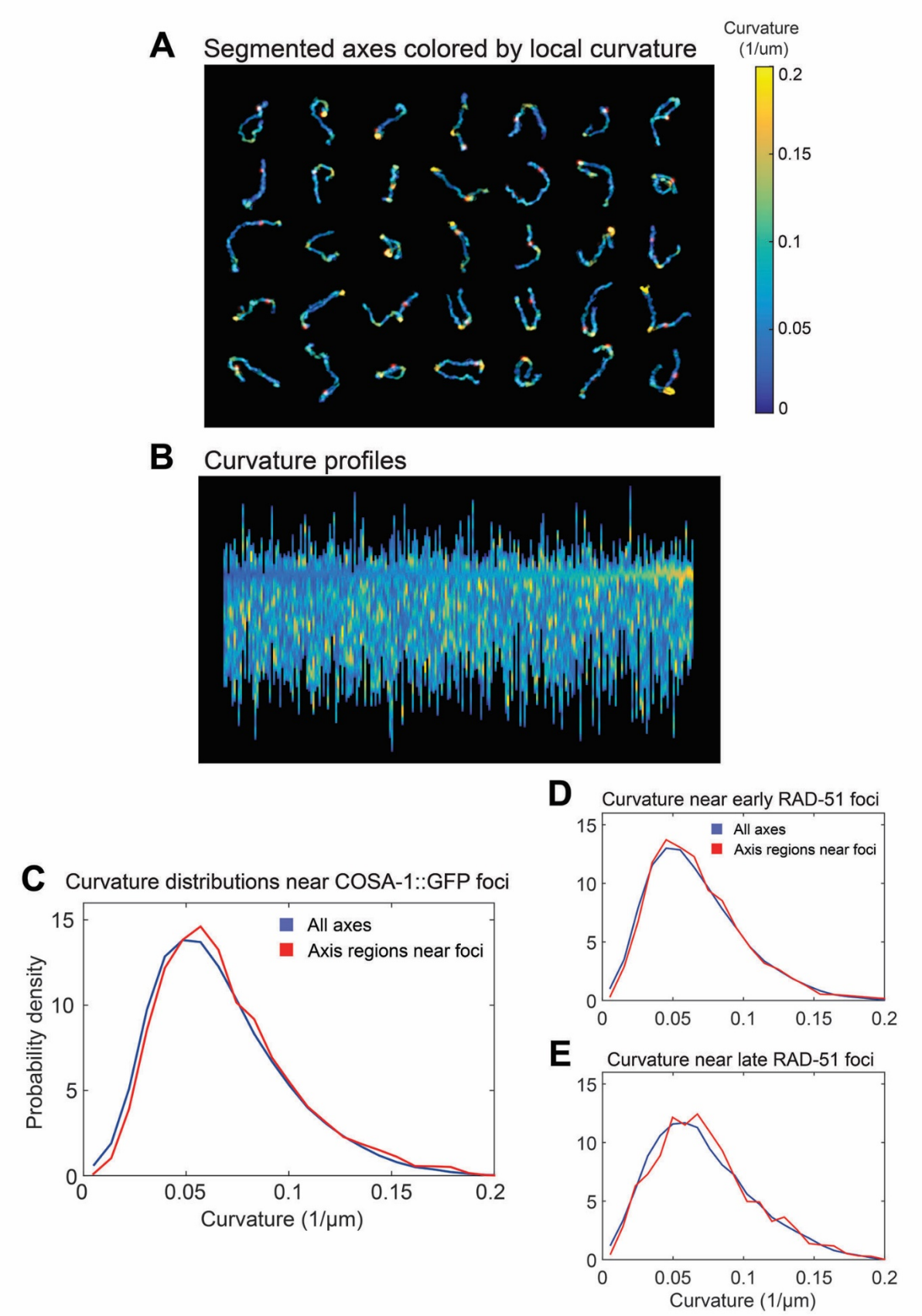

A
Segmented axes colored by local curvature
Curvature (1/um)
0.2
0.15
0.1
0.05
0
B
Curvature profiles
C
Curvature distributions near COSA-1::GFP foci
All axes
Axis regions near foci
Probability density
Curvature (1/μm)
D
Curvature near early RAD-51 foci
All axes
Axis regions near foci
E
Curvature near late RAD-51 foci
Curvature (1/μm)

Figure 3.7 Axis curvature near DSBs and crossovers
(A) Chromosome tracing permits the measurement of axis curvature, illustrated here by coloring the original axis staining according to the local curvature of the corresponding chromosome trace. GFP::COSA-1 foci are overlaid in red. (B) A dataset of synapsed chromosomes, visualized as vertical lines colorized by local curvature, aligned vertically by the position of the GFP::COSA-1 focus associated with each axis and ordered from left to right according to the curvature in the neighborhood of the focus. (C) Distribution of axis curvatures in the neighborhood of GFP::COSA-1 foci (red) and globally along all traces (blue). Analogous distributions for early (D) and late pachytene (E) RAD-51 foci.

Although this simple model does not require any assumptions about how tethering sites are selected, chromatin immunoprecipitation experiments in yeast have revealed that axis components are preferentially associated with short, relatively evenly spaced intervals along each chromosome; these regions have been interpreted to represent the sites at which loops are tethered to the axis (Blat et al., 2002; Glynn et al., 2004). Similar experiments in *C. elegans* have revealed the same pattern of axis associations, albeit with wider variation in the spacing between axis-associated regions (Kotwaliwale and Dernburg, unpublished). Our model for axis length variation implies that only a variable subset of the axis-associated sites identified by these experiments are selected to become tethers along any one chromosome.

Implications of axis length elongation

Robust measurements of chromosome axis length throughout pachytene have not been reported previously, both because of technical limitations and because quantifying progression through pachytene is impossible in many organisms. The elongation of axis length that we observe, however, is consistent with cytological observations in *Sordaria macrospora* and measurements of chromosome volume in maize and other organisms (Kleckner et al., 2004), as well as with analogous measurements of chromosome compaction during mitotic prophase (Liang et al., 2015).

The most obvious implication of the axis elongation we observe is that synapsed chromosomes are not static structures. Furthermore, because the elongation occurs gradually during pachytene and homogenously along chromosomes, it cannot reflect either a discrete or local change in chromosome structure. A recent report that chromosome axes locally elongate in response to crossover formation (Libuda et al., 2013) is not, however, incompatible with our results, because the observed local elongation (several tenths of a micron) is too small to distinguish from the gradual elongation we report here.

Within the context of the loop-axis model of chromosome organization, the axis elongation that we observe during prophase implies that, as with variation in axis length between chromosomes, either the number of loops or the axial spacing between loops must increase as axes elongate. Although loop-axis associations are generally assumed to be static, nothing is known about their temporal stability. In principle, loops could be relatively transient and either respond to, or drive, axis elongation by gradually accumulating during pachytene—provided a mechanism were in place to ensure that the density of loops along the axis remained constant. A more parsimonious explanation of axis elongation is one in which the loops are static and elongation is a consequence of gradual structural changes in either the axis, SC, or chromatin itself that increase the

spacing between adjacent loops. This explanation is consistent with the increase in axis lengths observed in condensin mutants (Mets and Meyer, 2009) and in partial depletion of SC components (Hayashi et al., 2010; Libuda et al., 2013). Provocatively, in vitro studies of condensins have shown that these molecules alone can independently control the width and length of mitotic chromosomes (Shintomi and Hirano, 2011), suggesting that relatively subtle stoichiometric shifts coupled to meiotic progression could be sufficient to drive chromosome axis elongation.

However it occurs, the elongation of synapsed axes has the important implication that the SC is dynamic in at least the sense that it can grow substantially longer without becoming (cytologically) discontiguous during pachytene. This observation is consistent with other evidence of dynamic SC behavior, including that the SC can undergo post-assembly extension into regions of unsynapsed axis (Henzel et al., 2011; MacQueen et al., 2005) and that it can incorporate new subunits after its assembly is (cytologically) complete (Voelkel-Meiman et al., 2012). Recent work suggesting that the SC has liquid-like properties provides an elegant synthesis of these disparate observations (Rog and Dernburg, unpublished) and readily explains how the SC might 'elongate' along with the axis.

A dynamic distribution of DSBs

The measurements of RAD-51 foci that we report here are the first to temporally resolve the distribution of DSBs in any organism. DSB distributions have previously been measured using genome-wide techniques in yeast (reviewed in de Massy, 2013), mice (Smagulova et al., 2011), and *C. elegans* (Ho et al., 2014), as well as cytologically on particular chromosomes (Mets and Meyer, 2009). In all of these cases, despite averaging over many meiotic nuclei, the distribution of DSBs has closely mimicked the distribution of crossovers, leading to the general conclusion that crossover distribution is determined at the time of DSB formation.

Our results are partially in concordance with this conclusion; we observe that the earliest DSBs to appear are, like crossovers in *C. elegans*, most likely to occur on the chromosome arms. The degree of arm enrichment, while significant, is less for DSBs than for crossovers; while about 90% of crossovers occur on chromosome arms, 70% of early RAD-51 foci appear on chromosome arms. More significantly, we observe that DSBs appearing later in prophase are not arm-enriched but instead uniformly distributed along chromosomes—in contrast to the distribution of crossovers and to ChIP-seq measurements of RAD-51 enrichment (Ho et al., 2014).

Several possibilities could explain this discrepancy. RAD-51 oligomerizes along DSB-adjacent single stranded overhangs, forming a nucleoprotein filament that corresponds, cytologically, to a single RAD-51 focus (reviewed in Brown and Bishop, 2015). However, variation in filament stability or filament length could either generate variation in ChIP-seq enrichment profiles or render some RAD-51 foci undetectable cytologically. The fact that RAD-51 staining consistently yields foci with a wide range of intensities, and that foci are sometimes larger than diffraction-limited objects, adds weight to this possibility. An additional, nonexclusive possibility is that RAD-51 may have some propensity to associate with chromatin that is detectable by ChIP-seq but not cytologically.

Our results exclude several explanations for the loss of arm-enriched RAD-51 foci, including the existence of interference between DSBs (discussed below) and the non-uniform expansion or compaction of chromosomes during pachytene. They also argue against a role for the crossover assurance checkpoint, which monitors crossover formation and extends the DSB-permissive zone in response to crossover defects even on one chromosome. While it is tempting to speculate that the loss of arm-enriched DSBs corresponds to some early stage in the satisfaction of this checkpoint, the almost wild-type timing of the loss of arm-enriched DSBs in *him-8* and of residual arm-enriched DSBs in *him-5*—in which the assurance checkpoint is never satisfied and eventually overridden—argues against this hypothesis. Likewise, the loss of arm-enriched foci is unlikely to be a consequence of negative feedback regulation, given that we observe wild-type-like DSB distribution dynamics in *dsb-1*^{5AQ}, which is at least partially responsible for feedback-inhibition of DSB formation in *C. elegans*.

We favor explanations for the loss of arm enrichment that couple DSB formation to some feature of chromosome organization that changes gradually during pachytene and independently of recombination. Because the loss of arm enrichment and the elongation of axes happen at approximately the same time, it is tempting to speculate that the same change in chromosome organization drives both. Because chromosome axis length alone does not determine DSB distribution, this change must independently affect axis length and DSBs. This class of explanations is, nevertheless, consistent with all of our observations, including that the DSB distribution is insensitive to an increased number of DSBs and that in *him-5,* which is the only mutant we found in which axes do not elongate, there is also loss of early arm-enriched foci.

What features of chromatin or chromosome organization could be changing during pachytene? A prominent candidate is the pattern of histone modifications along the chromosome, which is known to differ significantly between the arms and center regions (Ho et al., 2014; Liu et al., 2011), and has been correlated with DSB distributions in yeast and mammals (reviewed in de Massy, 2013) and in *C. elegans* (Kotwaliwale and Dernburg, unpublished). Efforts to distinguish heterogeneity in the staining intensity of histone modifications enriched on chromosome arms during pachytene did not reveal significant differences (data not shown); however, it is possible that multiple modifications act combinatorially to promote or inhibit DSB formation, or that changes in the modification landscape are too subtle to detect cytologically.

Lack of measureable DSB interference

Crossover interference has remained an enigmatic feature of meiosis since its discovery in the early 20th century. Despite recent progress (Zhang et al., 2014), conserved principles remains elusive, and it is likely that several mechanisms, operating at different stages of crossover formation, play varyingly prominent roles in different organisms. Recent work in yeast has provided the first direct evidence that one of those mechanisms could be interference between DSBs themselves (Garcia et al., 2015). Although this study detected DSB interference only a range of approximately 70kb, crossover interference itself in yeast acts over a similar scale, so the possibility that longer range DSB interference operates in *C. elegans*—in which crossover interference acts over tens of megabases—is an intriguing possibility. Our high-throughput

cytological assay is the only practical way to detect such putative long-range DSB interference.

We did not detect any significant interference effect between adjacent RAD-51 foci. The modest short-range positive interference we observed may be an artifact, since a single DSB may give rise to two distinct but closely spaced foci if the two resected ends become separated by a sufficient distance (Brown et al., 2015; Kurzbauer et al., 2012). At larger distances, over which this effect is unlikely to confound our observations, we also observed no significant interference. Importantly, however, our measurements of DSB interference rely on the simultaneous presence of two RAD-51-associated DSBs. Interference could still exist between nascent DSBs and later, RAD-51-unmarked, stages of repair. Evidence in yeast that interference exists between crossovers and noncrossovers, but not between adjacent noncrossovers (Mancera et al., 2008), circumstantially supports this possibility. Because we also do not observe any interference between RAD-51 foci and GFP::COSA-1 foci, however, these RAD-51-unmarked recombination intermediates would have to be downstream of RAD-51 removal and upstream of COSA-1 localization.

Implications of unbiased chromosome conformation at DSBs and crossovers

Whether and how meiotic chromosome organization might respond to the formation of particular meiotic recombination intermediates, perhaps to implement crossover interference, has been a longstanding question. One prominent model for interference—the 'mechanical stress' model—proposes that interference is the product of coupling crossover formation to mechanical stress within either the chromosome itself or the chromosome axis (Kleckner et al., 2004; Zhang et al., 2014). In this model, the formation of a crossover is first 'triggered' or licensed by a state of high mechanical stress, and then later generates a 'defect' in the integrity of the stress-bearing feature. This defect causes the local relief of mechanical stress—over a distance dictated by the mechanical properties of the chromosome—and thereby inhibits the subsequent formation of crossovers nearby.

If this model explains the extremely strong interference effect observed in *C. elegans*, it implies that mechanical stress relief occurs throughout the chromosomes, with the strongest relief occurring near the site of crossover formation. A direct test of this model, therefore, would be to measure stress near and far from crossovers. Of course, even if the identity of the putative stress-bearing structure were clear, this is not technically possible. An indirect test, however, is possible by assuming that mechanical stress and chromosome stiffness are correlated (just as a spring is more difficult to bend when it is stretched) and to measure the curvature of the chromosome axis near and far from crossovers.

Our observation that chromosomes are not preferentially curved or un-curved near DSBs or crossovers is, therefore, circumstantial evidence against the mechanical stress model for interference. It is, however, tenuous at best, for it is possible that interference-mediating mechanical stress exists independently of the forces that dictate the chromosome conformations we can observe by light microscopy. It is also possible that stress relief occurs only during a very brief window of pachytene, or that it is triggered by a recombination intermediate downstream of RAD-51-marked DSBs and upstream of COSA-1-marked crossover sites.

Notably, however, the evidence that chromosome axes locally expand by approximately 0.3μm in response to crossover formation indicates that chromosome organization does undergo some persistent change on length scales accessible to light microscopy (Libuda et al., 2013). On larger scales, crossover formation triggers asymmetric, chromosome-wide remodeling along the crossover-demarcated 'long' and 'short' arms of the axis that culminates in the step-wise disassembly of the SC (Martinez-Perez et al., 2008). Super-resolution imaging using STORM suggests that this remodeling may be preceded by changes in the organization of components within the axis (Kohler and Dernburg, unpublished). It is possible that only this kind of higher-resolution imaging, perhaps coupled with live imaging of crossover formation and chromosome dynamics, will elucidate the connections between chromosome conformation and crossover formation.

METHODS

Mutations and strains

All strains were cultured at 20ºC under standard conditions. The wild-type strain was N2 Bristol. The following mutants were analyzed: *him-5(e1490)*, *him-8(tm611)*, *msh-5(me23)*, *spo-11(me44)*, and *dsb-1(ieSi25)*. Strains used in this work were:

CA148 *him-5(e1490) V*
CA257 *him-8(tm611) IV*
AV630 *meIs8 [pie-1p::GFP::cosa-1 + unc-119(+)] II*
PS2442 *dpy-20(e1282) IV; syIs44 [pPD49-78::lacI + lacO(256) + (pMH86) dpy-20(+)]*
CA279 *spo-11(me44)/mIs11 IV*
AV115 *msh-5(me23) IV/nT1[unc-?(n754) let-?] (IV;V)*
CA1139 *dsb-1(ieSi25) II; dsb-1(tm5034) IV*

FISH probe synthesis

Probes were designed using the Oligopaints method (Beliveau et al., 2012) and synthesized as in (Beliveau et al., 2014). Briefly, an oligo library was designed consisting of thermodynamically suitable oligos that hybridized within 100kb regions at the borders between the arm and center regions on chromosome III. Barcode sequences seven base pairs in length were appended to each oligo according to the region to which it hybridized. Library synthesis was performed by MYcroarray (Ann Harbor, Michigan). Oligos corresponding to a single probe were amplified from the library by PCR with appropriately barcoded and fluorescently labeled primers (IDT), digested with Nb.BsrDI, and the labeled single strand extracted by denaturing gel electrophoresis. A 200μL PCR yielded approximately 20 pmol of probe DNA, and robust labeling was achieved using 2 pmol of probe DNA in a 10μL hybridization volume (see below).

Immunofluorescence and FISH

Immunofluorescence was performed as described in (Phillips et al., 2009a), except that the tissue was washed and stained in eppendorf tubes, rather than on slides, and mounted just before imaging. Hermaphrodites 24-30 hours post-L4 were dissected in

egg buffer containing 0.2% Tween 20. Extruded gonads were fixed for 30 seconds in 1% formaldehyde, washed in 1mL PBST, incubated in methanol at -20ºC for 1 minute, and washed three times in PBST. The gonads were blocked with Roche blocking agent for 30 minutes at room temperature, stained with primary antibodies in block for 12-24 hours at 4ºC, washed three times in PBST, stained with secondary antibodies for 2 hours at room temperature, washed three times in PBST, and then transferred to Histobond slides and mounted in Prolong Gold mounting medium. The anti-HTP-3 antibody was a polyclonal chicken antibody described previously (MacQueen et al., 2005) and was used at 1:500. The RAD-51 antibody was an affinity purified rabbit polyclonal antibody (Novus 2948.00.02) and used at 1:10000. A commercial monoclonal GFP antibody (Roche) was used to amplify the GFP::COSA-1 signal at 1:300. Commercial secondary antibodies were from Jackson Immunoresearch or Molecular Probes and were used at 1:500. FISH was performed as in (Phillips et al., 2009a) except that, as for IF, the hybridization was performed in Eppendorf tubes instead of on slides. Dissected gonads were fixed for 2 minutes in 2% formaldehyde, washed in 1mL PBST, incubated in methanol for 1 minute, and washed three times in 2x SSCT, and then transferred to 1mL of 50% formamide in 1x SSCT and incubated overnight at 37ºC. For hybridization, the gonads were transferred to a 10-12uL mix of hybridization buffer and FISH probe (see above), and the samples denatured at 91ºC for 2 minutes in a thermocycler followed by overnight incubation at 37ºC. After final washes in 1x SSCT, the gonads were immunostained and mounted as described above.

Fluorescence microscopy

All images were acquired using a DeltaVision OMX structured illumination microscope (Applied Precision) equipped with an Olympus 100x NA 1.40 objective. Immersion oil with a refractive index of 1.516 was used, as this yielded, empirically, the least asymmetric point spread functions with our samples. Three-dimensional images spanned 4-6μm and z-slices were taken every 125nm. Image reconstruction was performed in SoftWoRx (Applied Precision) using a Wiener filter constant of 0.01. Reconstructed images were analyzed as described in Chapter 2.

Chapter 4 Observing homolog interactions using FISH

Introduction

How homologous chromosomes recognize one another is one of the enduring mysteries of meiosis. In organisms in which homolog pairing depends upon the initiation of meiotic recombination, we at least know that the basis of homology assessment is provided by the search for a homologous repair template. In these organisms, the mystery of pairing is how recombinational interactions between homologs are selectively stabilized while ectopic interactions are eliminated. In organisms that do not require recombination for homolog pairing, however, pairing poses an even deeper mystery, for not even the molecular basis of homology assessment—and, indeed, whether one even exists—is known.

Perhaps the most prominent model system in which homolog pairing occurs independently of recombination is *C. elegans*. In this organism, pairing activity is restricted to a specific region near one end of each chromosome (MacQueen et al., 2005). These regions, called pairing centers (PCs), are defined by the enrichment of a motif recognized by one of a family of zinc finger proteins—ZIM-1,-2,-3, and HIM-8 (Phillips and Dernburg, 2006; Phillips et al., 2005, 2009b). These proteins recruit their corresponding PC to the nuclear envelope, where a protein complex that spans the nuclear envelope tethers each PC to the nuclear periphery and connects it to cytoskeletal motor proteins (Sato et al., 2009). These connections enable rapid PC-led chromosome movements, catalyzing the homolog recognition process and playing an important role in licensing homologous synapsis (Penkner et al., 2009; Sato et al., 2009; Wynne et al., 2012). Pairing selectivity is not completely determined by zinc finger binding, however, because the PCs of two pairs of autosomes are bound by the same zinc finger proteins. Nevertheless, it is clear that PCs are sufficient to license synapsis between otherwise nonhomologous chromosomes, implying that homology assessment involves only loci or regions within the PCs. Whether this assessment involves intermingling of PC regions, superficial contact between PCs, or only contact between epigenetic features or PC-associated factors remains unknown.

One of the experimental challenges that has limited our understanding of homolog pairing is the difficulty of observing interactions between homologs. At the molecular level, the formation of recombination intermediates between homologs can be monitored by hybridizing two-dimensional Southern blots with homolog-specific probes (Bzymek et al., 2010; Oh et al., 2007; Schwacha and Kleckner, 1995). This biochemical technique cannot, however, observe recombinational or other interactions between homologs in situ. Meanwhile, cytological methods of labeling particular chromosomal loci in fixed tissue or living organisms can determine whether particular homologous loci are colocalized or not, but cannot distinguish one homolog from another. Methods based on rolling-circle amplification have been developed to label particular single nucleotide polymorphisms in situ (Larsson et al., 2004; Zhong et al., 2001), but these methods are inefficient and cannot be used to label larger homologous regions.

Despite its limitations, fluoresence in situ hybridization (FISH) has long been the most flexible and robust of the methods available for cytologically labeling chromosomes. Recently, the development of bioinformatically designed FISH probes has significantly elevated the versatility of FISH by allowing the investigator to select the

constituent oligos of each probe (Beliveau et al., 2012). This approach has numerous advantages: it bypasses the need to clone the genomic region of interest, yields more robust probes, and allows the design of probes targeting any non-repetitive chromosomal locus or region.

Using the design control provided by this approach, it is also possible to design homolog-specific FISH probes by restricting probe composition to only those oligos that overlap single nucleotide polymorphisms (SNPs). Provided that a sufficient density of SNPs exists in the region of interest, a pair of probes—one consisting of oligos carrying the SNP variants of one homolog, and one consisting of oligos carrying those of the other—can be generated that preferentially hybridize to their corresponding homolog. This strategy has been successfully used to differentially label large homologous chromosomal regions in fixed tissue from Drosophila and mouse hybrids (Beliveau et al., 2015). Here, we apply the same approach to generate homolog-specific FISH probes to regions in or near pairing centers in *C. elegans* in order to observe interactions between homologs. We find that regions within pairing centers often colocalize in the transition zone, but not in pachytene. Regions near, but outside of, pairing centers do not often colocalize either in the transition zone or in pachytene. This selective colocalization of pairing center regions does not appear to depend on synapsis or be extended in its absence. Finally, we do not find obvious evidence for large-scale interactions between homologs at or near crossovers.

RESULTS

Robust and specific homolog labeling using OligoPaint FISH probes

The design of homolog-specific Oligopaint probes in *C. elegans* requires the existence of two strains with a relatively high density of SNPs between them. In mouse and Drosophila, a SNP density of approximately one SNP per 1-2kb was sufficient to yield bright FISH signals. Fortunately, the well-characterized Hawaiian isolate CB4856 possesses approximately this density of SNPs relative to the N2 lab strain. Using the database of Hawaiian SNPs (Wormbase, 2015) and the published library of suitable oligoPaint oligos (Beliveau et al., 2012), we plotted the density of SNPs along each chromosome to identify regions with locally high oligo and SNP densities that would be most amenable to homolog-specific labeling (Figure 4.1). Among these regions, we identified several 250kb-long regions that were located within, near, and far from pairing centers. Separately, we also designed probes to label the entire 2mb-wide pairing center region on chromosome V in order to visualize the interactions between larger homologous regions.

We first tested homolog probe pairs using a standard FISH protocol (see Methods) in N2-Hawaiian hybrid offspring. In all regions of both hermaphrodite and male gonads, we observed differentially localized foci in the two probe channels. In pachytene, these foci were usually adjacent to one another, as expected for synapsed chromosomes, and occasionally appeared to colocalize in projected images (Figure 4.3). In the premeiotic zone, we observed either one or two foci in each probe channel; these foci were not paired with the foci of the cognate probe, as expected (Figure 4.2). In very late pachytene, when the SC begins to disassemble, we correspondingly once again often observed unpaired foci (Figure 4.3). Finally, in male gonads, in which a

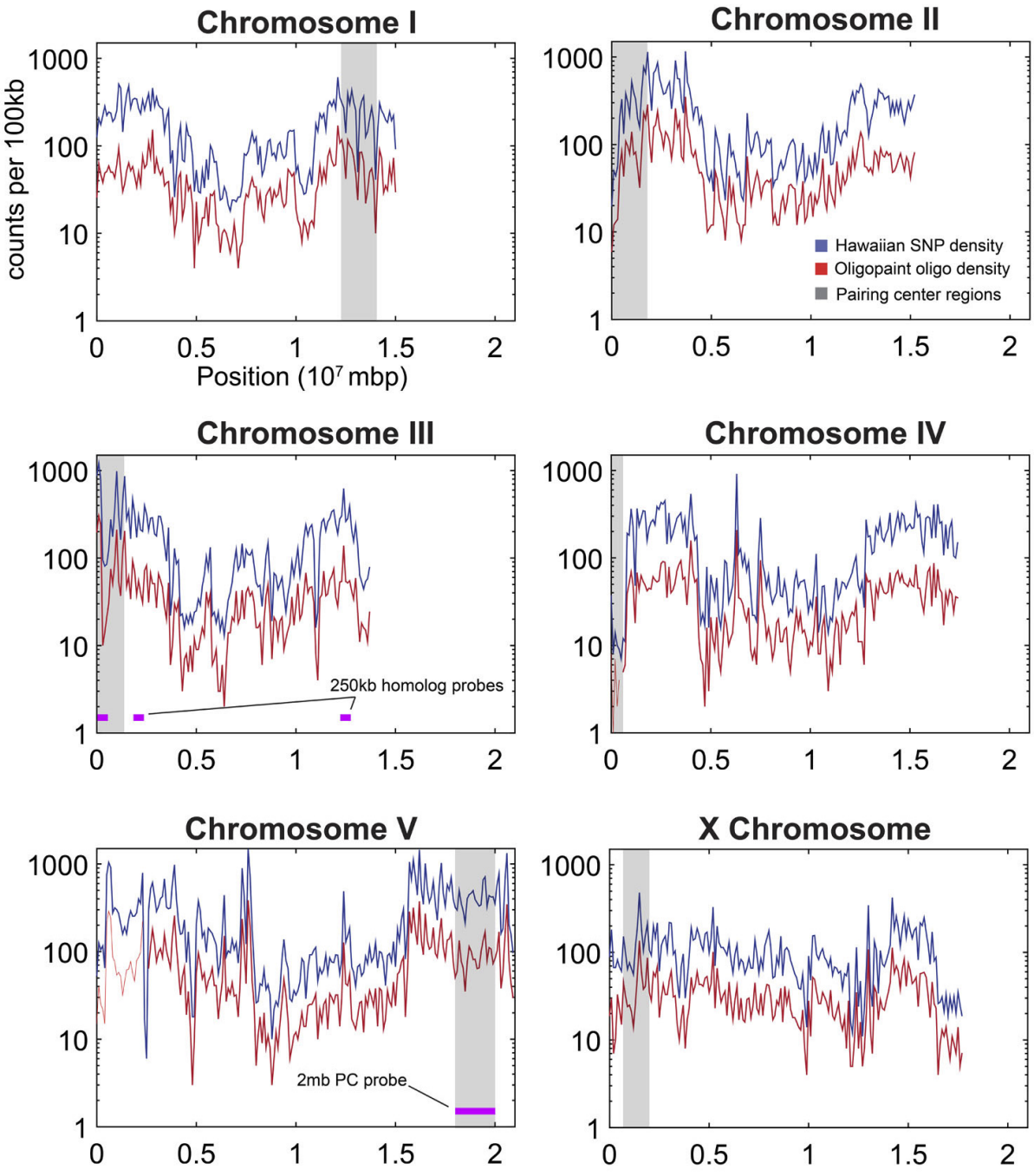


Figure 4.1 Distribution of SNPs and homolog probe design
Distribution of Hawaiian SNPs along each chromosome (blue) and distribution of oligoPaint-eligible oligos that intersect at least one SNP (red). Probes were designed to the regions highlighted in magenta. The approximate position and width of each pairing center is annotated in light gray.

large population of sperm nuclei is visible in a single field of view, we observe in each nucleus either a focus in one homolog probe channel or the other, but not both, consistent with specific labeling of segregated maternal and paternal homologs.

Additional controls confirmed the homolog specificity of our probe pairs. When both homolog probes were hybridized to gonads from either N2 or Hawaiian hermaphrodites, only the N2 or Hawaiian probes, respectively, yielded bright foci, as expected (Figure 4.4A). Further, when we hybridized the Hawaiian probe alone to N2 gonads, we did not observe foci as bright as those observed from the N2 probe, indicating that the Hawaiian SNP variants were sufficient to inhibit efficient hybridization of the Hawaiian probe to the N2 homolog. We obtained a similar and even more dramatic result from hybridizing the N2 probe to Hawaiian gonads; in this case, no clear foci could be detected, indicating low affinity of the N2 probe for the Hawaiian homolog (Figure 4.4B).

Homologous regions occupy distinct volumes in pachytene

Synapsed loci visualized by FISH in *C. elegans* often appear as two adjacent but distinct fluorescent foci (refs). The most parsimonious explanation for this observation is that each focus corresponds to a single homolog, implying that synapsed homologous loci are usually well separated from one another. We visualized the localization of four different regions using homolog-specific Oligopaint probes and observed consistent separation between the two homologs at each region in pachytene (Figure 4.3, 3.5). Foci that appeared to overlap in maximum intensity projections did not overlap in the original three-dimensional images. We verified that our failure to observe frequent colocalization between homologous regions was not an artifact of poor registration between the two fluorescent probe channels by using custom image registration algorithms and control images of tissue identically labeled in all channels to validate alignment accuracy throughout the full three-dimensional volume observed in each field of view (see Methods).

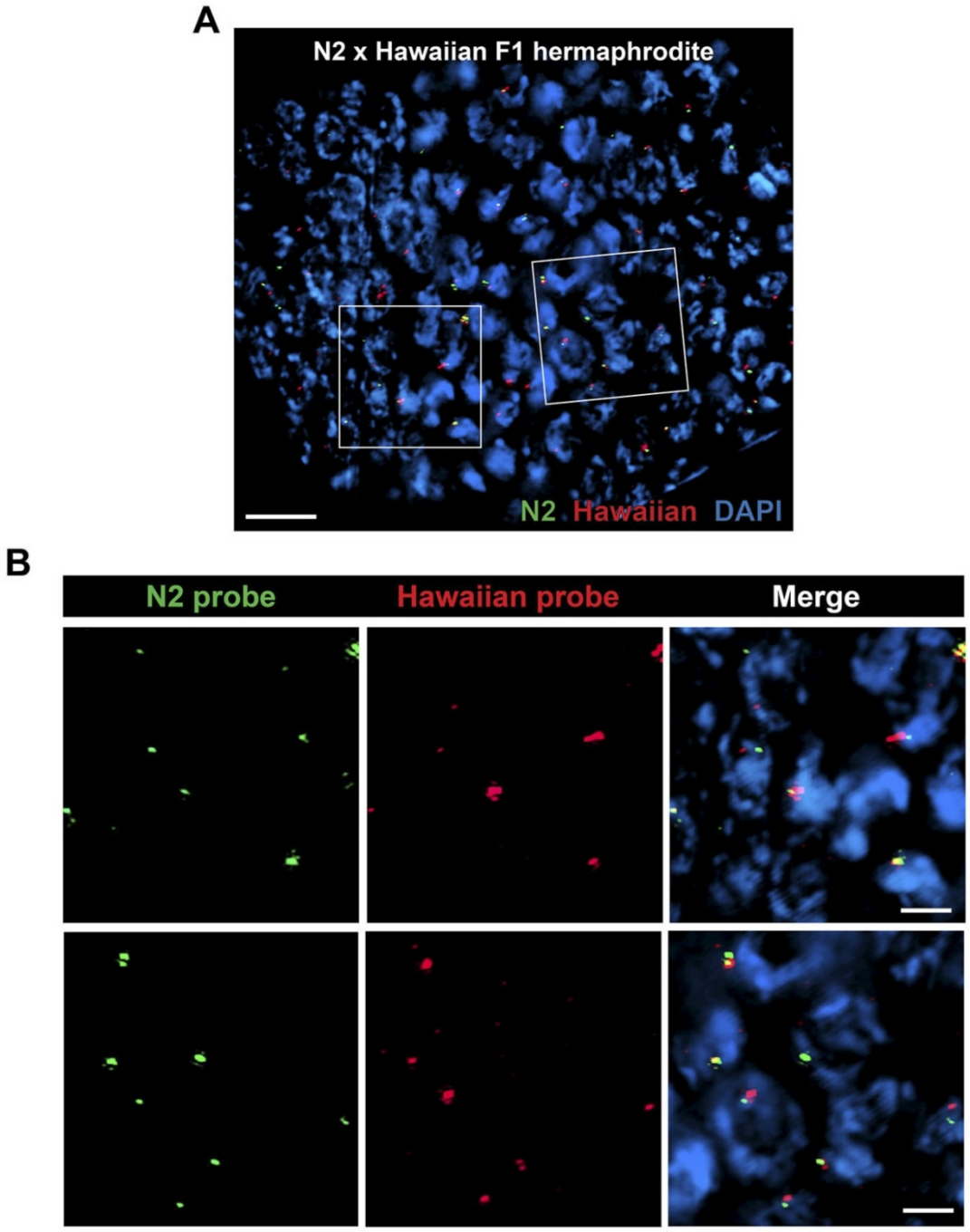


Figure 4.2 Localization of a 250kb region in the Chromosome III pairing center in the transition zone
(A) Overview of the transition zone in an N2-Hawaiian hybrid hermaphrodite. A 250kb region in the pairing center on chromosome III is labeled with homolog-specific probes. Meiosis proceeds from left to right. (B) Magnified views of the regions outlined in (A). Nuclei with both paired and unpaired chromosome III PCs are apparent.

Homologous regions within a pairing center colocalize in the transition zone

In the transition zone, homology assessment takes place between pairing centers and leads, relatively rapidly, to stable pairing. Cytologically, pairing is observed by colocalization of either the PC-bound zinger finger proteins or by labeling PC loci with FISH. How pairing centers interact during and immediately after pairing is not known; it is possible that the interactions are only superficial or that they involve dense intermingling of pairing center chromatin. We visualized the localization of a 250kb region on the left end of the chromosome III pairing center in the transition zone and homology assessment involves the intermingling of pairing center chromatin. Notably, in *syp-3* mutant hybrids, we did not observe intermingling more extensive than that observed in wild-type hybrids in the transition zone (Figure 4-6C-D). This suggests that formation of the SC between paired homologs does not drive the transition from intermingled to well-separated homologous PCs that we observe in wild-type gonads.

Homologs do not detectably interact at crossovers

Crossovers are, by definition, sites at which homologous chromosomes interact biochemically. The extent to which this molecular-scale interaction coincides with colocalization or intermingling of homologous chromosomes on larger scales is not known. Because we could not combine our FISH protocol with immunofluorescence to localize crossovers cytologically, we observed homolog interactions near crossovers indirectly. We labeled a 2mb region on the right end of chromosome V using homolog-specific probes, and compared the localization of homologs in wild-type N2-Hawaiian hybrids to their localization in hybrids heterozygous for the translocation *nT1(IV;V)*, in which crossover formation is restricted to the right end of chromosome V. If crossovers triggered large-scale colocalization of nearby homologous loci, we would expect to observe more frequently colocalized homolog FISH signals in the *nT1* heterozygotes, in which crossovers often form in the labeled region, than in the wild-type hybrid. This is not what we observed; we could not detect a significant difference in the frequency of colocalization (Figure 4.6E), suggesting that crossover formation does not trigger homolog colocalization at resolutions observable by light microscopy.

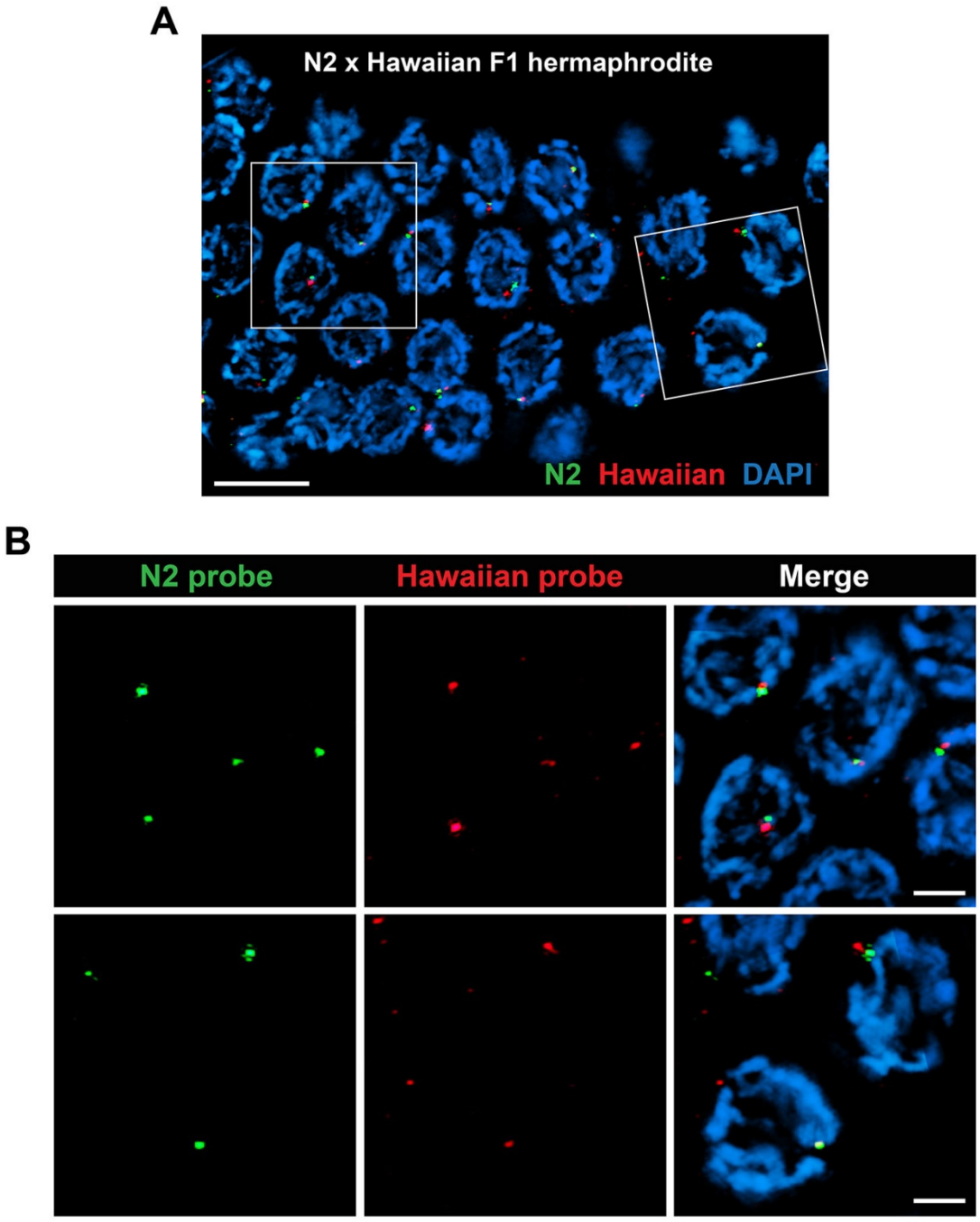


Figure 4.3 Localization of a 250kb region in the Chromosome III pairing center during pachytene and at diakinesis
(A) Late pachytene in an N2-Hawaiian hybrid hermaphrodite. A 250kb region in the pairing center on chromosome III is labeled with homolog-specific probes. Meiosis proceeds from left to right. (B) Magnified views of the regions outlined in (A). In most nuclei, the homologous regions remain paired, but as nuclei enter diakinesis, pairing is lost as the SC disassembles.

DISCUSSION

Here, we have demonstrated robust homolog-specific labeling using the Oligopaints method of FISH probe synthesis in the germline of *C. elegans*. Notably, the labeling we observe does not appear to strongly depend on the existence of competition between homolog probe pairs, surprisingly implying that a single SNP within the 32-basepair homology region in each oligo is alone sufficient to prevent most nonhomologous hybridization. It is not clear why the published demonstration of homolog Oligopaints, which required competition between probe pairs for homolog-specific hybridization (Beliveau et al., 2015), conflicts with this observation. Nevertheless, coupled with our consistent observation of unpaired homolog foci in the premeiotic zone and during SC disassembly at diakinesis, this observation strongly suggests that the labeling we observe is homolog-specific.

The most striking preliminary observation we have made using homolog-specific probes is that, while most homologous regions are well-separated during meiotic prophase, a region within the chromosome III PC is often colocalized with its homologous partner specifically in the transition zone. Unfortunately, the harsh fixation required to preserve chromosome morphology is not compatible with most antibodies, preventing the combination of homolog FISH with immunofluorescence to determine how PC colocalization correlates with the presence of PC-associated proteins or axis components. Future experiments, however, will be able to determine the genetic requirements of colocalization and, by extension, whether this colocalization is required for pairing or is merely a consequence of chromosome organization in the transition zone.

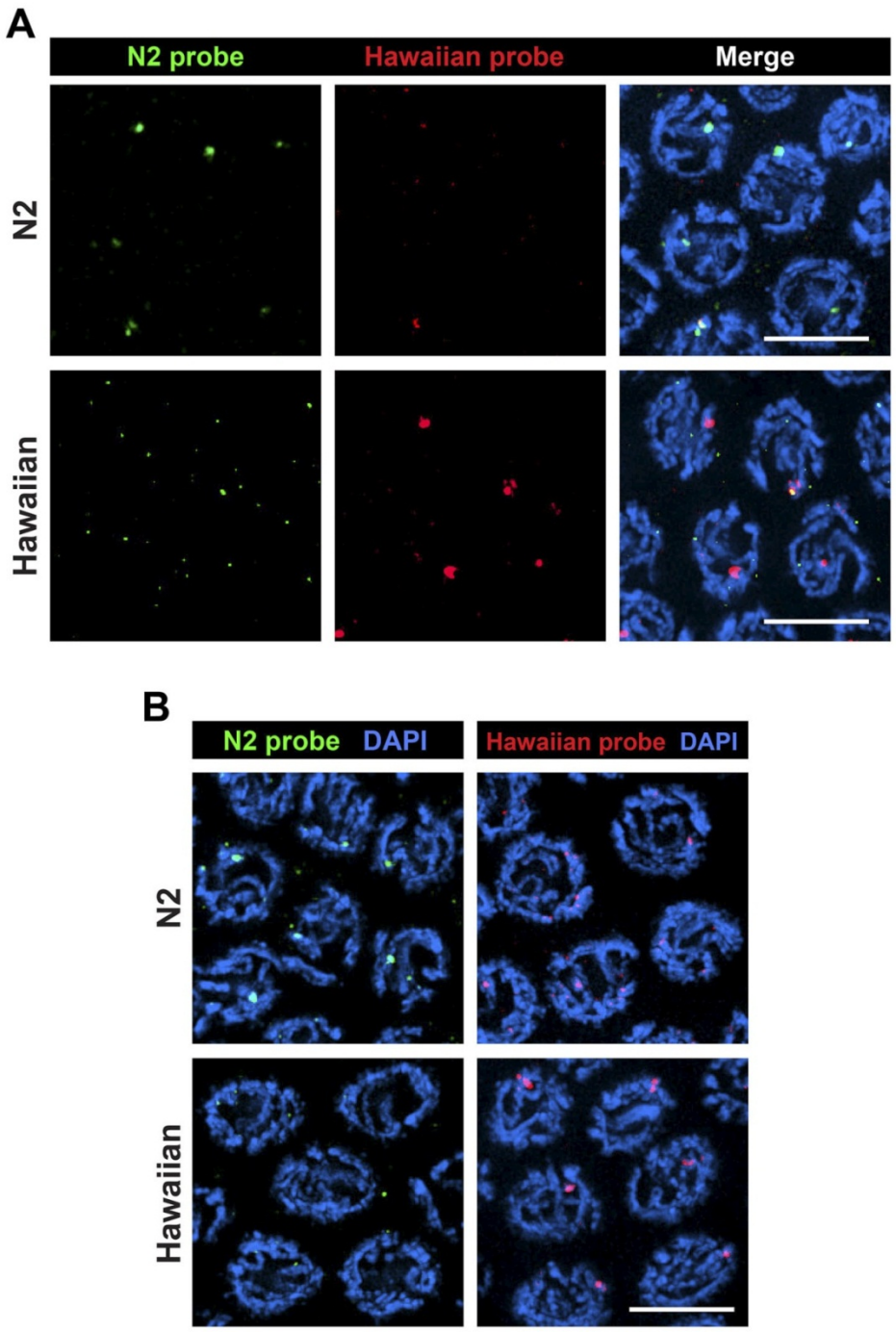


Figure 4.4 Homolog probe hybridization is specific and robust
(A) Hybridization of a homolog probe pair targeting the 2mb pairing center on chromosome V in N2 and Hawaiian hermaphrodites. Only the N2 or Hawaiian probe, respectively, yields a bright FISH signal. (B) Hybridization of single probes to N2 and Hawaiian hermaphrodites. In N2, the Hawaiian probe alone yields only weak foci, while in Hawaiian, the N2 probe fails to yield detectable foci.

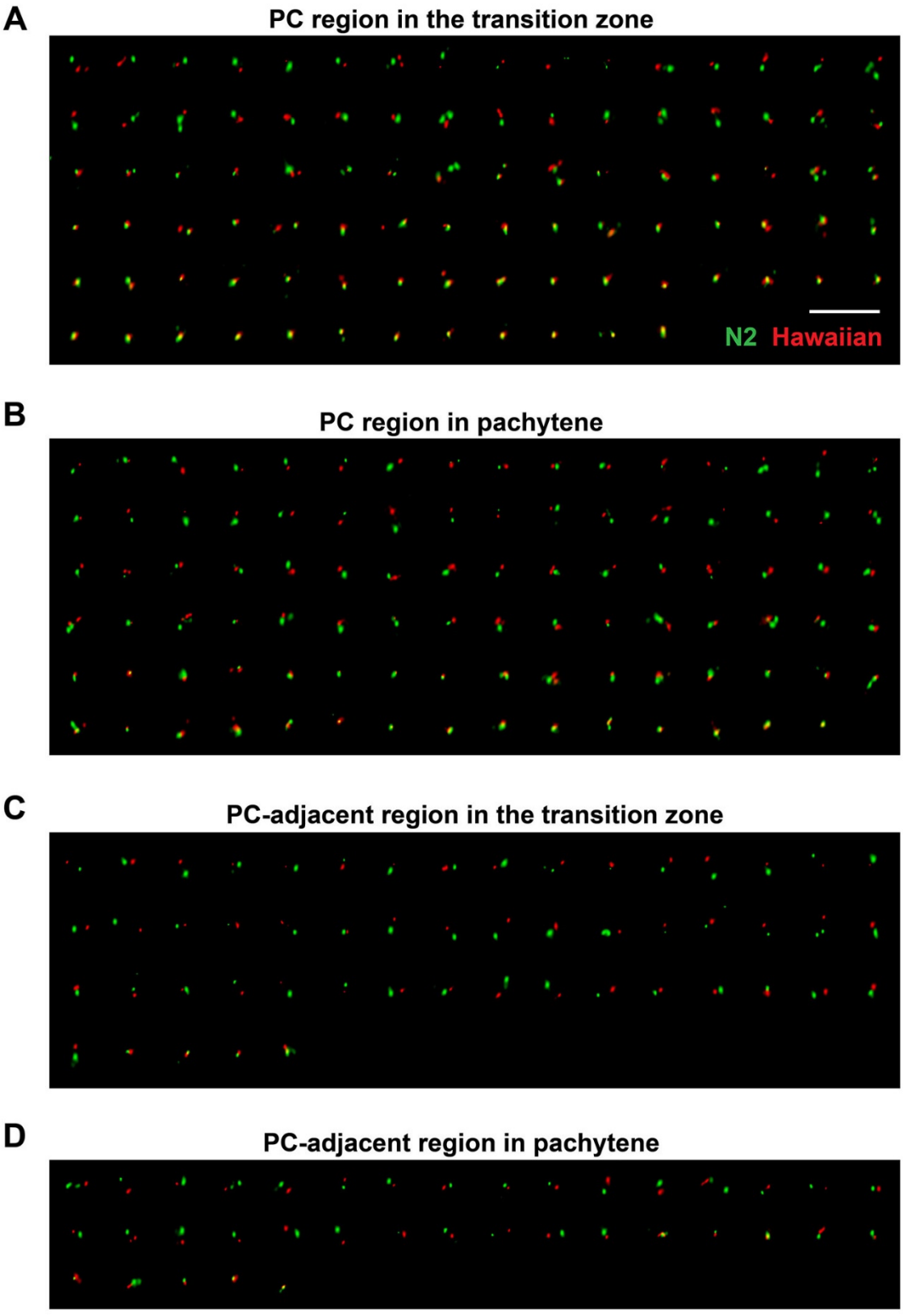

A
PC region in the transition zone
N2 Hawaiian
B
PC region in pachytene
C
PC-adjacent region in the transition zone
D
PC-adjacent region in pachytene

Figure 4.5 Chromosome III homolog FISH suggests pairing center regions colocalize specifically in the transition zone

Cropped and tiled images of foci aggregated from several gonads for two different probes in the transition zone and pachytene. Each pair of foci is ordered from left to right and top to bottom according to the degree to which the two foci overlap. (A) and (B) Foci corresponding to a 250kb region in the pairing center of chromosome III often colocalize in the transition zone, but not in pachytene. (C) and (D) Foci corresponding to a 250kb region approximately 200kb to the right of the pairing center on chromosome III do not often colocalize in either the transition zone or pachytene.

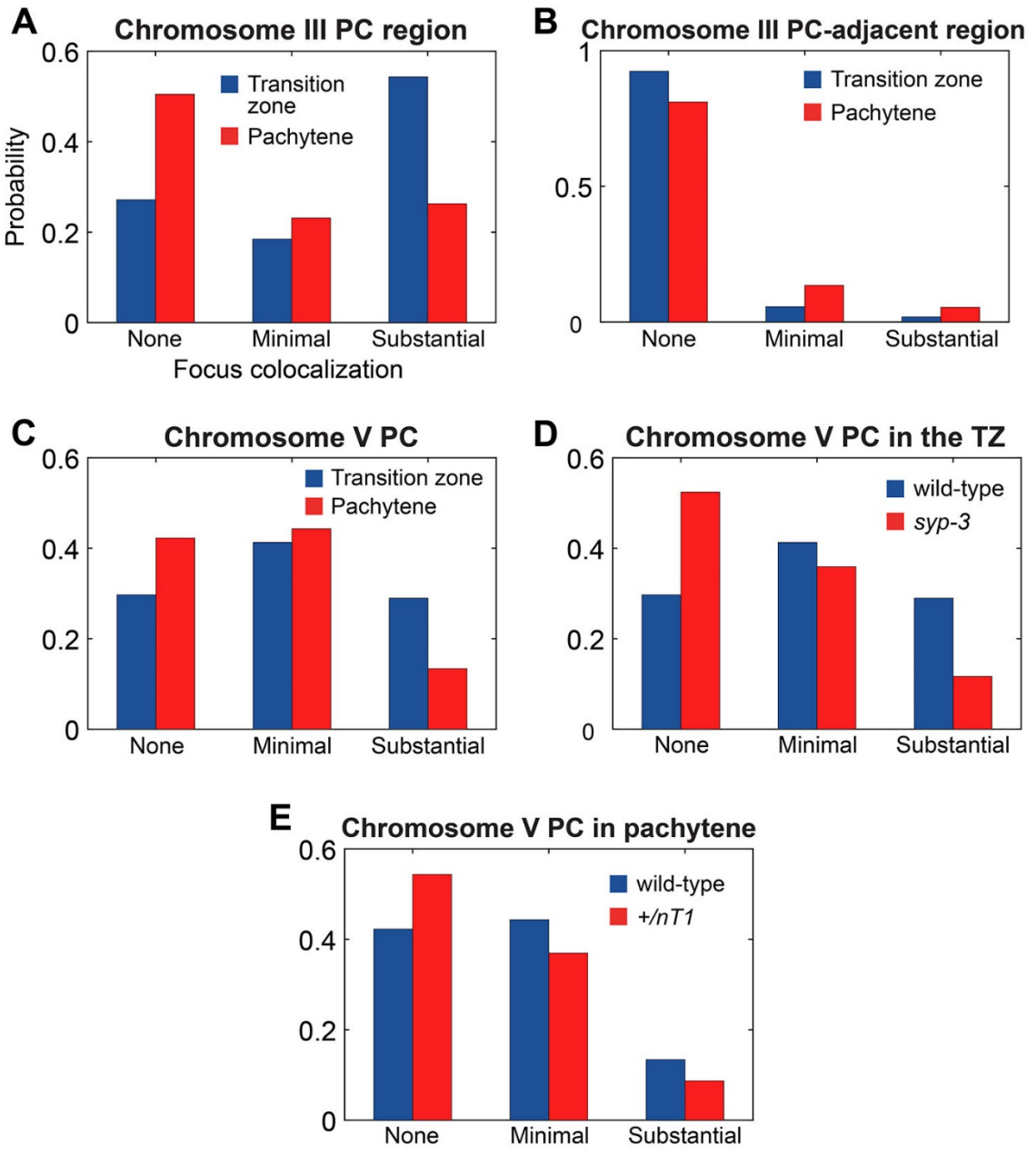


Figure 4.6 Quantification of homolog FISH focus overlap
(A) and (B) A 250kb region in the chromosome III pairing center often colocalizes in the transition zone, but not in pachytene; a 250kb region adjacent to the same pairing center almost never colocalizes. (C) Analogous, but less dramatic, results for a probe to the entire 2mb pairing center of chromosome V, which more frequently overlaps in the transition zone than in pachytene. (D) Chromosome V pairing center colocalization in the transition zone in wild-type and *syp-3* mutants. (E) Chromosome V pairing center colocalization does not differ in *nT1* heterozygotes, in which crossovers are biased to occur in the labeled region.

METHODS

Mutations and strains

All strains were cultured at 20ºC under standard conditions. The wild-type strain was N2 Bristol. The Hawaiian isolate (CB4856) was obtained from the Caenorhabditis Genetics Center. All hybrid crosses were between N2-background hermaphrodites and Hawaiian-background males. The *syp-3(ok758)* mutant was 'balanced' in the Hawaiian background by the presence of a rescuing *EmGFP-SYP-3* transgene (Rog and Dernburg, 2015); both loci were independently introgressed into Hawaiian at least six times. To generate homozygous *syp-3* hybrids, *syp-3* heterozygotes in the N2 background were crossed to Hawaiian males heterozygous for both *syp-3* and *EmGFP-SYP-3*; progeny homozygous for *syp-3* were then identified by the presence of 12 DAPI-staining bodies at diakinesis. Finally, to generate the translocation heterozygotes, the reciprocal translocation *nT1(IV;V)* was maintained in the N2 background, crossed to wild-type Hawaiian males, and heterozygous F1 hybrids selected.

Homolog probe design

A list of homolog probe oligos was generated by searching the database of all candidate oligoPaint oligos (available online at genetics.med.harvard.edu/oligopaints) for oligos that intersected at least one Hawaiian SNP in the SNP database available from wormbase.org. For a variety of reasons, these SNP-intersecting oligos are not distributed uniformly throughout the genome (Figure 4.1). Probe design was therefore guided by the location of loci or regions with a high density of SNP-intersecting oligos. Once selected, all probe pairs were pooled in a single oligo library and selectively amplified using the same 7mer barcode sequences described in Chapter 3.

FISH probe synthesis, sample preparation, FISH, and microscopy

Probe synthesis using the PCR-based Oligopaints method was as described in Chapter 3. For consistency, all N2 probes were labeled with cy3, and all Hawaiian probes with cy5 (IDT). Sample preparation was as described in Chapter 3 but with a different fixation to better preserve chromatin morphology. Dissected gonads were fixed in 0.8% EGS for 20-30 minutes, incubated in 100% ethanol at -20ºC for at least five minutes, washed in PBST twice, and post-fixed in 3.7% formaldehyde for 20 minutes. Overnight pre-hybridization in 50% formamide, followed by denaturation and hybridization, was performed as described in Chapter 3. The 0.8% EGS fix was prepared as in (Phillips et al., 2009a), and was necessary to obtain unperturbed DAPI morphology (note, however, that most antibodies do not work well with this fix). Slide preparation and SIM imaging were performed using an OMX system as described in Chapter 3.

Image analysis

SIM images were reconstructed and registered using SoftWoRx as described in Chapter 3. The image registration was verified using control samples in which the chromosome axis was stained in both homolog probe channels. Custom MATLAB scripts were used to crop foci in three dimensions from each field of view. The degree of overlap between homolog foci was scored by calculating the covariance between the two homolog probe foci.

References

Alpi, A., Pasierbek, P., Gartner, A., and Loidl, J. (2003). Genetic and cytological characterization of the recombination protein RAD-51 in Caenorhabditis elegans. Chromosoma *112*, 6–16.

Barnes, T.M., Kohara, Y., Coulson, A., and Hekimi, S. (1995). Meiotic recombination, noncoding DNA and genomic organization in Caenorhabditis elegans. Genetics *141*, 159–179.

Baudat, F., and de Massy, B. (2007). Regulating double-stranded DNA break repair towards crossover or non-crossover during mammalian meiosis. Chromosome Res. Int. J. Mol. Supramol. Evol. Asp. Chromosome Biol. *15*, 565–577.

Baudat, F., Imai, Y., and de Massy, B. (2013). Meiotic recombination in mammals: localization and regulation. Nat. Rev. Genet. *14*, 794–806.

Beliveau, B.J., Joyce, E.F., Apostolopoulos, N., Yilmaz, F., Fonseka, C.Y., McCole, R.B., Chang, Y., Li, J.B., Senaratne, T.N., Williams, B.R., et al. (2012). Versatile design and synthesis platform for visualizing genomes with Oligopaint FISH probes. Proc. Natl. Acad. Sci. U. S. A. *109*, 21301–21306.

Beliveau, B.J., Apostolopoulos, N., and Wu, C. (2014). Visualizing genomes with Oligopaint FISH probes. Curr. Protoc. Mol. Biol. Ed. Frederick M Ausubel Al *105*, Unit 14.23.

Beliveau, B.J., Boettiger, A.N., Avendaño, M.S., Jungmann, R., McCole, R.B., Joyce, E.F., Kim-Kiselak, C., Bantignies, F., Fonseka, C.Y., Erceg, J., et al. (2015). Single-molecule super-resolution imaging of chromosomes and in situ haplotype visualization using Oligopaint FISH probes. Nat. Commun. *6*, 7147.

Bhalla, N., and Dernburg, A.F. (2008). Prelude to a division. Annu. Rev. Cell Dev. Biol. *24*, 397–424.

Bishop, D.K., and Zickler, D. (2004). Early decision; meiotic crossover interference prior to stable strand exchange and synapsis. Cell *117*, 9–15.

Blat, Y., Protacio, R.U., Hunter, N., and Kleckner, N. (2002). Physical and functional interactions among basic chromosome organizational features govern early steps of meiotic chiasma formation. Cell *111*, 791–802.

de Boer, E., and Heyting, C. (2006a). The diverse roles of transverse filaments of synaptonemal complexes in meiosis. Chromosoma *115*, 220–234.

de Boer, E., and Heyting, C. (2006b). The diverse roles of transverse filaments of synaptonemal complexes in meiosis. Chromosoma *115*, 220–234.

de Boer, E., Stam, P., Dietrich, A.J.J., Pastink, A., and Heyting, C. (2006). Two levels of interference in mouse meiotic recombination. Proc. Natl. Acad. Sci. U. S. A. *103*, 9607–9612.

Börner, G.V., Kleckner, N., and Hunter, N. (2004). Crossover/noncrossover differentiation, synaptonemal complex formation, and regulatory surveillance at the leptotene/zygotene transition of meiosis. Cell *117*, 29–45.

Brenner, S. (1974). The genetics of Caenorhabditis elegans. Genetics *77*, 71–94.

Brown, M.S., and Bishop, D.K. (2015). DNA strand exchange and RecA homologs in meiosis. Cold Spring Harb. Perspect. Biol. *7*, a016659.

Brown, M.S., Grubb, J., Zhang, A., Rust, M.J., and Bishop, D.K. (2015). Small Rad51 and Dmc1 Complexes Often Co-occupy Both Ends of a Meiotic DNA Double Strand Break. PLoS Genet. *11*, e1005653.

Buhler, C., Borde, V., and Lichten, M. (2007). Mapping meiotic single-strand DNA reveals a new landscape of DNA double-strand breaks in Saccharomyces cerevisiae. PLoS Biol. *5*, e324.

Bzymek, M., Thayer, N.H., Oh, S.D., Kleckner, N., and Hunter, N. (2010). Double Holliday junctions are intermediates of DNA break repair. Nature *464*, 937–941.

Carballo, J.A., Panizza, S., Serrentino, M.E., Johnson, A.L., Geymonat, M., Borde, V., Klein, F., and Cha, R.S. (2013). Budding yeast ATM/ATR control meiotic double-strand break (DSB) levels by down-regulating Rec114, an essential component of the DSB-machinery. PLoS Genet. *9*, e1003545.

Carlton, P.M., Farruggio, A.P., and Dernburg, A.F. (2006). A link between meiotic prophase progression and crossover control. PLoS Genet. *2*, e12.

Caselles, V., Kimmel, R., and Sapiro, G. (1997). Geodesic Active Contours. Int. J. Comput. Vis. *22*, 61–79.

C. elegans Sequencing Consortium (1998). Genome sequence of the nematode C. elegans: a platform for investigating biology. Science *282*, 2012–2018.

Christophorou, N., Rubin, T., and Huynh, J.-R. (2013). Synaptonemal Complex Components Promote Centromere Pairing in Pre-meiotic Germ Cells. PLoS Genet. *9*, e1004012.

Colaiácovo, M.P. (2006). The many facets of SC function during C. elegans meiosis. Chromosoma *115*, 195–211.

Colaiácovo, M.P., MacQueen, A.J., Martinez-Perez, E., McDonald, K., Adamo, A., La Volpe, A., and Villeneuve, A.M. (2003). Synaptonemal complex assembly in C. elegans

is dispensable for loading strand-exchange proteins but critical for proper completion of recombination. Dev. Cell *5*, 463–474.

Cole, F., Kauppi, L., Lange, J., Roig, I., Wang, R., Keeney, S., and Jasin, M. (2012). Homeostatic control of recombination is implemented progressively in mouse meiosis. Nat. Cell Biol. *14*, 424–430.

Comeron, J.M., Ratnappan, R., and Bailin, S. (2012). The many landscapes of recombination in Drosophila melanogaster. PLoS Genet. *8*, e1002905.

Davis, L., and Smith, G.R. (2006). The meiotic bouquet promotes homolog interactions and restricts ectopic recombination in Schizosaccharomyces pombe. Genetics *174*, 167–177.

Dernburg, A.F., McDonald, K., Moulder, G., Barstead, R., Dresser, M., and Villeneuve, A.M. (1998). Meiotic recombination in C. elegans initiates by a conserved mechanism and is dispensable for homologous chromosome synapsis. Cell *94*, 387–398.

Fraune, J., Schramm, S., Alsheimer, M., and Benavente, R. (2012). The mammalian synaptonemal complex: protein components, assembly and role in meiotic recombination. Exp. Cell Res. *318*, 1340–1346.

Fung, J.C., Rockmill, B., Odell, M., and Roeder, G.S. (2004). Imposition of crossover interference through the nonrandom distribution of synapsis initiation complexes. Cell *116*, 795–802.

Garcia, V., Gray, S., Allison, R.M., Cooper, T.J., and Neale, M.J. (2015). Tel1(ATM)-mediated interference suppresses clustered meiotic double-strand-break formation. Nature *520*, 114–118.

Glynn, E.F., Megee, P.C., Yu, H.-G., Mistrot, C., Unal, E., Koshland, D.E., DeRisi, J.L., and Gerton, J.L. (2004). Genome-wide mapping of the cohesin complex in the yeast Saccharomyces cerevisiae. PLoS Biol. *2*, E259.

Goldfarb, T., and Lichten, M. (2010). Frequent and efficient use of the sister chromatid for DNA double-strand break repair during budding yeast meiosis. PLoS Biol. *8*, e1000520.

Gonzalez-Serricchio, A.S., and Sternberg, P.W. (2006). Visualization of C. elegans transgenic arrays by GFP. BMC Genet. *7*, 36.

Goodyer, W., Kaitna, S., Couteau, F., Ward, J.D., Boulton, S.J., and Zetka, M. (2008). HTP-3 links DSB formation with homolog pairing and crossing over during C. elegans meiosis. Dev. Cell *14*, 263–274.

Gruhn, J.R., Rubio, C., Broman, K.W., Hunt, P.A., and Hassold, T. (2013). Cytological studies of human meiosis: sex-specific differences in recombination originate at, or prior to, establishment of double-strand breaks. PloS One *8*, e85075.

Gustafsson, M.G. (2000). Surpassing the lateral resolution limit by a factor of two using structured illumination microscopy. J. Microsc. *198*, 82–87.

Gustafsson, M.G.L., Shao, L., Carlton, P.M., Wang, C.J.R., Golubovskaya, I.N., Cande, W.Z., Agard, D.A., and Sedat, J.W. (2008). Three-dimensional resolution doubling in wide-field fluorescence microscopy by structured illumination. Biophys. J. *94*, 4957–4970.

Hayashi, M., Mlynarczyk-Evans, S., and Villeneuve, A.M. (2010). The synaptonemal complex shapes the crossover landscape through cooperative assembly, crossover promotion and crossover inhibition during Caenorhabditis elegans meiosis. Genetics *186*, 45–58.

Henderson, K.A., and Keeney, S. (2005). Synaptonemal complex formation: where does it start? BioEssays News Rev. Mol. Cell. Dev. Biol. *27*, 995–998.

Henzel, J.V., Nabeshima, K., Schvarzstein, M., Turner, B.E., Villeneuve, A.M., and Hillers, K.J. (2011). An asymmetric chromosome pair undergoes synaptic adjustment and crossover redistribution during Caenorhabditis elegans meiosis: implications for sex chromosome evolution. Genetics *187*, 685–699.

Hillers, K.J. (2004). Crossover interference. Curr. Biol. *14*, R1036–R1037.

Hillers, K.J., and Villeneuve, A.M. (2003). Chromosome-wide control of meiotic crossing over in C. elegans. Curr. Biol. CB *13*, 1641–1647.

Hiraoka, Y., and Dernburg, A.F. (2009). The SUN rises on meiotic chromosome dynamics. Dev. Cell *17*, 598–605.

Ho, J.W.K., Jung, Y.L., Liu, T., Alver, B.H., Lee, S., Ikegami, K., Sohn, K.-A., Minoda, A., Tolstorukov, M.Y., Appert, A., et al. (2014). Comparative analysis of metazoan chromatin organization. Nature *512*, 449–452.

Hong, S., Sung, Y., Yu, M., Lee, M., Kleckner, N., and Kim, K.P. (2013). The logic and mechanism of homologous recombination partner choice. Mol. Cell *51*, 440–453.

Hunter, N. (2015). Meiotic Recombination: The Essence of Heredity. Cold Spring Harb. Perspect. Biol. a016618.

Hunter, N., and Kleckner, N. (2001). The single-end invasion: an asymmetric intermediate at the double-strand break to double-holliday junction transition of meiotic recombination. Cell *106*, 59–70.

Hyppa, R.W., and Smith, G.R. (2010). Crossover Invariance Determined by Partner Choice for Meiotic DNA Break Repair. Cell *142*, 243–255.

Joyce, E.F., Pedersen, M., Tiong, S., White-Brown, S.K., Paul, A., Campbell, S.D., and McKim, K.S. (2011). Drosophila ATM and ATR have distinct activities in the regulation of meiotic DNA damage and repair. J. Cell Biol. *195*, 359–367.

Joyce, E.F., Apostolopoulos, N., Beliveau, B.J., and Wu, C. -ting (2013). Germline Progenitors Escape the Widespread Phenomenon of Homolog Pairing duringDrosophila Development. PLoS Genet. *9*, e1004013.

Kaback, D.B., Guacci, V., Barber, D., and Mahon, J.W. (1992). Chromosome size-dependent control of meiotic recombination. Science *256*, 228–232.

Kauppi, L., Barchi, M., Baudat, F., Romanienko, P.J., Keeney, S., and Jasin, M. (2011). Distinct properties of the XY pseudoautosomal region crucial for male meiosis. Science *331*, 916–920.

Kaur, T., and Rockman, M.V. (2014). Crossover heterogeneity in the absence of hotspots in Caenorhabditis elegans. Genetics *196*, 137–148.

Keeney, S. (2001). Mechanism and control of meiotic recombination initiation. Curr. Top. Dev. Biol. *52*, 1–53.

Keeney, S., Giroux, C.N., and Kleckner, N. (1997). Meiosis-specific DNA double-strand breaks are catalyzed by Spo11, a member of a widely conserved protein family. Cell *88*, 375–384.

Keeney, S., Lange, J., and Mohibullah, N. (2014). Self-Organization of Meiotic Recombination Initiation: General Principles and Molecular Pathways. Annu. Rev. Genet. *48*, 187–214.

Kelly, K.O., Dernburg, A.F., Stanfield, G.M., and Villeneuve, A.M. (2000). Caenorhabditis elegans msh-5 is required for both normal and radiation-induced meiotic crossing over but not for completion of meiosis. Genetics *156*, 617–630.

Kim, Y., Kostow, N., and Dernburg, A.F. (2015). The Chromosome Axis Mediates Feedback Control of CHK-2 to Ensure Crossover Formation in C. elegans. Dev. Cell *35*, 247–261.

Kleckner, N. (2006). Chiasma formation: chromatin/axis interplay and the role(s) of the synaptonemal complex. Chromosoma *115*, 175–194.

Kleckner, N., Storlazzi, A., and Zickler, D. (2003). Coordinate variation in meiotic pachytene SC length and total crossover/chiasma frequency under conditions of constant DNA length. Trends Genet. TIG *19*, 623–628.

Kleckner, N., Zickler, D., Jones, G.H., Dekker, J., Padmore, R., Henle, J., and Hutchinson, J. (2004). A mechanical basis for chromosome function. Proc. Natl. Acad. Sci. U. S. A. *101*, 12592–12597.

Klutstein, M., and Cooper, J.P. (2014). The Chromosomal Courtship Dance-homolog pairing in early meiosis. Curr. Opin. Cell Biol. *26*, 123–131.

Kohl, K.P., and Sekelsky, J. (2013). Meiotic and mitotic recombination in meiosis. Genetics *194*, 327–334.

Koszul, R., Kim, K.P., Prentiss, M., Kleckner, N., and Kameoka, S. (2008). Meiotic chromosomes move by linkage to dynamic actin cables with transduction of force through the nuclear envelope. Cell *133*, 1188–1201.

Kroon, D.-J. (2011). Snakes: Active Contours.

Kurzbauer, M.-T., Uanschou, C., Chen, D., and Schlogelhofer, P. (2012). The Recombinases DMC1 and RAD51 Are Functionally and Spatially Separated during Meiosis in Arabidopsis. Plant Cell *24*, 2058–2070.

Lande, R., and Stahl, F.W. (1993). Chiasma interference and the distribution of exchanges in Drosophila melanogaster. Cold Spring Harb. Symp. Quant. Biol. *58*, 543–552.

Lange, J., Pan, J., Cole, F., Thelen, M.P., Jasin, M., and Keeney, S. (2011). ATM controls meiotic double-strand-break formation. Nature *479*, 237–240.

Larsson, C., Koch, J., Nygren, A., Janssen, G., Raap, A.K., Landegren, U., and Nilsson, M. (2004). In situ genotyping individual DNA molecules by target-primed rolling-circle amplification of padlock probes. Nat. Methods *1*, 227–232.

Lee, T.C., Kashyap, R.L., and Chu, C.N. (1994). Building skeleton models via 3-D medial surface/axis thinning algorithms. CVGIP Graph Models Image Process *56*, 462–478.

Liang, Z., Zickler, D., Prentiss, M., Chang, F.S., Witz, G., Maeshima, K., and Kleckner, N. (2015). Chromosomes Progress to Metaphase in Multiple Discrete Steps via Global Compaction/Expansion Cycles. Cell *161*, 1124–1137.

Libuda, D.E., Uzawa, S., Meyer, B.J., and Villeneuve, A.M. (2013). Meiotic chromosome structures constrain and respond to designation of crossover sites. Nature *502*, 703–706.

Liu, T., Rechtsteiner, A., Egelhofer, T.A., Vielle, A., Latorre, I., Cheung, M.-S., Ercan, S., Ikegami, K., Jensen, M., Kolasinska-Zwierz, P., et al. (2011). Broad chromosomal domains of histone modification patterns in C. elegans. Genome Res. *21*, 227–236.

Lu, P., Han, X., Qi, J., Yang, J., Wijeratne, A.J., Li, T., and Ma, H. (2012). Analysis of Arabidopsis genome-wide variations before and after meiosis and meiotic recombination by resequencing Landsberg erecta and all four products of a single meiosis. Genome Res. *22*, 508–518.

Lynn, A. (2002). Covariation of Synaptonemal Complex Length and Mammalian Meiotic Exchange Rates. Science *296*, 2222–2225.

MacQueen, A.J., Phillips, C.M., Bhalla, N., Weiser, P., Villeneuve, A.M., and Dernburg, A.F. (2005). Chromosome Sites Play Dual Roles to Establish Homologous Synapsis during Meiosis in C. elegans. Cell *123*, 1037–1050.

Mancera, E., Bourgon, R., Brozzi, A., Huber, W., and Steinmetz, L.M. (2008). High-resolution mapping of meiotic crossovers and non-crossovers in yeast. Nature *454*, 479–485.

Martinez-Perez, E., and Colaiácovo, M.P. (2009). Distribution of meiotic recombination events: talking to your neighbors. Curr. Opin. Genet. Dev. *19*, 105–112.

Martinez-Perez, E., Schvarzstein, M., Barroso, C., Lightfoot, J., Dernburg, A.F., and Villeneuve, A.M. (2008). Crossovers trigger a remodeling of meiotic chromosome axis composition that is linked to two-step loss of sister chromatid cohesion. Genes Dev. *22*, 2886–2901.

Martini, E., Diaz, R.L., Hunter, N., and Keeney, S. (2006). Crossover Homeostasis in Yeast Meiosis. Cell *126*, 285–295.

de Massy, B. (2013). Initiation of meiotic recombination: how and where? Conservation and specificities among eukaryotes. Annu. Rev. Genet. *47*, 563–599.

McKim, K.S., Green-Marroquin, B.L., Sekelsky, J.J., Chin, G., Steinberg, C., Khodosh, R., and Hawley, R.S. (1998). Meiotic synapsis in the absence of recombination. Science *279*, 876–878.

Mehrotra, S., and McKim, K.S. (2006). Temporal analysis of meiotic DNA double-strand break formation and repair in Drosophila females. PLoS Genet. *2*, e200.

Meneely, P.M., McGovern, O.L., Heinis, F.I., and Yanowitz, J.L. (2012). Crossover distribution and frequency are regulated by him-5 in Caenorhabditis elegans. Genetics *190*, 1251–1266.

Mets, D.G., and Meyer, B.J. (2009). Condensins regulate meiotic DNA break distribution, thus crossover frequency, by controlling chromosome structure. Cell *139*, 73–86.

Meyer, F. (1994). Topographic distance and watershed lines. Signal Process. *38*, 113–125.

Muller, H. (1916). The Mechanism of Crossing-Over. Am. Nat. *50*, 284–305.

Muniyappa, K., Kshirsagar, R., and Ghodke, I. (2014). The HORMA domain: an evolutionarily conserved domain discovered in chromatin-associated proteins, has unanticipated diverse functions. Gene *545*, 194–197.

Nabeshima, K., Villeneuve, A.M., and Hillers, K.J. (2004). Chromosome-wide regulation of meiotic crossover formation in Caenorhabditis elegans requires properly assembled chromosome axes. Genetics *168*, 1275–1292.

Nabeshima, K., Mlynarczyk-Evans, S., and Villeneuve, A.M. (2011). Chromosome painting reveals asynaptic full alignment of homologs and HIM-8-dependent remodeling of X chromosome territories during Caenorhabditis elegans meiosis. PLoS Genet. *7*, e1002231.

Nagaoka, S.I., Hassold, T.J., and Hunt, P.A. (2012). Human aneuploidy: mechanisms and new insights into an age-old problem. Nat. Rev. Genet. *13*, 493–504.

Novak, I., Wang, H., Revenkova, E., Jessberger, R., Scherthan, H., and Höög, C. (2008). Cohesin Smc1beta determines meiotic chromatin axis loop organization. J. Cell Biol. *180*, 83–90.

Ogawa, T., Shinohara, A., Nabetani, A., Ikeya, T., Yu, X., Egelman, E.H., and Ogawa, H. (1993). RecA-like recombination proteins in eukaryotes: functions and structures of RAD51 genes. Cold Spring Harb. Symp. Quant. Biol. *58*, 567–576.

Oh, S.D., Lao, J.P., Hwang, P.Y.-H., Taylor, A.F., Smith, G.R., and Hunter, N. (2007). BLM ortholog, Sgs1, prevents aberrant crossing-over by suppressing formation of multichromatid joint molecules. Cell *130*, 259–272.

Page, S.L., and Hawley, R.S. (2004). The genetics and molecular biology of the synaptonemal complex. Annu. Rev. Cell Dev. Biol. *20*, 525–558.

Pan, J., Sasaki, M., Kniewel, R., Murakami, H., Blitzblau, H.G., Tischfield, S.E., Zhu, X., Neale, M.J., Jasin, M., Socci, N.D., et al. (2011). A hierarchical combination of factors shapes the genome-wide topography of yeast meiotic recombination initiation. Cell *144*, 719–731.

Panizza, S., Mendoza, M.A., Berlinger, M., Huang, L., Nicolas, A., Shirahige, K., and Klein, F. (2011). Spo11-accessory proteins link double-strand break sites to the chromosome axis in early meiotic recombination. Cell *146*, 372–383.

Penkner, A.M., Fridkin, A., Gloggnitzer, J., Baudrimont, A., Machacek, T., Woglar, A., Csaszar, E., Pasierbek, P., Ammerer, G., Gruenbaum, Y., et al. (2009). Meiotic chromosome homology search involves modifications of the nuclear envelope protein Matefin/SUN-1. Cell *139*, 920–933.

Phillips, C.M., and Dernburg, A.F. (2006). A family of zinc-finger proteins is required for chromosome-specific pairing and synapsis during meiosis in C. elegans. Dev. Cell *11*, 817–829.

Phillips, C.M., Wong, C., Bhalla, N., Carlton, P.M., Weiser, P., Meneely, P.M., and Dernburg, A.F. (2005). HIM-8 binds to the X chromosome pairing center and mediates chromosome-specific meiotic synapsis. Cell *123*, 1051–1063.

Phillips, C.M., McDonald, K.L., and Dernburg, A.F. (2009a). Cytological analysis of meiosis in Caenorhabditis elegans. Methods Mol. Biol. Clifton NJ *558*, 171–195.

Phillips, C.M., Meng, X., Zhang, L., Chretien, J.H., Urnov, F.D., and Dernburg, A.F. (2009b). Identification of chromosome sequence motifs that mediate meiotic pairing and synapsis in C. elegans. Nat. Cell Biol. *11*, 934–942.

Reynolds, A., Qiao, H., Yang, Y., Chen, J.K., Jackson, N., Biswas, K., Holloway, J.K., Baudat, F., de Massy, B., Wang, J., et al. (2013). RNF212 is a dosage-sensitive regulator of crossing-over during mammalian meiosis. Nat. Genet. *45*, 269–278.

Rockman, M.V., and Kruglyak, L. (2009). Recombinational landscape and population genomics of Caenorhabditis elegans. PLoS Genet. *5*, e1000419.

Rog, O., and Dernburg, A.F. (2013). Chromosome pairing and synapsis during Caenorhabditis elegans meiosis. Curr. Opin. Cell Biol. *25*, 349–356.

Rog, O., and Dernburg, A.F. (2015). Direct Visualization Reveals Kinetics of Meiotic Chromosome Synapsis. Cell Rep.

Rosu, S., Libuda, D.E., and Villeneuve, A.M. (2011). Robust Crossover Assurance and Regulated Interhomolog Access Maintain Meiotic Crossover Number. Science *334*, 1286–1289.

Rosu, S., Zawadzki, K.A., Stamper, E.L., Libuda, D.E., Reese, A.L., Dernburg, A.F., and Villeneuve, A.M. (2013). The C. elegans DSB-2 protein reveals a regulatory network that controls competence for meiotic DSB formation and promotes crossover assurance. PLoS Genet. *9*, e1003674.

Saito, T.T., Mohideen, F., Meyer, K., Harper, J.W., and Colaiácovo, M.P. (2012). SLX-1 Is Required for Maintaining Genomic Integrity and Promoting Meiotic Noncrossovers in the Caenorhabditis elegans Germline. PLoS Genet. *8*, e1002888.

Sato, A., Isaac, B., Phillips, C.M., Rillo, R., Carlton, P.M., Wynne, D.J., Kasad, R.A., and Dernburg, A.F. (2009). Cytoskeletal forces span the nuclear envelope to coordinate meiotic chromosome pairing and synapsis. Cell *139*, 907–919.

Schwacha, A., and Kleckner, N. (1995). Identification of double Holliday junctions as intermediates in meiotic recombination. Cell *83*, 783–791.

Shintomi, K., and Hirano, T. (2011). The relative ratio of condensin I to II determines chromosome shapes. Genes Dev. *25*, 1464–1469.

Smagulova, F., Gregoretti, I.V., Brick, K., Khil, P., Camerini-Otero, R.D., and Petukhova, G.V. (2011). Genome-wide analysis reveals novel molecular features of mouse recombination hotspots. Nature *472*, 375–378.

Sommermeyer, V., Béneut, C., Chaplais, E., Serrentino, M.E., and Borde, V. (2013). Spp1, a member of the Set1 Complex, promotes meiotic DSB formation in promoters by tethering histone H3K4 methylation sites to chromosome axes. Mol. Cell *49*, 43–54.

Stamper, E.L., Rodenbusch, S.E., Rosu, S., Ahringer, J., Villeneuve, A.M., and Dernburg, A.F. (2013). Identification of DSB-1, a protein required for initiation of meiotic recombination in Caenorhabditis elegans, illuminates a crossover assurance checkpoint. PLoS Genet. *9*, e1003679.

Storlazzi, A., Gargano, S., Ruprich-Robert, G., Falque, M., David, M., Kleckner, N., and Zickler, D. (2010). Recombination proteins mediate meiotic spatial chromosome organization and pairing. Cell *141*, 94–106.

Sym, M., Engebrecht, J.A., and Roeder, G.S. (1993). ZIP1 is a synaptonemal complex protein required for meiotic chromosome synapsis. Cell *72*, 365–378.

Tease, C., and Hultén, M.A. (2004). Inter-sex variation in synaptonemal complex lengths largely determine the different recombination rates in male and female germ cells. Cytogenet. Genome Res. *107*, 208–215.

Thacker, D., Mohibullah, N., Zhu, X., and Keeney, S. (2014). Homologue engagement controls meiotic DNA break number and distribution. Nature *510*, 241–246.

Tsubouchi, T., Macqueen, A.J., and Roeder, G.S. (2008). Initiation of meiotic chromosome synapsis at centromeres in budding yeast. Genes Dev. *22*, 3217–3226.

Voelkel-Meiman, K., Moustafa, S.S., Lefrançois, P., Villeneuve, A.M., and MacQueen, A.J. (2012). Full-length synaptonemal complex grows continuously during meiotic prophase in budding yeast. PLoS Genet. *8*, e1002993.

de Vries, F.A.T., de Boer, E., van den Bosch, M., Baarends, W.M., Ooms, M., Yuan, L., Liu, J.-G., van Zeeland, A.A., Heyting, C., and Pastink, A. (2005). Mouse Sycp1 functions in synaptonemal complex assembly, meiotic recombination, and XY body formation. Genes Dev. *19*, 1376–1389.

Wang, S., Zickler, D., Kleckner, N., and Zhang, L. (2015). Meiotic crossover patterns: obligatory crossover, interference and homeostasis in a single process. Cell Cycle Georget. Tex *14*, 305–314.

Wiggins, P.A., Cheveralls, K.C., Martin, J.S., Lintner, R., and Kondev, J. (2010). Strong intranucleoid interactions organize the Escherichia coli chromosome into a nucleoid filament. Proc. Natl. Acad. Sci. U. S. A. *107*, 4991–4995.

Wormbase (2015). Wormbase.

Wynne, D.J., Rog, O., Carlton, P.M., and Dernburg, A.F. (2012). Dynein-dependent processive chromosome motions promote homologous pairing in C. elegans meiosis. J. Cell Biol. *196*, 47–64.

Yokoo, R., Zawadzki, K.A., Nabeshima, K., Drake, M., Arur, S., and Villeneuve, A.M. (2012). COSA-1 reveals robust homeostasis and separable licensing and reinforcement steps governing meiotic crossovers. Cell *149*, 75–87.

Youds, J.L., and Boulton, S.J. (2011). The choice in meiosis - defining the factors that influence crossover or non-crossover formation. J. Cell Sci. *124*, 501–513.

Zhang, L., Wang, S., Yin, S., Hong, S., Kim, K.P., and Kleckner, N. (2014). Topoisomerase II mediates meiotic crossover interference. Nature *511*, 551–556.

Zhong, X.B., Lizardi, P.M., Huang, X.H., Bray-Ward, P.L., and Ward, D.C. (2001). Visualization of oligonucleotide probes and point mutations in interphase nuclei and DNA fibers using rolling circle DNA amplification. Proc. Natl. Acad. Sci. U. S. A. *98*, 3940–3945.

Zickler, D., and Kleckner, N. (1999). Meiotic chromosomes: integrating structure and function. Annu. Rev. Genet. *33*, 603–754.

Zickler, D., and Kleckner, N. (2015). Recombination, Pairing, and Synapsis of Homologs during Meiosis. Cold Spring Harb. Perspect. Biol. *7*.